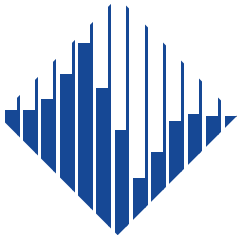

PACIFIC EARTHQUAKE ENGINEERING
RESEARCH CENTER

A Methodology for the Estimation of Kappa (κ) from Large Datasets: Example Application to Rock Sites in the NGA-East Database and Implications on Design Motions

Olga-Joan Ktenidou

Norman A. Abrahamson

Department of Civil and Environmental Engineering
University of California, Berkeley

Robert B. Darragh

Walter J. Silva

Pacific Engineering & Analysis
El Cerrito, California

PEER Report No. 2016/01
Pacific Earthquake Engineering Research Center
Headquarters at the University of California, Berkeley

April 2016

PEER 2016/01
April 2016

A Methodology for the Estimation of Kappa (κ) from Large Datasets: Example Application to Rock Sites in the NGA-East Database and Implications on Design Motions

Olga-Joan Ktenidou

Norman A. Abrahamson

Department of Civil and Environmental Engineering
University of California at Berkeley

Robert B. Darragh

Walter J. Silva

Pacific Engineering & Analysis
El Cerrito, California

PEER Report 2016/01
Pacific Earthquake Engineering Research Center
Headquarters, University of California, Berkeley

April 2016

ABSTRACT

This report reviews four of the main approaches (two band-limited and two broadband) currently used for estimating the site κ_0: the acceleration slope (AS) above the corner frequency, the displacement slope (DS) below the corner frequency, the broadband (BB) fit of the spectrum, and the response spectral shape (RESP) template. Using these four methods, estimates of κ_0 for rock sites in Central Eastern North America (CENA) in the shallow crustal dataset from NGA-East are computed for distances less than 100 km.

Using all of the data within 100 km, the mean κ_0 values are 8 msec for the AS approach and 27 msec for the DS approach. These mean values include negative κ estimates for some sites. If the negative κ values are removed, then the mean values are 25 msec and 42 msec, respectively. Stacking all spectra together led to mean κ_0 values of 7 and 29 msec, respectively. Overall, the DS approach yields 2–3 times higher values than the AS, which agrees with previous observations, but the uncertainty of the estimates in each case is large. The AS approach seems consistent for magnitudes down to **M**3 but not below.

There is large within-station variability of κ that may be related to differences in distance, Q, complexity along the path, or particular source characteristics, such as higher or lower stress drop. The station-to-station differences may be due to site-related factors. Because most sites have been assigned V_{s30} = 2000 m/sec, it is not possible to correlate variations in κ_0 with rock stiffness.

Based on the available profile, the individual spectra are corrected for crustal amplification and only affect results below 15 Hz. Since the AS and DS approaches are applied over different frequency ranges, we find that only the DS results are sensitive to the amplification correction. More detailed knowledge of individual near-surface profiles may have effects on AS results, too. Although κ is considered to be caused solely by damping in the shallow crust, measurement techniques often cannot separate the effects of damping and amplification, and yield the net effect of both phenomena.

The two broadband approaches, BB and RESP, yield similar results. The mean κ_{0_BB} is 5±0.5 msec across all NEHRP class A sites. The κ_{0_RESP} for the two events examined is 5 and 6 msec. From literature, the average value of κ_0 in CENA is 6 ± 2 msec. This typical value is similar to the broadband estimates of this study and to the mean κ_{AS} when all available recordings are used along with all flags. When only recordings with down-going FAS slope are selected from the dataset, the mean value of κ_{AS} increases by a factor of 2–3.

To evaluate the scaling of high-frequency ground motion with κ, we analyze residuals from ground motion prediction equations (GMPEs) versus κ estimates. Using the κ values from the AS approach, the average trend of the ln(PSA) residuals for hard-rock data do not show the expected strong dependence on κ, but when using κ values from the DS approach, there is a stronger correlation of the residuals, i.e., a κ that is more consistent with the commonly used analytically based scaling. The κ_{DS} estimates may better reflect the damping in the shallow crust, while the κ_{AS} estimates may reflect a net effect of damping and amplification that has not been decoupled. The κ_{DS} estimates are higher than the κ_{AS} estimates, so the expected effect on the high-frequency ground motion is smaller than that expected for the κ_{AS} estimates.

An empirical hard-rock site factor model is developed that represents the combined V_s-κ_0 site factor relative to a 760 m/sec reference-site condition. At low frequencies (< 3 Hz), the empirical site factors are consistent with the scaling due to the change in the impedance contrast. At high frequencies (> 10 Hz), the residuals do not show the strong increase in the site factors as seen in the analytical model results. A second hard-rock dataset from British Columbia, Canada, is also used. This BC hard-rock residuals show an increase in the 15–50 Hz range that is consistent with the analytical κ_0 scaling for a hard-rock κ_0 of about 0.015 sec.

The variability of the PSA residuals is also used to evaluate the κ_0 scaling for hard-rock sites from analytical modeling. The scatter in existing κ_0 values found in literature is disproportionately large compared to the observed variability in high-frequency ground motions. We compared the predicted ground-motion variability based on analytical modeling to the observed variability in our residuals. While the hard-rock sites are more variable at high frequencies due to the additional κ_0 variability, this additional variability is much less than the variability predicted by the analytical modeling using the variability from κ_0-V_{s30} correlations. This is consistent with weaker κ_0 scaling compared to that predicted by the analytical modeling seen in the mean residuals.

ACKNOWLEDGMENTS

We thank John Anderson, Glenn Biasi, and Jim Brune of University of Nevada, Reno (UNR), for fruitful discussions that took place in December 2013 at UNR. Thanks also go to the members of the NGA-West and NGA-East projects, including Dave Boore, Tadahiro Kishida, and Justin Hollenback. We also thank Dino Bindi, Sanjay Bora, Aurore Laurendeau, Matthew Muto, and Phillipe Renault for discussions. Additional thanks go to Claire M. Johnson, PEER Editor, for her help in preparing this manuscript for publication.

This study was partially sponsored by the Pacific Earthquake Engineering Research Center (PEER). The first author was also partially funded by PG&E, the French Sigma Project, and the GFZ German Research Centre for Geosciences. Any opinions, findings, and conclusions or recommendations expressed are those of the authors and do not necessarily reflect those of the sponsoring agencies.

This work is dedicated to the memory of Stephen P. Ktenides (1926–2016).

CONTENTS

LIST OF TABLES

LIST OF FIGURES

1 Introduction

1.1 IMPLICATIONS OF κ AND ITS UNCERTAINTY ON DESIGN GROUND MOTIONS

For typical rock and deep soil sites, which display an overall increase in stiffness with depth due primarily to increasing confining pressure, the major contribution to seismic energy dissipation at a site occurs over the top several km of the crust at close (< about 50 km) rupture distances [Anderson and Hough 1984; Silva and Darragh 1996; and Campbell 2009]. This observation was first recognized and subsequently characterized as a site parameter by Anderson and Hough [1984], specifically as kappa (κ) at zero epicentral distance (κ_0). However, due to geologic processes, at sites which reflect significant departures from an overall increase in stiffness with depth such as layered basalt and sedimentary soil or rock sequences, significant contributions to κ may occur at depths well beyond 1– 2 km and reflect contributions from both damping as well as scattering.

The damping reflected in the measurement of κ appears to be frequency independent (hysteretic), occurs at low strains, and is the principal site or path parameter controlling the limitation of high-frequency (> 5 Hz) strong ground motion at close-in (≤ 50 km) sites. As a result, its value or range of values is important in characterizing strong ground motions for engineering design. Additionally, because it is generally independent of the level of motion at rock or very stiff sites, small local or regional earthquakes may be used to estimate its value or range in values.

Uncertainty in the estimation of κ is large [Ktenidou et al. 2014]. In practice, this may have significant implications for seismic risk. At rock sites, the estimation of the damping in the profile is important to assessing appropriate levels of high-frequency (> ~5 Hz) design motions. In probabilistic seismic hazard assessment (PSHA) for critical facilities, ground motion prediction equations (GMPEs) are often adjusted from host to target regions, typically from active regions for soft-rock conditions to less active regions for hard-rock conditions; for example, as was done by Campbell [2003; 2004], using the hybrid empirical method. The scaling from soft rock to hard rock is made considering the differences in V_{s30} and κ_0 to account for both site amplification, which is dominant at lower frequencies, and site attenuation, which dominates high frequencies [Cotton et al. 2006; Van Houtte et al. 2011]. Adjusting the GMPEs to hard-rock conditions is sensitive to κ_0. For example, the Pegasos Refinement Project [Biro and Renault 2012] showed that the κ_0 corrections from soft-rock to hard-rock conditions can lead to differences up to a factor of 3 in the high-frequency part of the response spectrum, depending on the target κ_0 value; see Figures 1.1–1.3. This can lead to a large uncertainty in the probabilistic

risk at nuclear facilities with safety-related equipment that is sensitive to ground shaking at frequencies above 20 Hz.

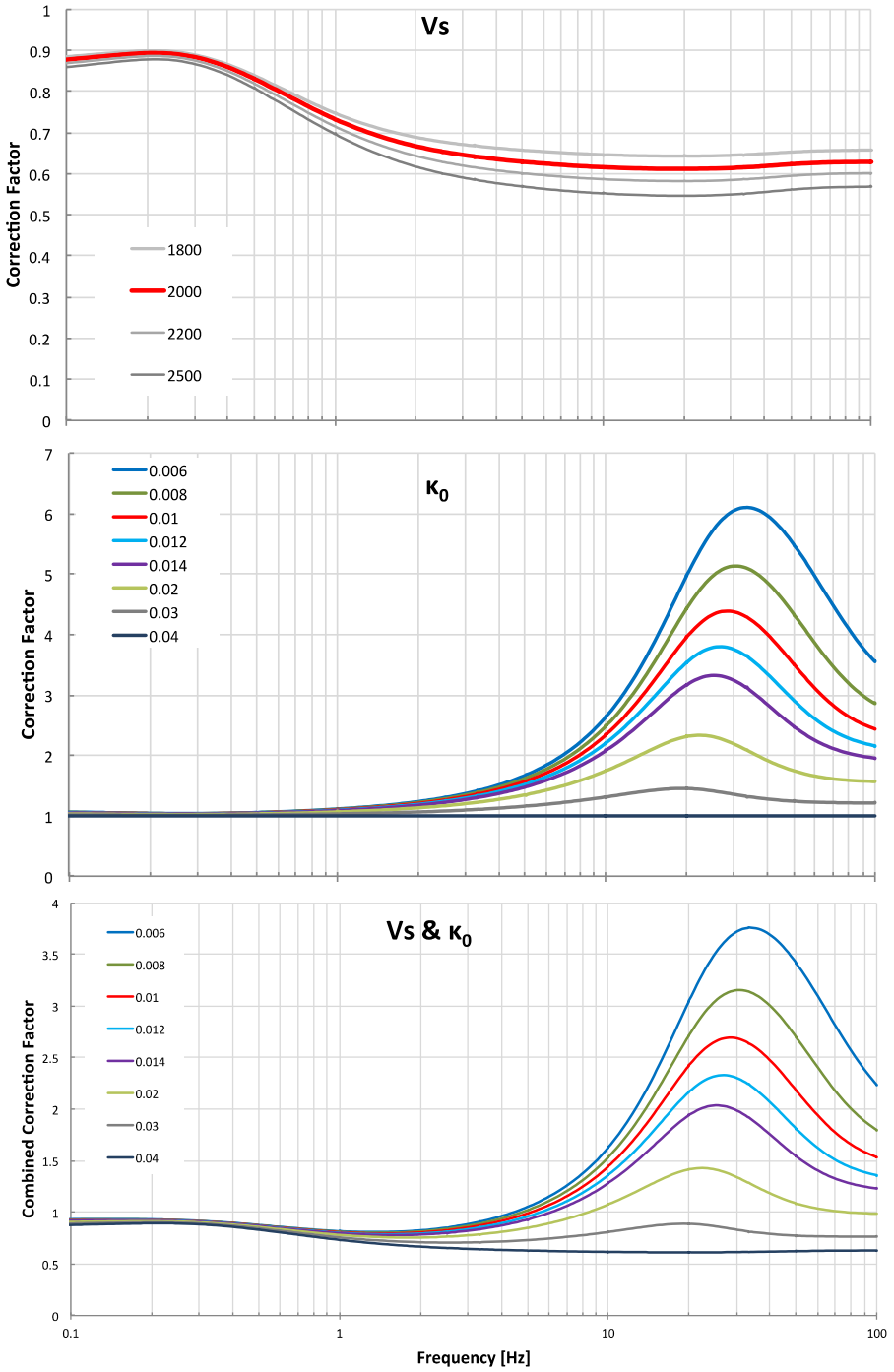

Figure 1.1 **Example of V_s, and κ, and combined V_s - κ_0 correction functions evaluated for Abrahamson and Silva GMPE [2008] with respect to κ_0 = 0.04 sec (after Biro and Renault [2012]).**

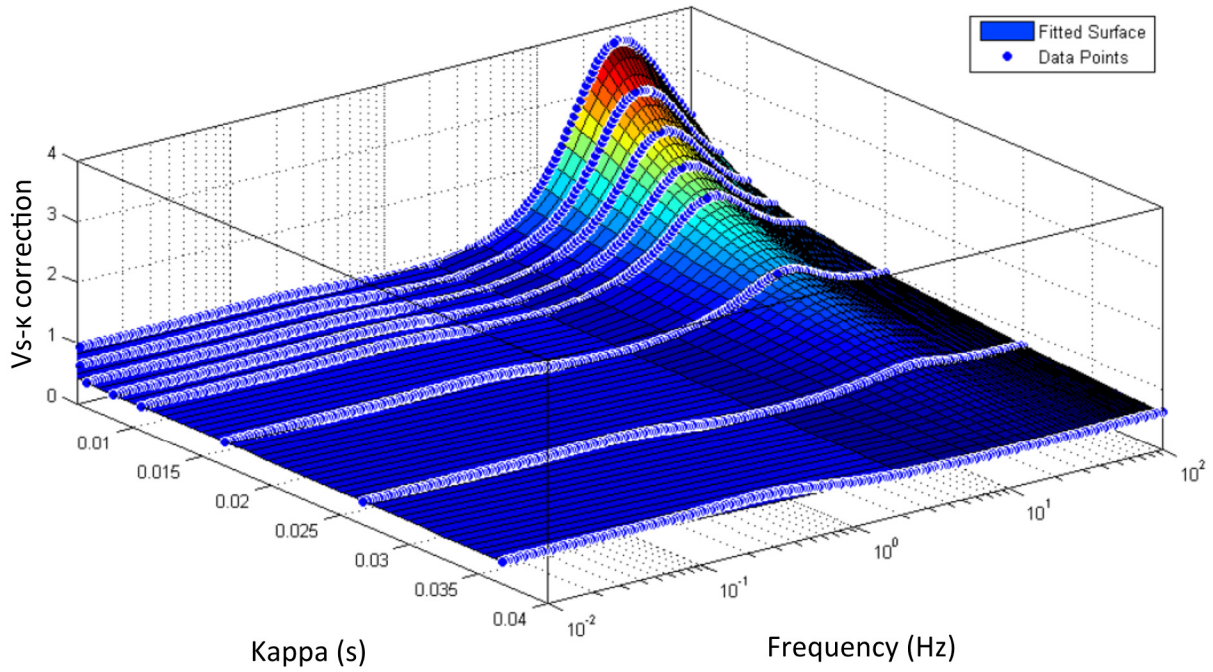

Figure 1.2 **Example parameterization of V_s and κ_0 correction functions by fitting a surface to the evaluated correction functions (here for a given V_{s30} and a range of target κ_0 values) (after Biro and Renault [2012]).**

High-frequency ground motion (> 5 Hz) is also very important for the seismic behavior of small concrete dams. Their eigen-frequencies may reach 16 Hz (Figure 1.4), and peak stresses may be controlled by high frequencies [Muto and Duron 2015]. The concrete in old dams may be unreinforced or under-reinforced, and the formation of cracks may leave them vulnerable to failure under hydrostatic pressure. Muto and Duron [2015] studied the effect of κ_0 on the hazard of Southern California Edison (SCE) dams when updated from assumed values of κ_0, based on V_{s30}, to measured, site-specific values. In this case, the measured κ values were significantly larger than the assumed κ values, which reduced the 10 Hz ground motion by a factor of 2.4; see Figure 1.5.

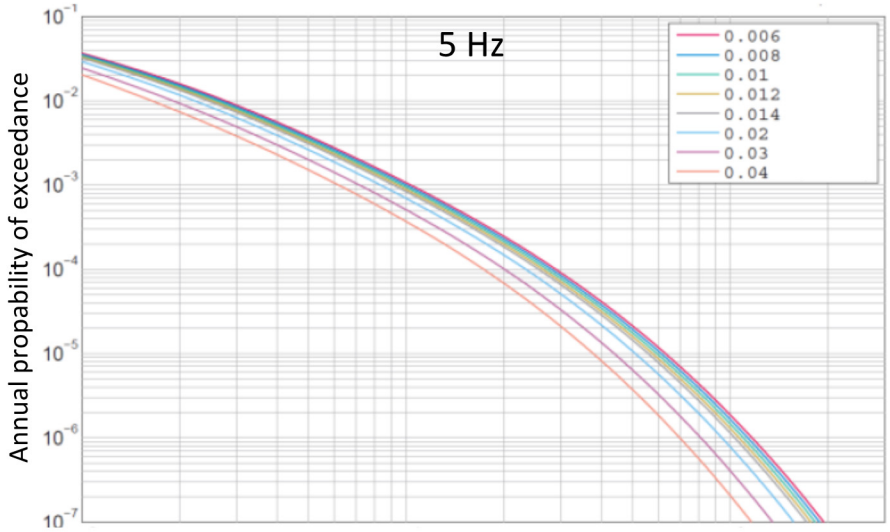

(a)

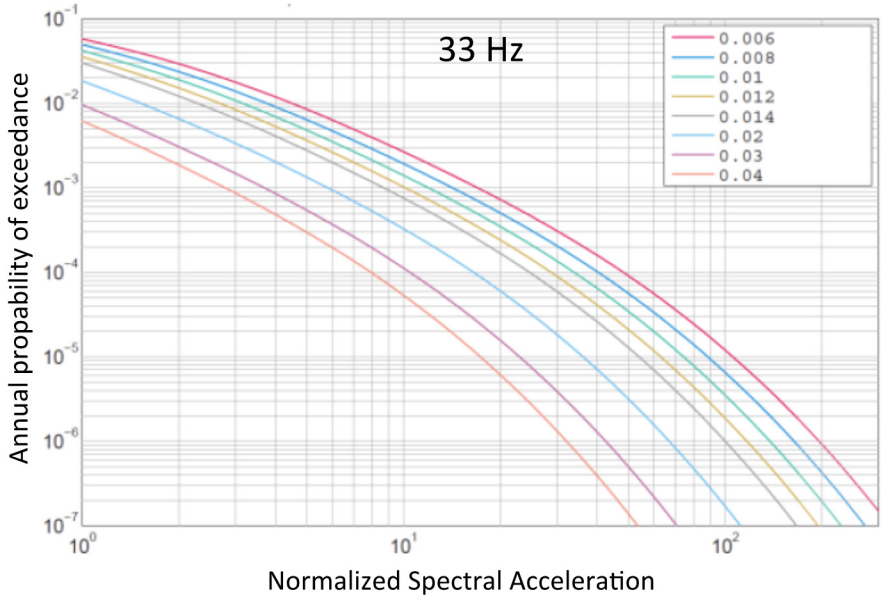

(b)

Figure 1.3 **Hazard sensitivity to different target κ_0 values for (a) 5 Hz and (b) 33 Hz at an example site in Switzerland. The host κ_0 is fixed as 0.04 sec with V_{s30} = 800 m/sec. The target conditions are V_{s30} = 2000 m/sec with different κ_0 values ranging from 0.006 sec to 0.04 sec (after Biro and Renault [2012]).**

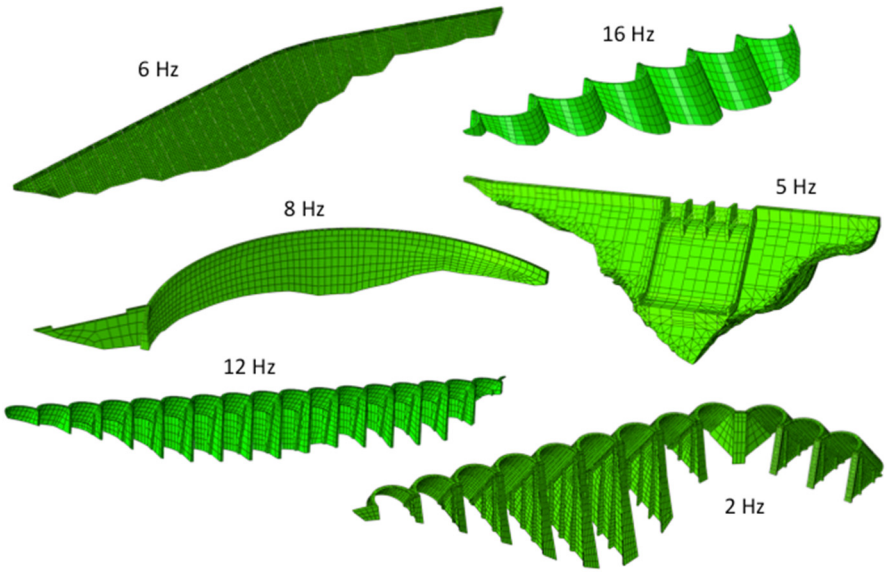

Figure 1.4 **Eigen-frequencies of concrete dams (after Muto and Duron [2015]).**

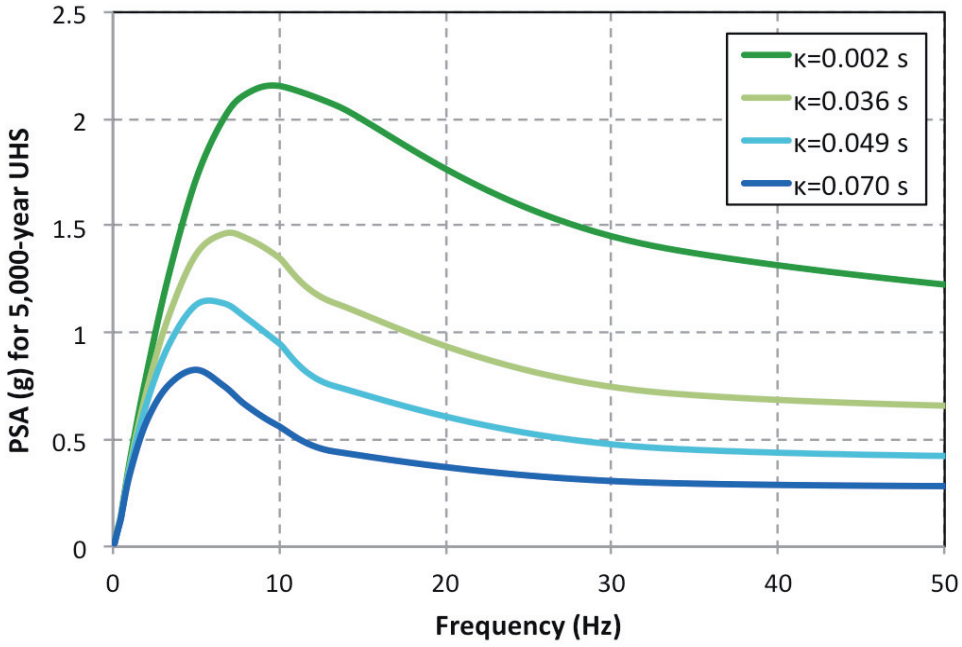

Figure 1.5 **Five-thousand-year Uniform Hazard Spectrum for different κ_0 values (after Muto and Duron [2015]).**

1.2 OVERVIEW

This report reviews most of the main approaches currently used for estimating κ (and, in particular, its site-specific component, κ_0), makes some methodological suggestions for improvement, and demonstrates how subsets for which the different approaches can be used may be selected from large ground-motion datasets. Lastly, the report provides a preliminary estimate of κ_0 for rock sites in Central-Eastern North America (CENA), using the shallow crustal dataset from NGA-East [Goulet et al. 2014].

Chapter 2 discusses the estimation of κ_0 by four different methods: two band-limited and two broadband. Following the nomenclature proposed by Ktenidou et al. [2014], these are referred to as the acceleration spectrum approach (AS), the displacement spectrum approach (DS), the broadband approach (BB), and the response spectral shape approach (RESP). The AS approach is applied in a frequency range above the source corner frequency (f_c), the DS approach is applied below f_c, and the BB and RESP approaches use the entire usable frequency range. These approaches were introduced, respectively, in Anderson and Hough [1984], Biasi and Smith [2001], Silva et al. [1997], and Silva and Darragh [1995]. Table 1.1 outlines the approaches based on certain common features, such as the principle behind the approach and the frequency range over which κ is computed.

We make a clear distinction between κ_r and κ_0. The aim is to estimate κ_0, the zero-distance, site-specific attenuation factor. Some of the approaches to measure κ, such as AS and DS, generally start with individual measurements of κ_r (i.e., observations on individual spectra at distance r), which must then be combined, interpreted, and extrapolated to zero epicentral distance to obtain an estimate of κ_0 for the site. Others, such as BB or RESP, yield directly the κ_0 (i.e., the site-specific, zero-distance κ derived from many observations), after having corrected for path attenuation $Q(f)$ and crustal amplification. There are different ways of extrapolating κ_r values to zero distance (i.e., correcting for the path contribution); these are discussed in Chapter 2.

To use the band-limited approaches AS and DS, an estimate of f_c must be made, to either estimate κ below or above this frequency. The source corner frequency depends on the moment magnitude—which is typically well constrained—and the event stress drop—which is usually unknown except for special studies of larger events. For many regions (e.g., CENA), published stress drop values may vary greatly, making it difficult to assign a single value.

Every record in the NGA-East database is attributed a lowest and highest usable frequency, which are typically selected based on the noise level and the anti-alias filter. Data (Fourier amplitude spectrum or FAS) can only be used between these two values. In an application of either the AS or DS approach, a check is made to determine whether the source f_c lies within the usable bandwidth of the record, and whether there is an adequate overlap between the usable frequency range and the frequency range in which κ can be measured. For large databases, instead of starting directly with data analysis for κ calculations, as a first step it is important to create data subsets for which each of the approaches (AS and DS) may potentially be used, based on f_c and bandwidth considerations. For instance, in the NGA-East (CENA) dataset, there are many recordings for which there is no available bandwidth for κ analysis due to the small-to-moderate magnitude of the events and the high stress drop. The issue of data selection is further addressed in Chapter 2.

Table 1.1 Approaches used for estimating κ (adapted from Ktenidou et al. [2014]).

Notation	Principle	Main references	Measurement/computation	Frequency range
$\kappa_{\_AS}$	High-frequency decay of the S-wave Fourier spectrum	Anderson and Hough [1984], Hough and Anderson [1988]	Direct measurement on the *S*-wave Fourier **acceleration spectrum** above f_c, where it is theoretically flat	Above f_c
$\kappa_{\_DS}$	Small magnitudes (strong trade-off with source)	Biasi and Smith [2001]	Direct measurement on low-frequency part of the Fourier **displacement spectrum** (much below f_c) where it is theoretically flat	Below f_c
$\kappa_{\_BB}$	Inversion of the entire frequency band of the spectrum	Anderson and Humphrey [1991], Humphrey and Anderson [1992], Silva et al. [1997], Edwards et al. [2011]	**Broadband** inversion of the entire spectrum for source, path and site terms (usually for moment, f_c and κ_0)	Entire band
$\kappa_{\_RESP}$	Peak and shape of the normalized acceleration response spectrum	Silva and Darragh [1995], Silva et al. [1998]	Fitting of stochastically simulated **response spectra** (where κ is a model input parameter) coupled with site amplification to observed response spectra	Entire band

f_c: source corner frequency

Chapter 3 estimates κ_0 for rock sites in the NGA-East dataset. The flatfile provides FAS for different time windows, including the entire record, pre-event noise, *P* -wave, *S-Lg* -waves, combined *P*- and *S-Lg*-waves, and coda. We use the *S-Lg*-wave-window FAS to compute κ in the horizontal direction—irrespective of measurement approach—to be consistent with the original definition of κ as *S*-wave attenuation, and because structural damage is usually related mostly shaking from *S-Lg*-waves in CENA.

Chapter 4 analyzes residuals from several GMPEs versus κ_0 measurements, and reviews other existing global datasets that could be used in future. The weak correlation between high-frequency residuals and κ_0 indicates that other correlations between parameters may exist (e.g., between κ_0 and crustal amplification). To address the correlation, the combined effect of impedance (V_s) and attenuation (κ) is computed and compared with analytical modeling results.

Chapter 5 provides a detailed research plan for moving forward in the estimation of high-frequency ground motions at hard-rock sites, including the effects of κ.

2 Band-Limited versus Broadband Approaches for Estimating κ

2.1 BACKGROUND ON κ

At high frequencies, the spectral amplitude of acceleration decays rapidly. Hanks [1982] first introduced f_{max} to model the frequency above which the spectrum decreases, while Anderson and Hough [1984] introduced the spectral decay factor (κ) to model the rate of the decrease. κ is a crucial input for describing high-frequency motion in various applications, including the simulation of ground motion and the creation and adjustment of GMPEs from one region to another. There are many approaches for estimating κ [Ktenidou et al. 2014]. Anderson and Hough [1984] defined κ based on the observation that, above a given frequency, the amplitude of the FAS decays linearly if plotted in linear-logarithmic space. κ for a given record at some distance from the source (termed κ_r) can be related to the slope (λ) of the FAS (a) as follows:

$$\kappa_r = -\lambda / \pi \tag{2.1}$$

where $\lambda = \Delta(\ln a) / \Delta f$.

The same authors observed that measured κ_r values at a given station scale with distance. The zero-epicentral-distance intercept of the κ trend with distance (denoted κ_0) corresponds to the attenuation that *S*-waves encounter when travelling vertically through the geological structure beneath the station. The distance dependence corresponds to the incremental increase in attenuation due to predominantly horizontal *S*-wave propagation through the crust. As a first approximation, the distance dependence may be considered linear and denoted by κ_R, so that the overall κ can be written as follows, in units of time:

$$\kappa_r = \kappa_0 + \kappa_R \cdot R \text{ (sec)} \tag{2.2}$$

This linear approximation of the path component does not always describe the distance dependence, but has proven to be a good approximation in many cases (e.g., Nava et al. [1999]; Douglas et al. [2010]; Gentili and Francheschina [2011]; and Ktenidou et al. [2013]). The κ_0 component may also have possible source contributions (e.g., Tsai and Chen [2000] and Purvance and Anderson [2003]); however, this may be related more to the scatter than to the mean value of κ_0 [Kilb et al. 2012]. For more background on the debate as to source components in κ_0 and f_{max}, the reader is referred to Ktenidou et al. [2014]. In current applications, κ_0 is taken

primarily to describe site attenuation due to local geological conditions over the top few hundreds of meters to several kilometers beneath the site under study [Anderson and Hough 1984; Campbell, 2009].

Interest in κ_0 has increased because it constitutes an important input parameter when adjusting GMPEs to different regions through the host-to-target method [Cotton et al. 2006; Douglas et al. 2006; and Biro and Renault 2012], and in constraining high frequencies for synthetic ground motion generated either by stochastic, physics-based, or hybrid-method simulations (e.g., Boore [2003]; Graves and Pitarka [2010]; and Mai et al. [2010]). The EPRI report [2013] outlines the use of κ for development of site-specific amplification factors for Ground Motion Response Spectra (GMRS) screening at facilities with limited site-characterization data and then prioritization of nuclear power plant sites in the U.S. for additional analyses. Future GMPEs may also incorporate κ_0 as a new predictor variable (e.g., Laurendeau et al. [2013]).

2.2 THE BAND-LIMITED APPROACH 'AS'

In the original definition of Anderson and Hough [1984], κ_r can be directly measured in log-linear space on the high-frequency part of the FAS of the *S*-waves, between frequencies f_1 and f_2, where the decay is approximately linear; see Figure 2.1. We will refer to this original definition as κ_{r_AS}. Because a component of horizontal wave propagation, affected by Q, is present in these measurements, an extrapolation to zero distance (assuming frequency-independent Q) will lead to the site-specific attenuation component, κ_{0_AS}.

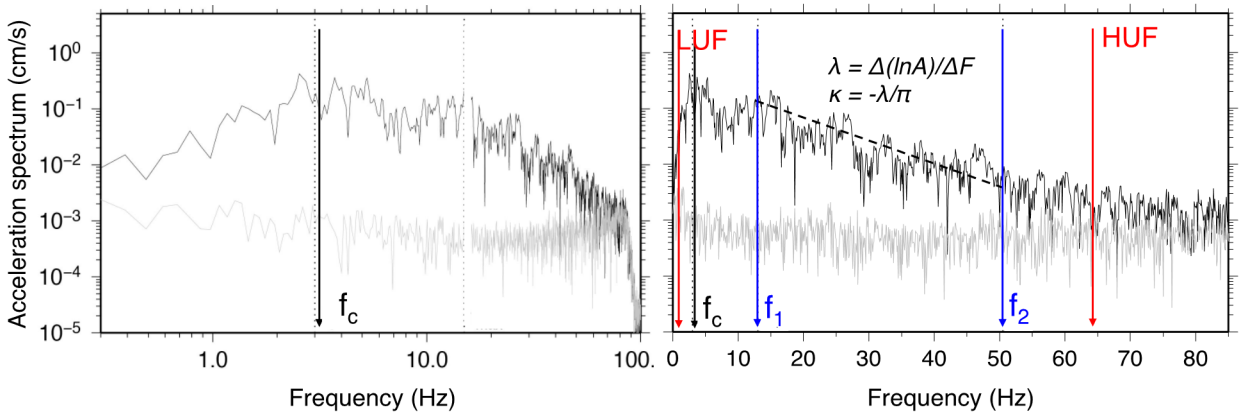

Figure 2.1 **Example acceleration FAS for noise (grey) and *S*-waves (black) in log–log (left) and log–linear (right) scale.**

The following three steps to compute κ_{0_AS} starting from the individual FAS are proposed.

- Step 1: choose the frequency band in which the measurement should be made
- Step 2: measure κ_{r_AS} on the individual spectra or on the vector-sum (orientation-independent spectra)
- Step 3: interpret all of the individual measurements to produce a κ model.

These steps are described below.

2.2.1 Step 1: Frequency Band

As the first step, certain objective criteria define the allowable frequency range within which to perform κ measurements. These are expanded from the considerations outlined in Ktenidou et al. [2013].

This approach is generally used for moderate to large magnitude events, as f_1 must exceed the source corner frequency (f_c) to avoid any trade-off with the source. Furthermore, it is advisable not only to work above f_c, but to maintain a buffer frequency range of 1.5 f_c, to avoid trade-offs between the source and site. This factor also acknowledges some of the uncertainty in the f_c estimate. Therefore, the frequency range in which κ_{r_AS} is measured may begin at f_{1_AS} = 1.5 f_c [J. G. Anderson, *personal communication*, 2013]. However, considering the definition of the corner frequency, 1.5 f_c corresponds to only 70% of amplitude of the plateau of the spectrum; a factor of 3 f_c would be required to reach 90% of the plateau level. In practice, as there are narrow usable bandwidth concerns, Anderson's recommendation that a factor of 1.5 f_c is sufficient was followed to avoid rejecting many recordings.

Each record in the database is assigned a lowest and highest usable frequency (HUF and LUF, respectively, see Figure 2.1), which are typically dependent on the instrument response (gain and anti-alias corner frequency), noise level, and sampling rate (Nyquist frequency). Fourier amplitude spectrum values can only be used to measure κ between these two frequency values. The frequency range within which κ_{r_AS} is measured must lie within the usable bandwidth of the record (f_{2_AS} = HUF). Working within the usable frequency range ensures that the response is flat because the data have been corrected for the instrument response. For instance, it would be an error to compute κ_{r_AS} including frequencies where the instrument response (uncorrected) has begun to decay, because this decay would be interpreted as site attenuation, thus biasing κ_{r_AS} towards larger values.

The data must have an acceptable signal-to-noise ratio (SNR) for a robust estimate of κ_{r_AS} on the FAS of the *S*-wave window. For recordings where there exists a pre-event noise window, and where it is deemed adequate in length, then the required SNR was taken as 3. For recordings where there is no noise window (e.g., analog recordings), or where it is too short (e.g., limited pre-event memory or late trigger from a distant event), the SNR may be computed with respect to the coda window, and its limit value can lower, for example, 2. In those cases where there is no coda, the *P*-wave window may be used. A visual inspection may also be made, as an

increasing trend with increasing frequency may be interpreted as the noise dominating the signal in the FAS. κ is computed on the *S*-*Lg*-wave windows for the horizontal components. In contrast, the vertical component is best computed on the combined *P*- and *S*-*Lg*-wave window, so the SNR should be computed accordingly.

After following all of these criteria, the frequency ranges within which κ_{r_AS} is measured ($DF = f_2 - f_1$) must be wide enough to ensure a stable estimate of the spectral slope. Depending on the data available, the minimum range was set at 8–10 Hz in this study.

2.2.2 Step 2: Individual Measurements

After the determination of the frequency range within which κ can be measured, the second step is the computation of κ_{r_AS} for each individual spectrum. Here, we summarize the main considerations.

Orientation

Van Houtte et al. [2014] observed that the orientation of the horizontal components may have significant effects on the measured κ_{r_AS}. Typically, the two horizontal components are used separately and the measured κ values are then averaged. In some cases, a check is performed that rejects recordings for which the κ on the two horizontal components differ significantly (e.g., Douglas et al. [2010] and Ktenidou et al. [2013]). Van Houtte et al. [2014] found that for certain sites there may be a large difference between the κ values on the two components (up to 25%) possibly due to high-frequency site effects, while for other sites, κ measurements may be similar for the two components. Therefore, the vector sum (square root of the sum of the squares), which is orientation-independent, is suggested. A disadvantage of the vector sum method is that the component with the more limited bandwidth controls the *DF*. The vector sum is computed at each frequency as:

$$VS = \sqrt{H_1^2 + H_2^2} \tag{2.3}$$

Smoothing

κ is typically measured on unsmoothed FAS. If the available frequency range for the measurement is sufficiently wide, and if no significant amplification or deamplification is present in the spectrum's fine structure, then the local perturbations superimposed onto the FAS linear decay should not bias the measurement of the slope that is representative of the overall high-frequency decay. Ktenidou et al. [2013] measured κ_{r_AS} on unsmoothed FAS and examined the difference between using a standard linear regression, where all points are weighted equally, and a weighed regression that lowers the weights on outliers (i.e., the points of maximum perturbation along the slope of the FAS). The differences in κ between the two methods were small (generally below 8%). One possible reason for this result was that, in that study, there was sufficient bandwidth ($f_2 - f_1$) to estimate κ. In some datasets, recordings may have limited usable bandwidth (e.g., data from the Transportable Array (TA) typically have a maximum HUF of only 16 Hz due to low sampling rate of 40 samples per second). In these cases, it may be useful to explore the possibility of smoothing the spectra before measuring κ to increase the stability of the slope. The smoothing is best done on the entire spectrum, rather than just on the frequency

range f_1 to f_2; however, a disadvantage is that the uncertainty in the estimate of κ will now depend on the frequency bandwidth used for smoothing.

Frequency Range

In addition to smoothing, a second procedure that may help address band-limited data is the use of a moving frequency window. Typically, when there is sufficient usable bandwidth, κ is measured over the entire usable bandwidth and its mean value is considered representative, while the quality of the measurement may be judged by the standard deviation [Douglas et al. 2010]. Windows of 8 or 10 Hz are recommended, though shorter windows of 6–7 sec have also been used, especially with TA array data [Ktenidou et al. 2013; Kishida et al. 2014]. Recent work has shown that even for bandwidths greater than 10 Hz, results can be sensitive to the choice of frequency window [Edwards et al. 2015]. One way to quantify the sensitivity of the measurement to the choice of window is to perform a series of measurements for a moving window within the available bandwidth. The standard deviation of those measurements gives a good indication of the uncertainty of the mean estimated κ.

This sensitivity analysis can be performed for a large number of windows for recordings with large usable bandwidth. The computed uncertainty can then be applied to band-limited recordings for which we are not able to apply this procedure. The NGA-east dataset includes 50 recordings with available bandwidth above 35 Hz, 110 recordings above 30 Hz, 250 above 20 Hz, 520 above 10 Hz, and 640 above 5 Hz. In this case, we can apply the uncertainty in κ estimated for $DF\_{AS} > 30$ Hz to those with $DF\_{AS} > 5$ or 10 Hz. This uncertainty will likely depend on the type of site (rock or soil) and the noise level. Because rock sites tend to be more variable [W. J. Silva, *personal communication*, 2013; Schneider et al. 1993], a grouping into soil and rock classes may be appropriate. For a small bandwidth of 8 Hz, four moving windows with a width of 5 Hz and an overlap of 4 Hz could be used. For each regression, the standard deviation, coefficient of correlation, and L1 norm can be computed and used later to develop weights for the individual measurements.

Amplification

Parolai and Bindi [2005] caution against measuring κ on a spectrum whose shape is strongly distorted in the high-frequency range by amplification effects due to shallow resonance. They demonstrate the possible bias in κ when measured near a strong resonant peak caused by shallow impedance contrast (an underestimation when measured before the peak, and an overestimation when measured after it). They recommend either avoiding strong resonant peaks in the frequency range where κ is measured, or if that is impossible, measuring it over a wide enough range so that it crosses over several peaks and troughs and is not biased by a single peak or trough. This is particularly easy if the site is soft and the fundamental frequency is low. It is more difficult at hard-rock sites. Recent studies have taken this into account and measured κ over large enough frequency ranges to average out the distortion caused by resonant peaks from shallow structure in the site transfer function (up to 30 Hz or more, e.g., Douglas et al. [2010]; Ktenidou et al. [2013]; and Van Houtte et al. [2014]). In practice, a one-dimensional (1D) model of the recording site V_s profile is rarely available. One approximation, for sites where there are more than about three recordings, is to use the empirical approach of Lermo and Chavez-Garcia [1993] to compute the average horizontal-to-vertical spectral ratio (HVSR) of the site, as an indicator of local site resonance. This has been done for the for Arizona ground-motion data by Kishida et al. [2014] using the both the *S*-wave and coda-wave FAS. The latter HVSR is assumed to give an

estimate of the local site amplification smoothed over azimuth angles. One can determine whether it is possible to achieve an unbiased estimate of κ by studying the resonance pattern within the usable frequency band. If strong broadband amplification or deamplification is observed within the usable frequency, the site can be rejected or the site resonance can be removed before estimating κ; however, it has been shown to be difficult to remove the site-specific resonances, (e.g., Ktenidou et al. [2013]). As an alternative, hard-rock sites can also be grouped according to the shape of their average HVSR, leading to an average κ value for each group.

Another possible approach for minimizing bias in κ estimates from high-frequency resonances would be to stack individual FAS coming from different hard-rock sites to average over the different amplification patterns. This method could be applied within a particular region, taking care to bin recordings by V_S, magnitude, and distance. To our knowledge, stacking of FAS to measure κ has only been used in Kishida et al. [2014]. In that study, FAS of very small magnitude events in Arizona were stacked, not to smooth out local resonances, but to achieve a larger SNR. In that case, the stacking was done using recordings at the same site, coming from a small swarm with similar epicenter and magnitude.

Accounting for shallow resonance due to impedance contrasts in the first few tens or hundreds or meters of the site profile (assuming bedrock at about 1000 m/sec), as described above, is one aspect of site amplification. A second aspect is amplification from the entire crustal profile over several km beneath the site (assuming source V_S at 3500 m/sec). Crustal amplification is often computed based on a simple generic crustal profile through the square-root impedance method (SRI), which follows from the quarter-wavelength velocity [Boore and Joyner 1997] or on random vibration theory (RVT) as applied by Silva and Lee [1987] in RASCALS. How much these two approaches for estimating crustal amplification may differ for a given V_S profile depends on the method used to compute the amplification function. The SRI approach treats the V_S profile as given, while the RVT approach often randomizes the profile to capture profile (lateral) variability which broadens the site resonance. These approaches generally produce a transfer function that is smoother than the transfer function computed for surface soil layers with the reflectivity method, for example, to account for shallow resonances [Boore 2013]; but they still include broadband amplification trends even at high frequencies In the case of RASCALS, it is also possible to include a site-specific, near-surface profile on top of the generic crustal profile, which will include peaks from the near-surface structure as well as trends in the transfer function from the deeper structure.

In summary, for estimating κ, the estimate may be biased either by individual peaks in the transfer function, or by a general broadband trend in the amplification, if those occur within the frequency range of κ measurement. The most important issue is not whether there is amplification or not (i.e., whether the absolute value of the transfer function is equal to 1 or not) over the frequency range of interest, but whether the shape of the amplification transfer function is flat or not within the usable bandwidth. If the transfer function is not flat over the range of frequencies κ is measured (f_1, f_2), then to avoid such bias, one approach is to correct the FAS for the amplification effects before there are fitted for high-frequency log–linear decay. We note that when the transfer function is computed for perfectly elastic media (infinite Q, or zero damping), this correction will only account for the distortion in the shape of the FAS that is due to amplification from impedance contrasts; it does not account for material damping. Therefore, the

κ estimated from the corrected FAS will not correspond to the base of the assumed soil profiles, but to the surface, as the goal is to estimate κ_0.

After correcting the FAS there are three options: (1) measure κ_r individually, which may include some bias from high-frequency resonances; (2) bin the FAS according to magnitude, V_{s30} and distance (the latter only if the FAS are not corrected for regional attenuation) and stack them on a logarithmic scale in order to measure an average κ_r that smoothes through possible resonance peaks; or (3) supplement the regional crustal profiles with detailed site-specific information for sites with measured V_s profiles. In databases where few sites have measured V_s profiles, this allows for a check that compares estimated κ_r values with and without correction for near-surface site conditions.

Regional Attenuation

The final consideration in this step is the effect of regional attenuation on κ. As shown schematically in Figure 2.2, κ_r measurements have path and site contributions to κ. The path component is related to the frequency-dependent anelastic attenuation, $Q(f)$. This can either be taken out of the individual κ_r values in the current step, or it can be estimated in the next step as part of the interpretation for κ. Both approaches have been used in previous studies (e.g., Kishida et al. [2014]) and the results have been compared. Removing the regional $Q(f)$ implies that a $Q(f)$ model for the region has been proposed, and that it can be used to correct the FAS prior to fitting for κ. The FAS corrected for $Q(f)$ does not yield κ_r values, but rather, κ_0 values, because the distance attenuation effect is assumed to have been removed. The FAS can be corrected for path by deconvolving the Q model(s) considered appropriate for the region under study from the FAS; however, correcting the FAS with a $Q(f)$ model will inevitably introduce some uncertainty into the calculation, especially because $Q(f)$ models are generally determined at frequencies lower than where κ is usually measured, and using these models at higher frequencies may require extrapolation.

When sufficient close-in data are available, this issue can be avoided by limiting the recordings used to short distances only. In Van Houtte et al. [2014], for instance, station MQZ recorded over 1000 events at less than 30 km. In most cases, this is not possible. In Kishida et al. [2014], there were only two recordings per site, so different sites were combined, and an average was estimated over all close-in recordings (for the DS method). The maximum distance up to which the effect of path attenuation is negligible depends on the region. More active regions tend to have lower crustal Q values, and so the effect of Q becomes apparent at shorter epicentral distances. For example, in northern Greece, the distance dependence in κ_{r_DS} measurements were observed for epicentral distances larger than about 20 km [Ktenidou et al. 2014]; in southern Arizona, there was no discernible distance dependence in κ_{r_DS} out to 60 km [Kishida et al. 2014]. For WUS and CENA values of roughly 20–30 km and 50–100 km, respectively, are assumed for this study.

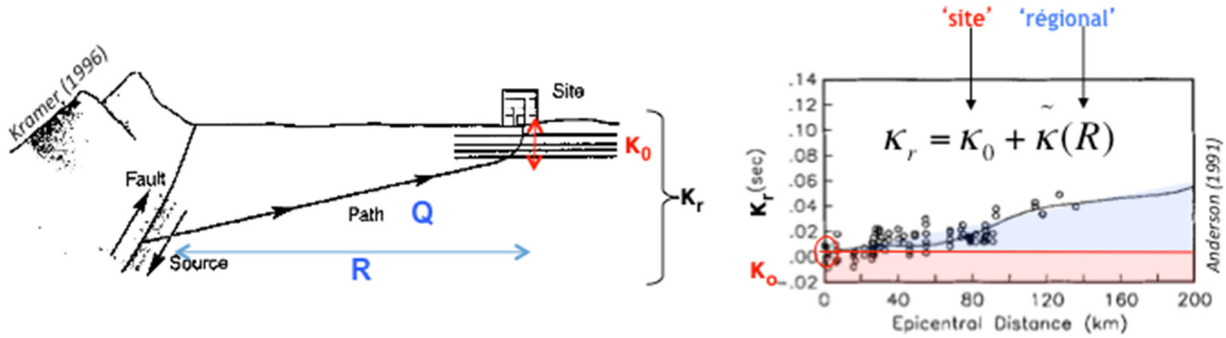

Figure 2.2 Schematic illustration of the path and site components of κ_r.

2.2.3 Step 3: Interpretation and Models

The third step is the interpretation of individual measurements to create an appropriate model for κ. The main considerations are the following.

Depending on the size of the study area, and to interpret individual results, it may be necessary to regionalize them. One may group all sites for which there are κ measurements into zones (for instance, in CENA, a regionalization was proposed by Dreiling et al. [2014]) to study a large area, or one whose crustal properties are known to vary (e.g., attenuation properties, or type of bedrock). In this case, the objective is to analyze recordings that have ray paths within a single region (e.g., Goulet et al. [2014] and the CENA regions), so that the regional effects on attenuation are similar (anelastic Q attenuation and geometrical spreading).

If the regional attenuation is not accounted for in the previous step (i.e., if the individual FAS are not corrected for $Q(f)$ prior to fitting), and if the distance is not negligible, then it should be accounted for in this step. This is done based on observation of the trend of κ_{r_AS} values with epicentral distance. Per Equation (2.2), a linear model may be adequate [Ktenidou et al. 2014]; this model implies a virtually frequency-independent and depth-independent Q within the frequency range over which the κ_{r_AS} measurements were made. The constant Q value can be computed from the slope of the regression of κ_{r_AS} with distance (see Ktenidou et al. [2015] for details) as:

$$Q = 1/\beta\kappa_R \tag{2.4}$$

In other cases, it may be appropriate to modify the linear model at short distances to yield a constant Q value for the first 20–50 km, depending on the maximum distance up to which there is no observable path effect (e.g., Kishida et al. [2014]). This is referred to as bilinear or hockey-stick model. It is based on the assumption that there may be a very high Q zone in the deep to mid-crustal depths where rays paths are recorded in the 30–50 km range [G. P. Biasi, *personal communication*, 2012]. With this assumption, nearby recordings can constrain κ_{0_AS} and more distant recordings can constrain the path effect (the slope of the line). If a simple linear or hockey-stick (bilinear) model does not fit the data, then one can determine a functional form that best fits the data through a non-parametric inversion. Anderson [1991] proposed that any smooth functional form may be possible. One important consideration is that the model chosen to

describe distance dependence does not bias the estimate of κ_{0_AS}, i.e., that the near-field measurements are allowed to determine κ_{0_AS} as much as possible; however, if regional attenuation has been accounted for in the previous step, then κ_{0_AS} values area already available to be averaged (within each zone, if zonation applies).

In deriving the final κ_{AS} model, we may choose not to use equal weights for all of the individual κ_{r_AS} measurements. The statistics from any regression performed in the previous step, can be used to assign weights to each individual measurement. The statistic most appropriate for assigning weights is the error on the slope, based on which κ_{r_AS} is computed [i.e., error on λ in Equation (2.1)]. The goal should be not to eliminate data but to prioritize use of the more robust estimates, especially when data are sparse.

In deriving κ_{AS} models when site conditions vary significantly among the stations then grouping recordings by site classification may be appropriate. Because soil damping is probably in the κ_{r_AS} measurements, it is appropriate to not treat all sites in one group (unless data paucity requires it). Bins based on V_{s30} or NEHRP site class, or some other site parameter, can be used. If the excitation level varies significantly, including high-amplitude recordings, that may include nonlinear soil behavior, then (at least for soil sites) bins by excitation level are appropriate.

Finally, we note that in the context of projects and applications, κ_0 can be defined at different depths beneath the site. This process yields κ_0 at the surface of the soil profile, as shown in Figure 2.3. This estimate does not include crustal amplification, but it does include damping within the soil layers, and any effects from scattering (see Ktenidou et al. [2015] for a discussion on scattering contribution to κ_0). If we remove the damping and scattering contributions in the soil layers, then we estimate κ_0 at the top of "rock," in the sense that "rock" is used in some projects to define the depth for the input motion. If we further remove estimates of damping and scattering contributions to the base of the crustal model (source depth with V_s = 3500 m/sec), then an estimate of crustal κ_0 may be obtained (e.g., 0.006 sec for CENA). It is important to consider which level (depth) we compute κ_{0_AS} at in order for this approach to yield consistent results with the broadband approaches described later.

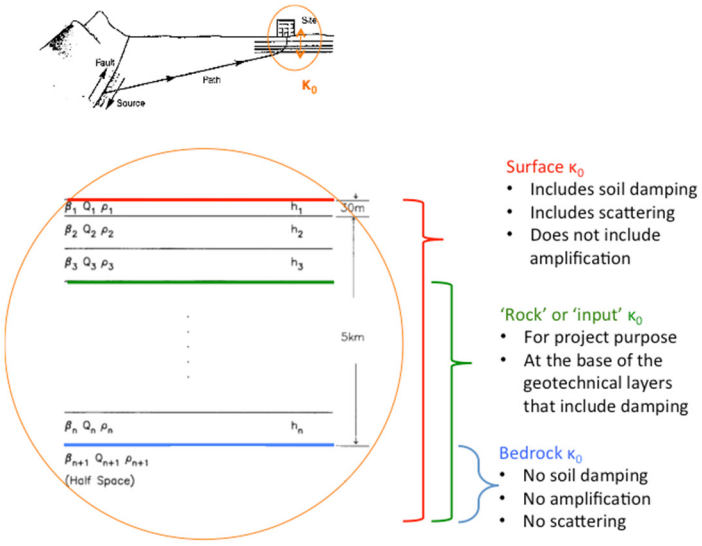

Figure 2.3 Schematic definition of κ_0 at different levels: surface, rock/input, and bedrock.

2.3 THE BAND-LIMITED APPROACH 'DS'

The traditional approach [Anderson and Hough 1984] uses relatively large-magnitude earthquakes to measure spectral decay above f_c. Biasi and Smith [2001] proposed an approach that expands the method to smaller magnitudes, where data are more abundant. They measure κ_r directly on the displacement FAS, using frequencies below the (rather high) f_c, in contrast to using the acceleration FAS and using frequencies above the (rather low) f_c. Rather than measuring κ_r as the departure of the acceleration spectrum from a horizontal line (κ = 0 sec, no attenuation), we use recordings from smaller earthquakes and measure κ_r as the departure of the displacement spectrum from a horizontal line (κ =0, no attenuation) over potentially the same frequency range.

One advantage of this method is that the theoretical basis for assuming the displacement spectrum at the source as flat below f_c is actually stronger than the basis for treating the acceleration spectrum as flat above f_c, as the latter depends on the validity of the ω^{-2} assumption [J. G. Anderson, *personal communication*, 2013]. We use κ_{r_DS} to denote these estimates, and the extrapolated zero-distance site parameter as κ_{0_DS} (also referred to as κ_{0_mini}).

The frequency range in which κ_{r_DS} can be measured begins at the lowest usable frequency (f_{1_DS} = LUF) and extends up to f_c. However, applying the same factor of safety of 1.5 as for the AS approach, to avoid trade-off with the source, the upper frequency cut-off is at $f_{2\_DS} = f_c/1.5$. The three steps in the AS approach are applicable to the DS approach apart from this difference in the definition of the bandwidth.

2.4 THE BROADBAND APPROACH 'BB'

Several authors have used broadband inversion schemes (using the entire useable frequency band) to compute κ. These methods assume a source spectral shape to estimate κ_r and account for the source, path and site effects in various ways so as to yield individual values of what we denote as κ_{r_BB}. These values may then be extrapolated to κ_{0_BB}. One advantage of broadband inversions is that, unlike the traditional approach, they are not constrained as much by the event magnitude (i.e., they can also be used when the earthquake corner frequency is within the frequency band used for κ measurement). Therefore, they can use more of the abundant small-magnitude earthquake data in the inversion. Numerous broadband inversion schemes are in literature. Anderson and Humphrey [1991] invert for f_c (or stress drop), spectral level, and κ_{r_BB}, assuming a smooth spectral shape to partly overcome the trade-off with stress drop. Humphrey and Anderson [1992] perform the broadband inversion after removing the empirical or modeled site response from each spectrum. Based on a method by Scherbaum [1990], Edwards et al. [2011] use a simultaneous broadband inversion of the velocity spectrum resolving for f_c, moment, and κ_{r_BB}. Finally, the approach introduced by Silva et al. [1997] is unique, as it yields either a site-specific or a site-class-specific estimate of κ_{0_BB}.

In this study, we use the approach of Silva et al. [1997]. This inversion method estimates the earthquake source, path, and site parameters through a nonlinear least-squares fit to the FAS, using the point-source model [Boore 1983; EPRI 1993]. The useable bandwidth is site- and earthquake-specific, based on a visual examination of the pre-event FAS noise levels compared to the windowed shear-wave FAS and with the maximum frequency constrained by either the

noise or the anti-alias filters in these analyses. Typically, the inversion bandwidth is magnitude dependent, extending to lower frequency as magnitude increases and averaged around 0.8 Hz above **M**2, and around 1.0 Hz below **M**2 for these CENA data. The inversion scheme treats multiple earthquakes and sites simultaneously with the common crustal path damping parameter $Q(f)$. The parameter covariance matrix is examined to determine which parameters may be resolved for each dataset and asymptotic standard errors are computed at the final iteration.

The model parameters include R_c (cutoff distance from $1/R$ to $1/R^{0.5}$ for geometrical spreading), $Q(f) = Q_0 \bullet f^{\eta}$ (where Q_0 is the value at 1 Hz), $\Delta\sigma$ (the stress parameter in the point-source ground motion model), the Brune point-source shear-wave velocity (β) and density (ρ), **M**, and linear-elastic crustal amplification. Inversion parameters that may be determined by the data include Q_0, η, R_c, κ_{0_BB}, **M**, and/or stress parameter (f_c). For datasets with insufficient distance range, strong parameter coupling may necessitate fixing $Q(f)$ and occasionally R_c; there may also be a trade-off between anelastic attenuation and geometrical spreading, so these two coupled parameters should be consistent with one another.

The procedure uses the Levenberg-Marquardt algorithm [Press et al. 1986] with the inclusion of the second derivative. Linear-elastic crustal profile amplification is accommodated in the inversion scheme by incorporating the appropriate rock or soil transfer functions (shear-wave velocity and density profile from source depth (assumed to be 8 km) to the surface) in estimating the point-source surface spectra. To reduce the potential for non-uniqueness inherent in inversion results, a suite of starting models is employed. The final set of parameters is selected based upon a visual inspection of the model fit to the FAS, the chi-square values, and the parameter covariance matrix. The stress parameter from the inversion is calculated from the moment using equation:

$$f_c = \beta \left(\frac{\Delta\sigma}{8.44 \cdot M_0} \right)^{1/3} \tag{2.5}$$

The inversions are performed on log amplitude spectra (the orientation independent vector average of the two horizontal components), as strong ground-motion data appear to be log-normally distributed. This is consistent with the model being represented as a product (rather than sum) of models [EPRI 1993]. A feature of the inversion scheme is the flexibility to distinguish between sites, for which κ_{0_BB} is determined, and stations for which recordings are available. As a result, several stations may share a common site or κ_{0_BB} estimate, for example, based on NEHRP classification.

To assess the stability of κ_{0_BB} and estimate its epistemic uncertainty, it is possible to run a suite of inversions, modifying some of the other model parameters by realistic amounts, such as the $Q(f)$ model and crustal amplification. Note that all other inversion parameters, such as **M** and $\Delta\sigma$, will change along with κ_{0_BB}. As an example, Kishida et al. [2014] showed that changing the $Q(f)$ model did not have a significant impact on κ_{0_BB}, although varying the frequency-independent constant Q (e.g., in the band-limited approaches AS and DS) had a significant impact of the estimated κ_{0_BB}. In the same study, the sensitivity of κ_{0_BB} to the crustal amplification correction was small. They found that the parameter most strongly affected by this

correction was the **M**. The sensitivity of κ_{0_BB} to different parameters may be different for other datasets. In addition, κ_{0_BB} may be sensitive to different parameters compared to κ_{0_AS} (e.g., in the same study, κ_{0_AS} and κ_{0_DS} were more sensitive to variations in the crustal amplification correction).

A second approach to assess the uncertainty in κ_{0_BB} is to perform inversions with different subsets of the data (jackknife approach). This approach, however, requires a sufficient amount of data.

A third approach is to investigate the effect of smoothing on the estimated values. Inversions may be done on FAS with smoothing that uses either a constant frequency increment (CFI) or a constant logarithmic frequency increment (CLFI). The former (CFI) produces an increased number of points at high frequencies. The latter (CLFI) results in a uniform distribution of points at both high and low frequencies. Inversions using CFI result in increased weighting at high frequencies, emphasizes parameters such as κ, stress parameter, and $Q(f)$ at larger distances, compared to magnitude (**M**). Such unequal weighting is most appropriate at large magnitude where the point-source model tends to over-predict low-frequency motions [EPRI 1993; Silva et al. 1997; and Atkinson and Silva 2000]. Increased weighting at high frequencies for large-magnitude recordings places more emphasis over the frequency range where the point-source model works well, conversely decreasing the emphasis where the model does not perform as well. CLFI smoothing results in equal weighting across the inversion bandwidth and is more appropriate for small-magnitude recordings, where the point-source model appears to work equally well at both high and low frequencies for these small magnitude earthquakes.

2.5 THE RESPONSE SPECTRAL SHAPE APPROACH

This is a second approach that makes use of the entire frequency band. In contrast to the classical approach [Anderson and Hough 1984], which relates κ to the decay of the high-frequency part of the FAS. This approach relates it to the spectral shape of the normalized response spectrum (RESP) that uses stochastically generated 5% damped pseudo-acceleration response spectra (PSA), where κ_0 is one of the point-source model input parameters (applied to the entire frequency range). The PSA are computed with the appropriate site amplification from the site profile. These point-source spectra are then normalized with respect to peak ground acceleration (PGA) and compared to observed response spectra. Thus we can estimate the input κ (we denote this one κ_{0_RESP}) that gives the best fit between these spectra. The entire frequency band is used for the fitting and not just the high-frequency part. Emphasis is placed on the location of the peak in the spectra (which depends on the input κ) and the width (which depends on **M**). Trade-offs between κ_0 and stress drop are avoided to a degree, as the PSA are normalized by PGA (spectral shape) and then averaged [Hiemer et al. 2011; Silva and Darragh 1996]. The use of response spectral shapes (5%-damped PSA/PGA) computed from recordings made at rock sites at close distances to estimate κ was developed by Silva and Darragh [1996] and Silva et al. [1997]. Differences in response spectral content or shape at different sites are significant and may be interpreted as primarily resulting from differences in the V_s (amplification) and damping (κ) beneath the site along with crustal $Q(f)$, especially at larger distances (> about 20 km for small

M) [Boore and Atkinson 1987; Toro and McGuire 1987; Silva and Green 1989; and Silva and Darragh 1996].

Pseudo-acceleration response spectra have a strong magnitude dependence, with smaller earthquakes having a narrower bandwidth and higher frequency peaks than larger earthquakes. This is a consequence of the lower corner frequencies for smaller magnitude earthquakes [Boore 1983; Silva and Green 1989; Silva 1991; and Silva and Darragh 1996]. Spectral shapes from multiple recordings at similar distances and magnitudes are averaged to reduce the frequency-to-frequency variability and provide additional stability in κ estimates [Silva and Green 1989; Silva and Darragh 1996]. These factors allow estimates of κ to be made from PSA shapes by visual comparison with the simulated spectral shape from the point-source model.

Silva and Darragh [1996] noted that the frequency where the PSA peaks provides an estimate of the site κ_0 value. Figure 2.4a (adapted from Silva et al. [1998]) shows simulated PSA (left) and spectral shape (right) for an earthquake with **M**6.5 at 25 km, for the western U.S. (WUS) parameters (65 bar). The simulations were made with the point source stochastic model (per Boore [1983] as validated by Silva et al. [1997]). For κ_0 = 0.04 sec (which is a typical for soft rock in WUS) the PSA peaks at around 5 Hz (red line). As κ_0 decreases, the frequency where the PSA peaks increases; e.g., for I_0=0.02 sec, it peaks around 10 Hz, and for κ_0=0.005 sec (a typical value for hard rock in CENA), it peaks around 40 Hz (blue line). Silva [1991] noted that a factor of two in κ_0 is reflected in a factor of two change in peak frequency in the response spectra.

Figure 2.4b shows PSA and normalized spectral shape for CENA rock conditions (110 bar), with unity crustal amplification and for a range of κ values appropriate for CENA rock (5–20 m/sec). Again, the peak frequency and shape of the response spectra clearly shift to lower frequency as κ increases. We also note that at 100 Hz not all of the spectral shapes converge to 1.0 (PGA), which indicates that in such conditions (hard rock and close-in distance), PGA may be observed at frequencies higher than 100 Hz.

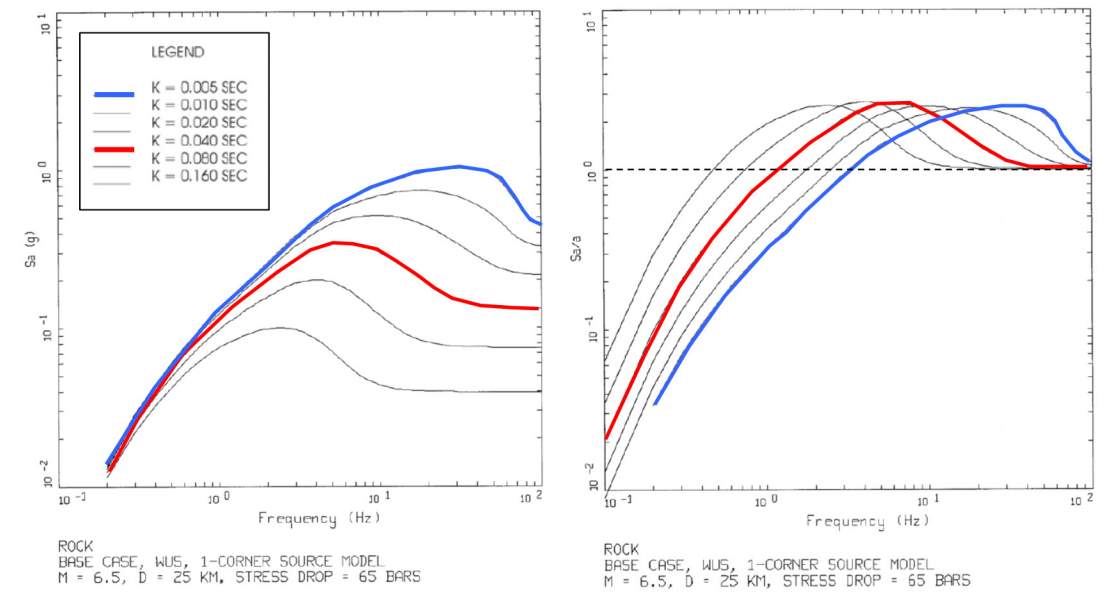

(a)

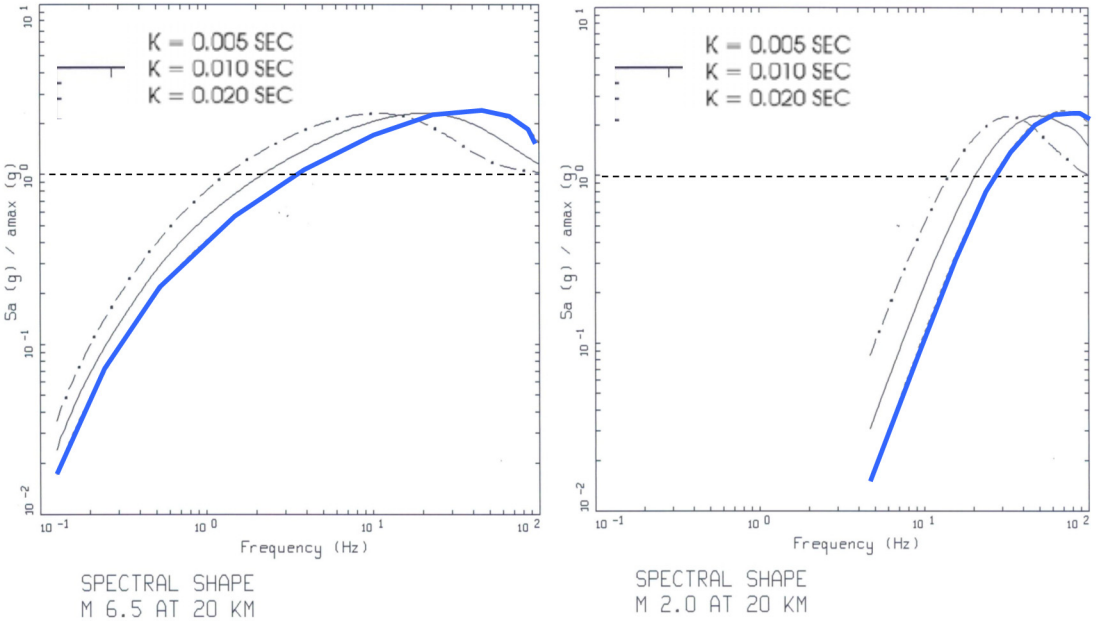

(b)

Figure 2.4 **(a) 5%-damped response spectra (left) and normalized response spectra (right) for M6.5 earthquake at 25 km for a suite of κ_0 values using WUS parameters and $\Delta\zeta$ = 65 bar (adapted from Silva et al. [1998]). Red represents typical values for WUS, blue for CENA; and (b) 5%-damped normalized response spectra for M6.5 (left) and M2.0 (right) earthquake at 20 km, for a suite of κ_0 values using CENA parameters and $\Delta\sigma$=110 bar.**

2.6 CHOOSING APPROPRIATE RECORDINGS FROM LARGE DATASETS FOR THE BAND-LIMITED APPROACHES

Sections 2.2.1 and 2.2.2 document the constraints that apply to the frequency band that can be used for the AS and DS approaches pertaining to the usable data bandwidth and stress drop or corner frequency. Approach AS measures κ above f_c, for relatively large magnitude events. Although typically used for magnitudes above about **M**4, it may be extended towards lower magnitudes depending on the stress drop and the available bandwidth of the data. For instance, studies in the 1980s often used data with **M**5 or above because of the relatively lower sampling rates and resulting lower Nyquist frequency values that afforded only a small usable bandwidth. Using more recent data, the minimum usable magnitude has dropped in cases where the larger bandwidth due to higher sampling rates compensates for higher f_c values [Ktenidou et al. 2013; and Van Houtte et al. 2013; 2014]. The DS approach measures κ below f_c, for small magnitude events. There are not many published studies using this approach, but the following suggest that it is best used for magnitudes below about **M**1 [Kilb et al. 2012; Biasi and Smith 2001; G. P. Biasi, *personal communication*, 2013; and Kishida et al. 2014].

When working with large datasets (such as NGA-West 2, NGA-East, KikNet, etc.), much of the data may fall between the magnitude limits of the two band-limited κ approaches. If we want to use only data with large magnitudes (e.g., above **M**5), we may assume that most recordings will be appropriate for the AS approach and start analyzing the data directly. However, if we also want to use data for magnitudes smaller than about **M**4, particularly for voluminous datasets, it is advisable before proceeding with data analysis to first scan the available metadata for recordings where the AS and DS approaches might be most appropriate. The concern is that, the lower the magnitude, the effect of the uncertainty of the stress drop on f_c is larger. Because we require an estimate of f_c in order to determine the usable bandwidth appropriate for each method, we propose an approach for choosing subsets for which we can apply each of the two approaches (AS and DS), with the goal of analyzing as much data as possible.

We first defined a plausible range (minimum and maximum) of stress drops for the region. This can be done in a variety of ways (e.g., through literature search, or spectral analysis, etc.). For each approach (AS and DS), we fixed the stress drop so as to maximize the data in each subset. To push the AS approach to as low a magnitude as possible, we assumed the minimum stress drop ($\Delta\sigma_{\min}$) because that yields the lowest f_c ($f_{c\min}$). Conversely, to push the AS approach to as high a magnitude as possible, we assumed the maximum stress drop ($\Delta\sigma_{\max}$), as that yields the highest possible f_c ($f_{c\max}$). These choices generate a small subset of recordings belonging to both the AS subset and the DS subset. These are the recordings for which there is the highest uncertainty that f_c may lie within the usable bandwidth, and concern over which of the two approaches is the most appropriate. Therefore, use of both approaches provides a range of possible values for κ and assists in the assessment of epistemic uncertainty.

This procedure defines the required frequency range for the analyses, which may or may not be available based on the record noise, filtering (anti-alias and noise), etc. So for each of the two cases ($f_{c\ \min}$, $f_{c\ \max}$) we checked whether the source f_c lay within the usable bandwidth of the record, and whether there was an adequate overlap between the usable frequency range (defined by the HUF and LUF) and the required frequency range in which we can measure κ. For small-magnitude events and relatively high stress drops, frequently there is no overlap, or if there is, it

may be inadequate [e.g., less than 8–10 Hz (minDF)]. Therefore, for large databases it is important to first scan the metadata (flatfiles) based on these frequency parameters to create subsets for which each of the approaches (AS and DS) may be used.

For the AS approach, we assumed $\Delta\sigma_{\min}$ to compute f_c ($f_{c\min}$). To avoid any trade-off with the source, the frequency range in which κ_{r_AS} is measured began at $f_{1\_AS} = 1.5 f_{c\min}$ and ended at the highest usable frequency. The required bandwidth for this approach was then:

$$DF_{\_AS} = \text{HUF-1.5} \bullet f_{c\min} \tag{2.6}$$

For the DS approach, we assumed $\Delta\sigma_{\max}$ to compute f_c ($f_{c\max}$). Again, to avoid trade-off with the source, the frequency range in which κ_{r_DS} was measured began at the lowest usable frequency and extended up to $f_{2\_DS} = f_{c\max}/1.5$. The required bandwidth for this approach was then:

$$DF_{\_DS} = f_{c\max}/1.5 - \text{LUF} \tag{2.7}$$

Fixing the stress drop and using the appropriate metadata, we computed DF_AS and DF_DS for every recording in the database. The required bandwidth only exists when these values are positive; this occurs only for large events in the first case and for small events in the second case. Furthermore, as discussed in Section 2.2.2, for a meaningful and robust estimate of κ, we require that DF_AS and DF_DS exceed a minimum value, which we designate as minDF.

To compute f_c for each of the two cases, we used the point-source stochastic model (PSSM) of Boore [1983]. Assuming that Brune's [1970, 1971] ω^2 source model and Aki's [1967] scaling law hold, then

$$f_{c\max} = 4.9 \cdot 10^6 \beta \left(\frac{\Delta\sigma_{\max}}{M_0} \right)^{1/3} \tag{2.8}$$

$$f_{c\min} = 4.9 \cdot 10^6 \beta \left(\frac{\Delta\sigma_{\min}}{M_0} \right)^{1/3} \tag{2.9}$$

where β is shear-wave velocity at the source (taken as 3.5 km/sec), and M_0 is the seismic moment, computed from moment magnitude **M** as follows:

$$M_0 = 10^{1.5M + 16.05} \tag{2.10}$$

3 Data Selection and κ Estimation for Rock Sites in the NGA-East Database: Example Application

3.1 SCOPE

The previous chapter presented a detailed methodology for estimating κ. This chapter presents an example application but with several of the considerations described in Chapter 2 simplified. κ_0 for recordings from the NGA-East database are estimated. For the purpose of this exercise (data selection), only sites with $V_{s30} \geq 1500$ m/sec (rock and mainly hard rock) are considered. Distances are also limited to a maximum epicentral distance of R_e =50 km, to reduce the contribution of path attenuation (effect of Q discussed in Section 2.2.3). The κ_0 values measured in this exercise will be used in the following chapters to study residuals and high-frequency ground motions for hard-rock sites.

3.2 BAND-LIMITED APPROACHES 'AS' AND 'DS'

3.2.1 Example Application for Selecting NGA-East Rock and Hard-Rock Sites ($V_{s30} \geq 1500$ m/sec)

There are few recordings in the NGA-East dataset at large magnitudes (above **M**5). A significant amount of data lies between **M**2 and **M**4, i.e., between the magnitude limits of the two band-limited κ approaches: AS and DS as described in Section 2.6. Furthermore, there exists large uncertainty as to the values of stress drop for CENA, especially for small magnitude earthquakes where this parameter is not commonly estimated. For magnitudes **M**2–**M**4, this translates into large uncertainty in f_c in this application. These data restrictions make CENA a good case study to illustrate the necessity of the proposed pre-processing of the database flatfile prior to undertaking κ computations. The selection of appropriate subsets from the NGA-East flatfiles for estimating κ in CENA using AS and DS approaches is discussed below.

In assigning values for $\Delta\sigma_{min}$ and $\Delta\sigma_{max}$, the results of various studies in the CENA region have been considered. Given the possible differences between the studies' input parameters, and particularly the path functions [Boore et al. 2010], a single mean value is unlikely; therefore, a range of credible values will be used. For CENA, we considered the following:

- According to the studies of A. Baltay and T. Hanks [2013, *personal communication*], the mean stress drop in CENA is around 100 bar (10 MPa).
- In Boore [2012], the mean stress drop for this dataset is either 113 or 90 bar, depending on whether Saguenay mainshock is included or not. Some events have stress drops as low as 30 bar in this study. The highest value is for the Saguenay mainshock, and it is close to 500 bar (50 MPa).
- According to Boore [2009], the value for use in the PSSM that is most consistent with Atkinson and Boore [2006] is 250 bar (25 MPa).
- Atkinson and Boore [2014] found geometric attenuation of $R^{-1.3}$ at distances less than 50 km, leading to higher stress drop values than the previous studies. Their mean value is 500–600 bar for events above **M**4.5. However, they also found some magnitude dependence to their stress drop values (which they consider a valid conclusion rather than an artifact). Because our dataset comprises mainly smaller events, we select their mean estimate as our maximum estimate.
- According to Boatwright [2014], the average stress drop over their entire dataset is 114 bar, and the regional averages are 215, 88, and 39 bar for Eastern Quebec, Western Quebec, and Northeastern U.S., respectively. The latter two regions also include some events with stress drops as low as 20 bar (2 MPa).
- In Eastern Quebec, there are indications of depth (but not magnitude) dependence of stress drop [Boatwright 2014]. Based on the NGA-East flatfile, the depth dependence in that region is investigated. The region is defined as north of N45° and east of W70°. Figure 3.1a shows the depths of all events in the entire dataset. The events located in Eastern Quebec are marked in red. The event depths in that region span a large range of values (5–22 km). Within this range, the stress drop in the region is strongly depth-dependent, as shown in Figure 3.1b.

Based on these observations, a distinction between Eastern Quebec and the rest of CENA is made. For the rest of CENA, a credible range of stress drop values between 20 and 500 bar, log-normally distributed around a mean value of 100 bar is assumed. So $\Delta\sigma_{min}$ is fixed at 20 bar (2 MPa) and $\Delta\sigma_{max}$ is fixed at 500 bar (50 MPa) (see blue dashed lines in Figure 3.1) and f_{cmin} and f_{cmax} are computed accordingly, irrespective of depth. Due to the depth dependence of the stress drop, the envelopes for Eastern Quebec—shown as the orange dashed lines in Figure 3.1—are followed. $\Delta\sigma_{min}$ ranges from 30–110 bar and $\Delta\sigma_{max}$ ranges from 300–1050 bar for source depths ranging from 5–22 km. Based on these stress drop values, f_c values are calculated and the dataset is scanned for usable recordings for the AS and DS approaches. Figure 3.2 shows the assumed corner frequency with magnitude and the assumed stress drop with depth. The events deviating from the trends are located in Eastern Quebec.

Figure 3.3 shows the epicenters and recording stations for the CENA dataset for all distances, distances less than 200 km, and distances less than 50 km. More than 85% of the data

come from distances greater than 200 km. The figure also uses a color code to indicate the type of site according to NEHRP site classification. Most NEHRP A and B sites are located in Canada, while the US sites are mostly NEHRP C and D classification. Table 3.1 shows that the number of data diminishes as constraints on the maximum distance are imposed.

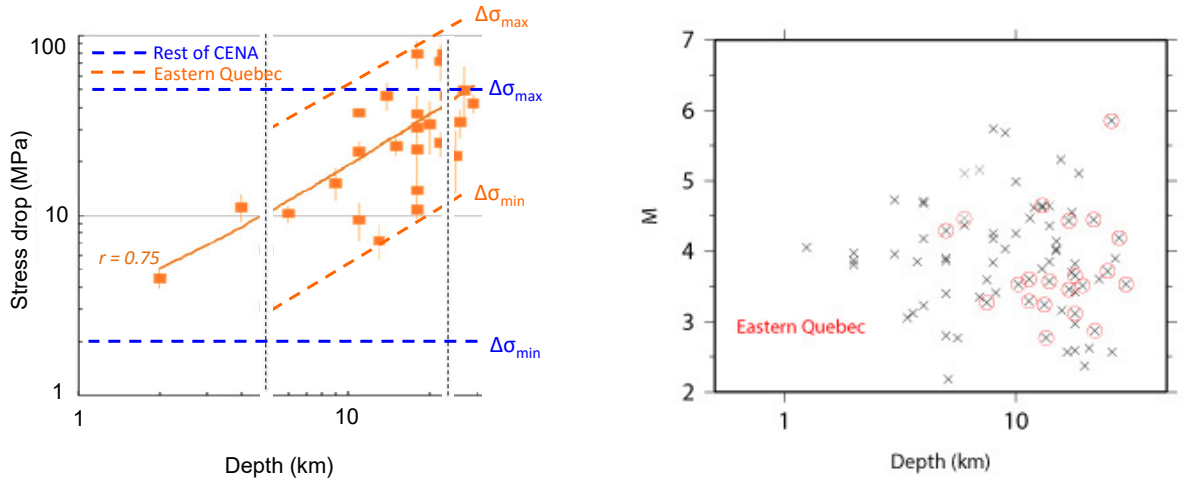

Figure 3.1 **(a) Stress drop dependence with event depth in Eastern Quebec after Boatwright [2014]. Dashed lines mark the chosen maximum and minimum credible values, $\Delta\sigma_{min}$ and $\Delta\sigma_{max}$, for Eastern Quebec (orange) and the rest of CENA (blue).; and (b) magnitude-depth distribution for all events in the dataset, with events from Eastern Quebec shown in red.**

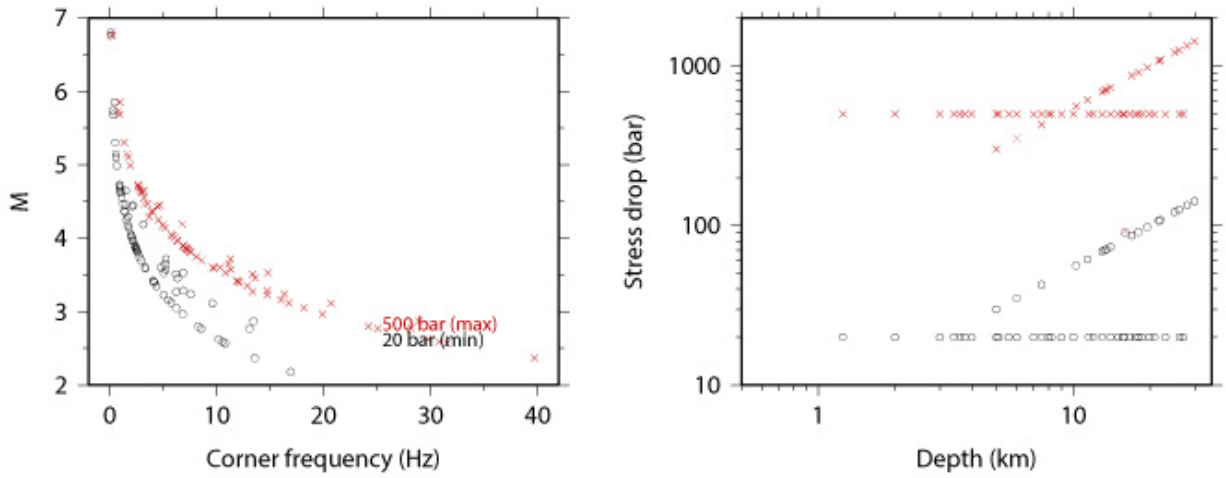

Figure 3.2 **(a) Corner frequency for all events in the dataset, for $\Delta\sigma_{min}$ (black circles) and $\Delta\sigma_{max}$ (red crosses). Those that deviate from the constant-stress-drop lines correspond to events in Eastern Quebec; and (b) stress drop versus event depth for all events in the dataset, for $\Delta\sigma_{min}$ (black circles) and $\Delta\sigma_{max}$ (red crosses). Those that show depth-dependence correspond to Eastern Quebec events.**

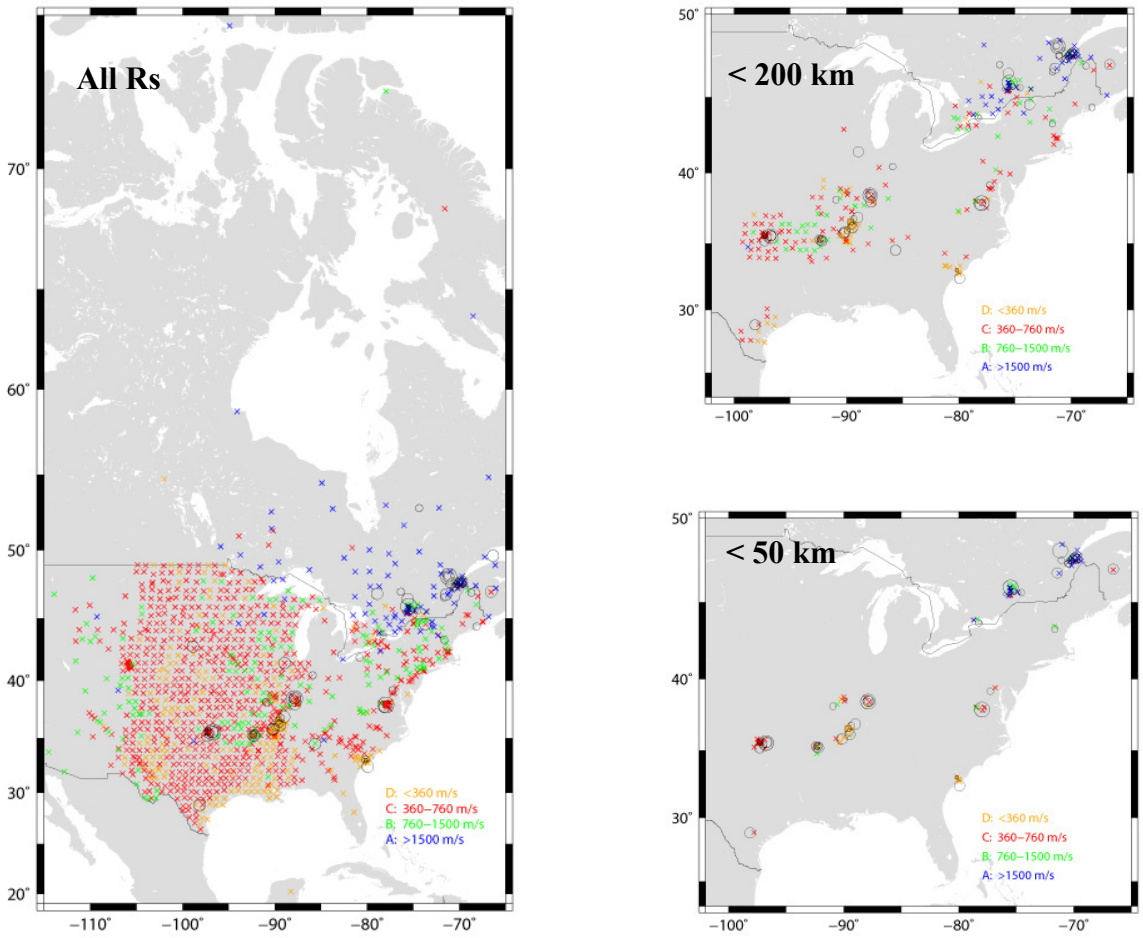

Figure 3.3 **Epicenters and recording stations for the CENA dataset for all distances, for distances less than 200 km, and for distances less than 50 km.**

Table 3.1 **The decrease in the number of recordings, events, and stations for all NEHRP site classifications as various distance constraints are used.**

	All	$R \leq 200$ km	$R \leq 50$ km
Recordings	9384	834	223
Events	84	77	60
Stations	1272	277	95

Figure 3.4a shows the LUF (red) and HUF (black) for each record in the database versus magnitude and the available bandwidth between them (Figure 3.4b) for different maximum distance constraints. Figure 3.5 shows the LUF and HUF together with the assumed corner frequencies. The left panel shows f_c for $\Delta\sigma_{min}$ (small blue squares) and their values increased by a

factor of safety of 50% (large blue squares) to avoid source effects. The right panel shows f_c for $\Delta\sigma_{max}$ (cyan), which are decreased by 50% to avoid source effects.

Figure 3.6 shows the available data for the AS approach. Figure 3.6a shows HUF and LUF together with 1.5*f_{cmin}, for all recordings that have an available usable bandwidth DF_AS ≥ 10 Hz. The minimum magnitude is **M**2.4. The number of recordings drops to 12% of the total when the maximum 200 km distance criterion is applied (moving from top to bottom). Figure 3.6b shows the DF_AS values for all recordings (red indicates that the bandwidth is adequate).

Figure 3.7 shows the same for the DS approach. Figure 3.7a shows LUF, HUF, and f_{cmax}/1.5 values for recordings that have adequate DF_DS range (≥ 10 Hz). The maximum magnitude is **M**3.3. The number of recordings drops to 35% of the total when the distance is limited to 200 km or less (moving from top to bottom). Figure 3.7b shows the available bandwidth DF_DS (red for sufficient bandwidth).

Figure 3.8 shows recordings that have adequate DF_AS range (≥ 10 Hz) and separates them into NEHRP site classes A through D. Figure 3.9 shows recordings that have adequate DF_DS range (≥ 10 Hz). The overlapping of the two groups is shown in red. The magnitude range for the overlapping recordings is **M**2.4–**M**3.2; for short distances, these recordings are from mostly for hard sites (NEHRP A and B).

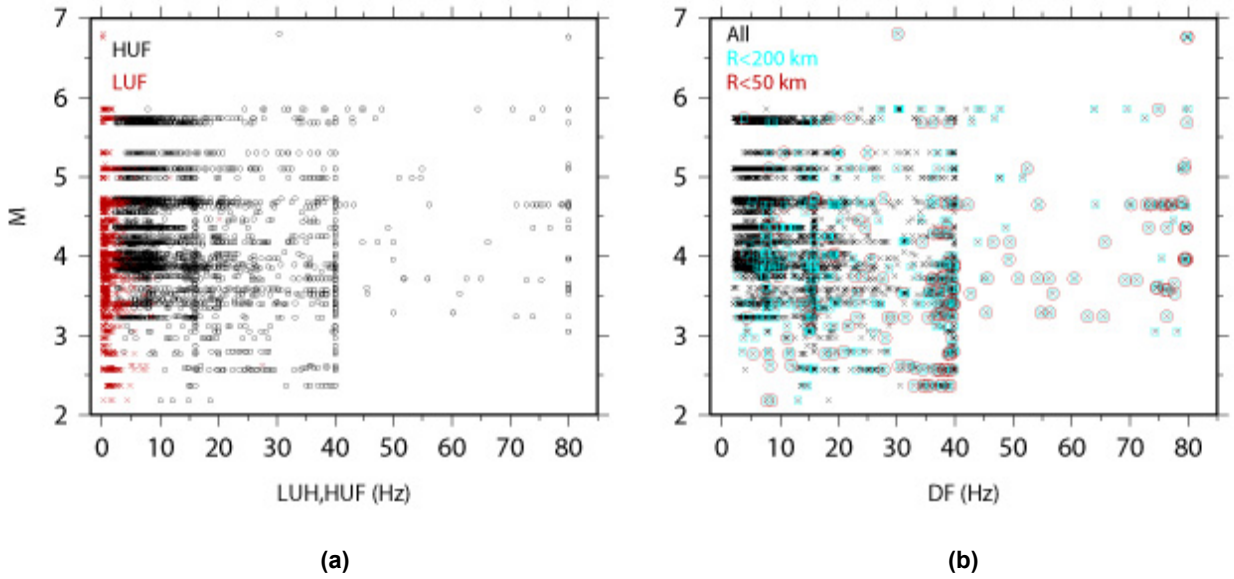

Figure 3.4 **(a) Highest and lowest usable frequency; and (b) available bandwidth between these for different maximum distances.**

In the NGA-East dataset, there is a dramatic data decrease when the maximum distance decreases. For large distances, the total attenuation measured (κ_r) is caused mostly by regional anelastic path attenuation $\left[Q(f)\right]$ rather than site attenuation (κ_0). Therefore, the choice of a maximum distance is critical; this distance could be e.g., 50 km (which is rather restrictive but avoids nearly all path attenuation issues) or 200 km (which includes more distant data with the caveat that there will be some trade-off with the path and κ estimate). The vertical lines in Figures 3.8 and 3.9 indicate that most of the data with usable bandwidth (≥ 10 Hz) are not very useful in estimating the site-specific component, κ_0 due to distance. For those sets with adequate DF_AS and DF_DS, Tables 3.2 and 3.3 show the number of data available as maximum distance constraints are imposed. Figures 3.10 and 3.11 show the epicenter and station location for the recordings with available bandwidth in the AS and DS case, respectively.

Finally, only recordings that have both horizontal components are included because the vector-sum (VS) of the horizontal spectrum is used to avoid the observed orientation dependence of the κ estimates. Problematic recordings based on flatfile flags are also rejected. These flags include late *S*-wave triggers, bad time history, poor FAS quality, high-frequency noise, or aftershocks in the time history.

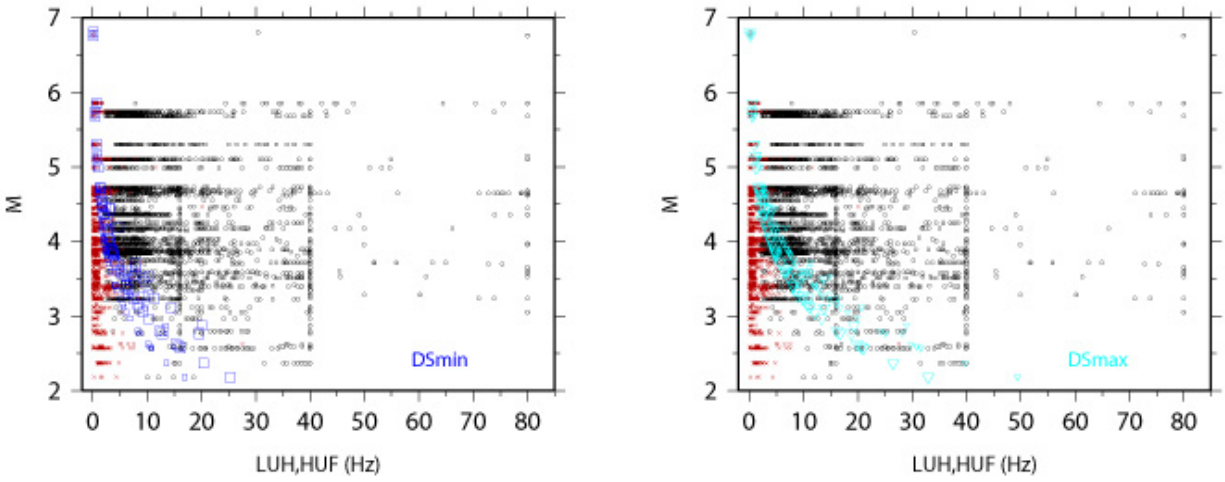

Figure 3.5 **(a) Highest and lowest usable frequency, and corner frequencies f_{cmin}; and (b) f_{cmax} (right) for minimum and maximum credible stress drop. The large symbols indicate the application of a factor of safety of 50%, increasing f_{cmin} and decreasing f_{cmin}.**

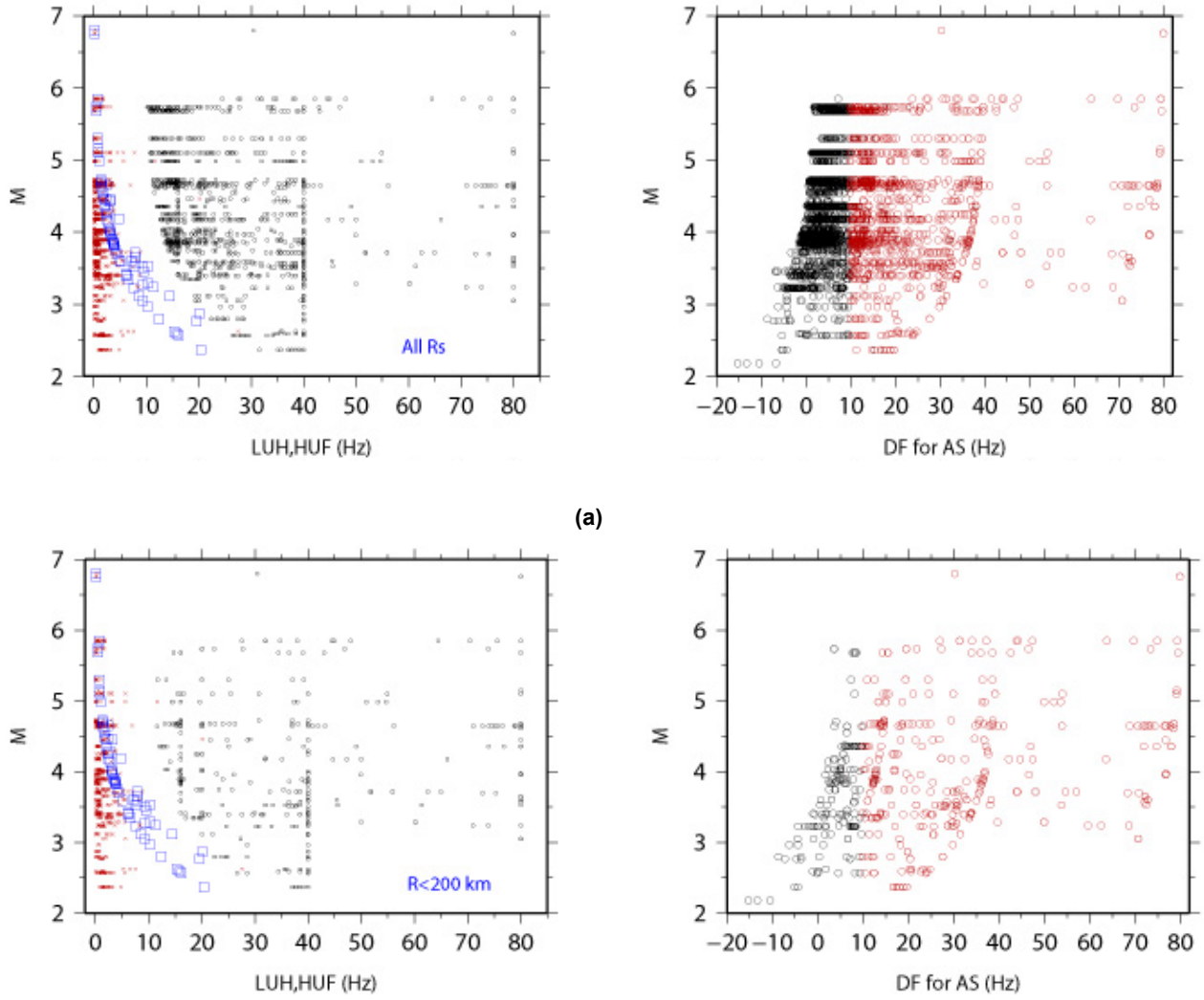

Figure 3.6 **(a) LUF, HUF, and 1.5 • f_{cmin} values for record with available DF_$_{AS}$ ≥ 10 Hz; and (b) corresponding DF_$_{AS}$ values for all distances (top), and for distances less than 200 km (bottom).**

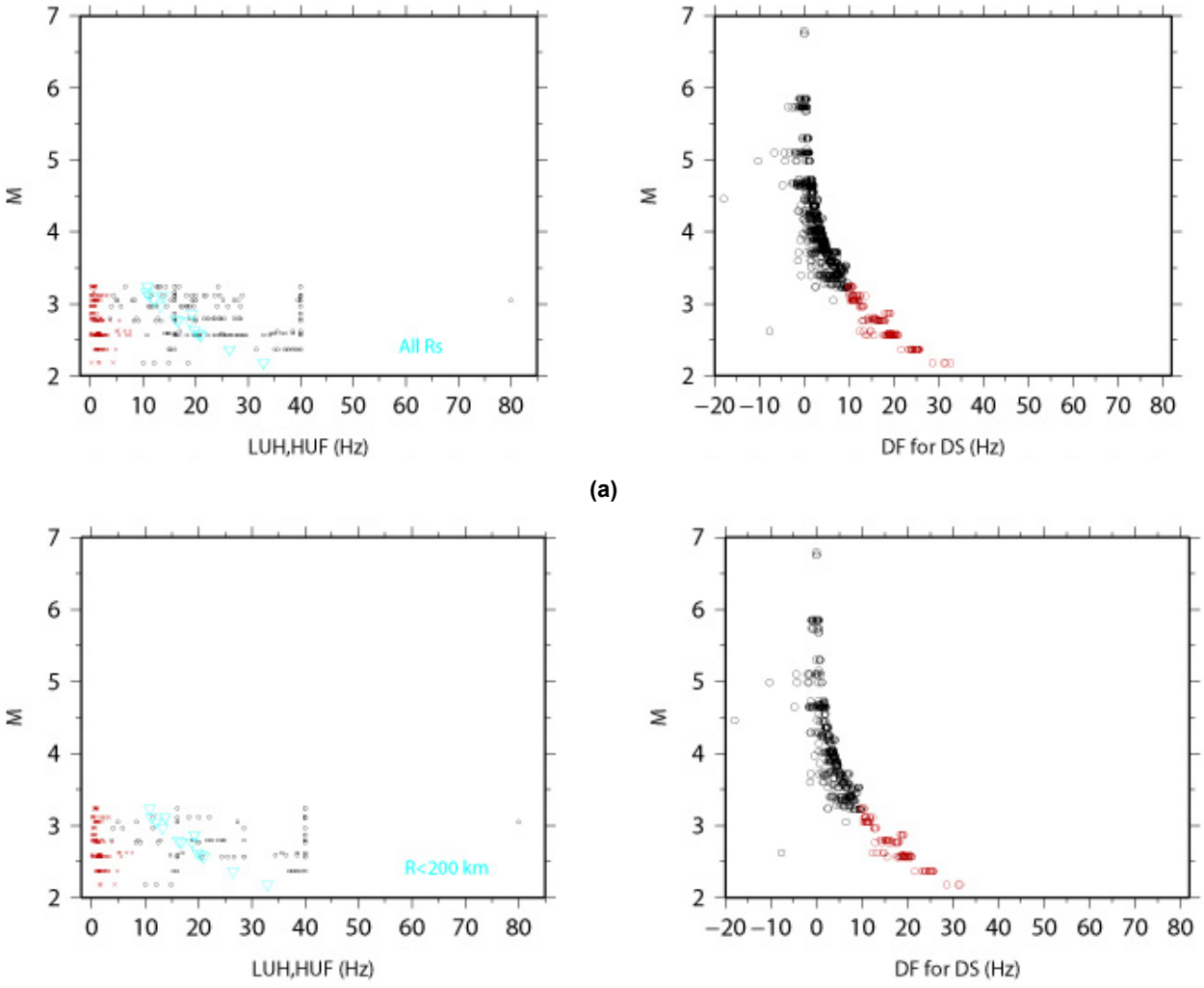

Figure 3.7 **(a) LUF, HUF, and 1.5 • f_{cmin} values for record with available DF_$_{AS}$ ≥ 10 Hz; and (b) corresponding DF_$_{AS}$ values (right): for all distances (top), and for distances less than 200 km (bottom).**

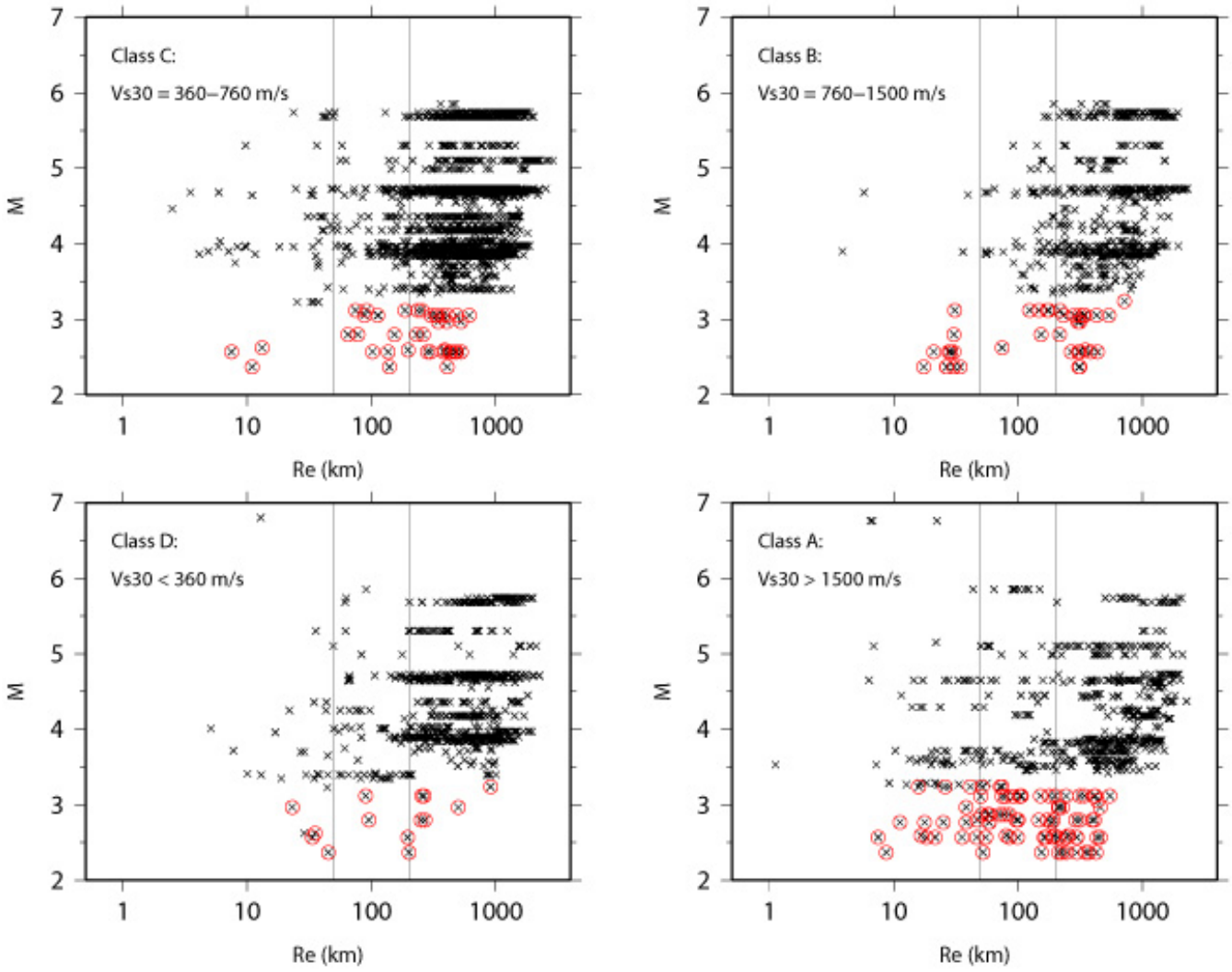

Figure 3.8 **Magnitude-distance distribution per NEHRP site class, for the recordings that have $DF\_{AS} \geq 10$ Hz. The recordings for which there is overlap between the DS and AS approach are marked in red.**

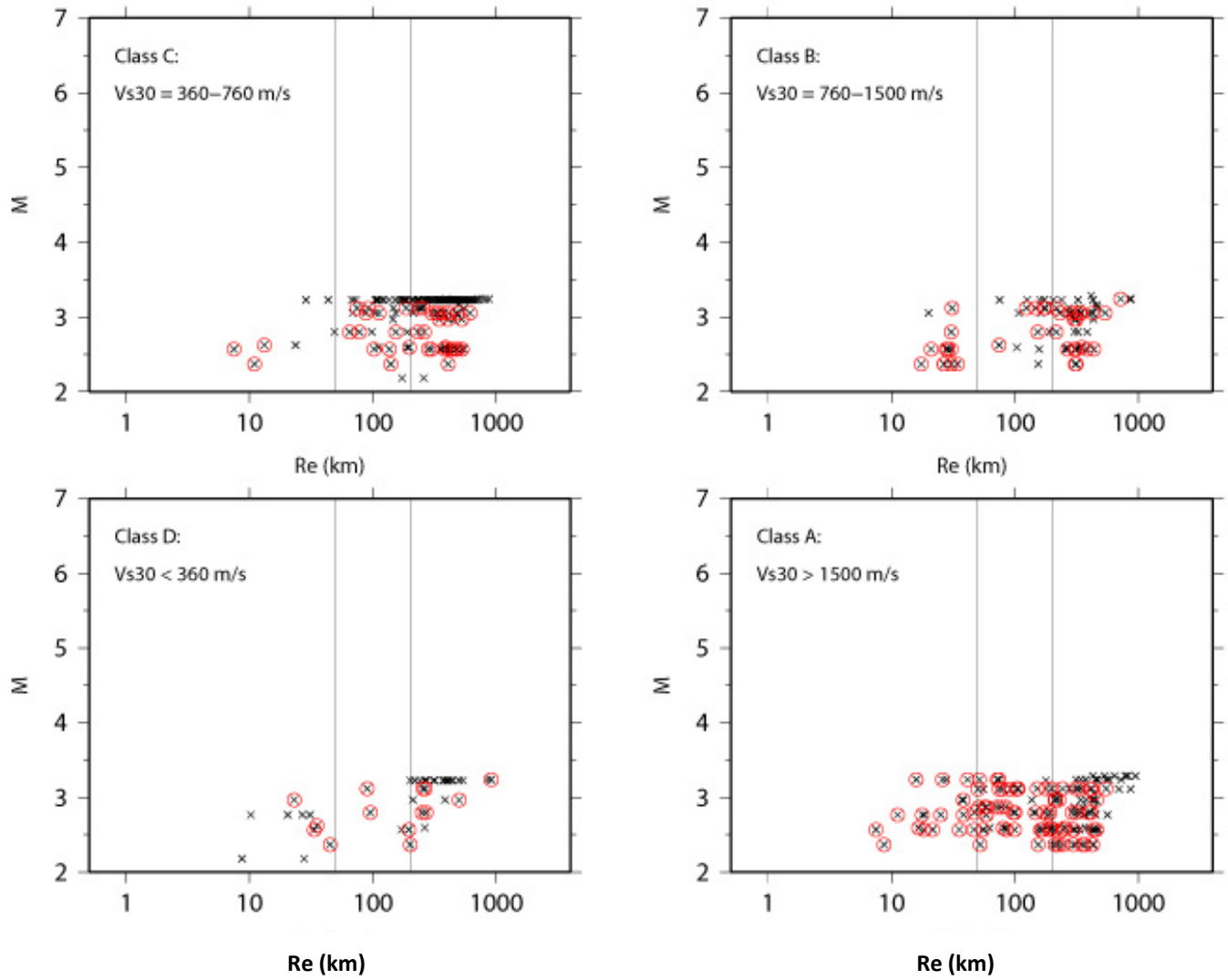

Figure 3.9 **Magnitude-distance distribution per NEHRP site class, for the recordings that have $DF\_{DS} \geq 10$ Hz. The recordings for which there is overlap between the DS and AS approach are marked in red.**

Table 3.2 **AS approach for $\Delta\sigma_{min}$ ($DF\_{AS} \geq 10$ Hz): The decrease in the number of recordings, events and stations for all NEHRP site classifications as various distance constraints are used.**

	All	$R \leq 200$ km	$R \leq 50$ km
Recordings	5082	635	190
Events	81	72	54
Stations	1037	247	82

Table 3.3 **DS approach for $\Delta\sigma_{max}$ ($DF\_{DS} \geq 10$ Hz): The decrease in the number of recordings, events and stations for all NEHRP site classifications as various distance constraints are used.**

	All	$R \leq 200$ km	$R \leq 50$ km
Recordings	458	160	50
Events	20	17	15
Stations	261	92	32

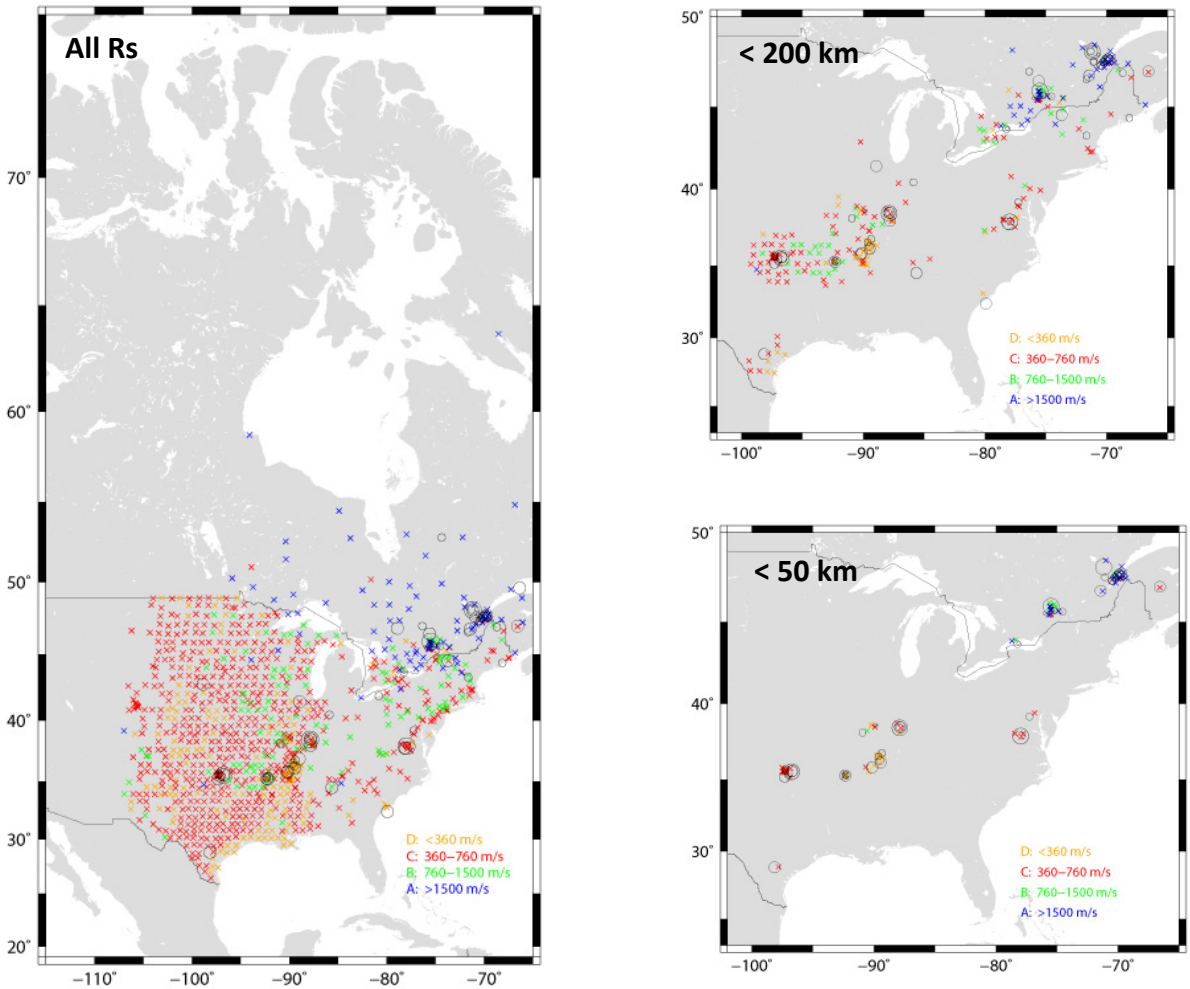

Figure 3.10 **Epicenters and recording stations for recordings with $DF\_{AS} \geq 10$ Hz: for all distances, for distances less than 200 km, and for distances less than 50 km.**

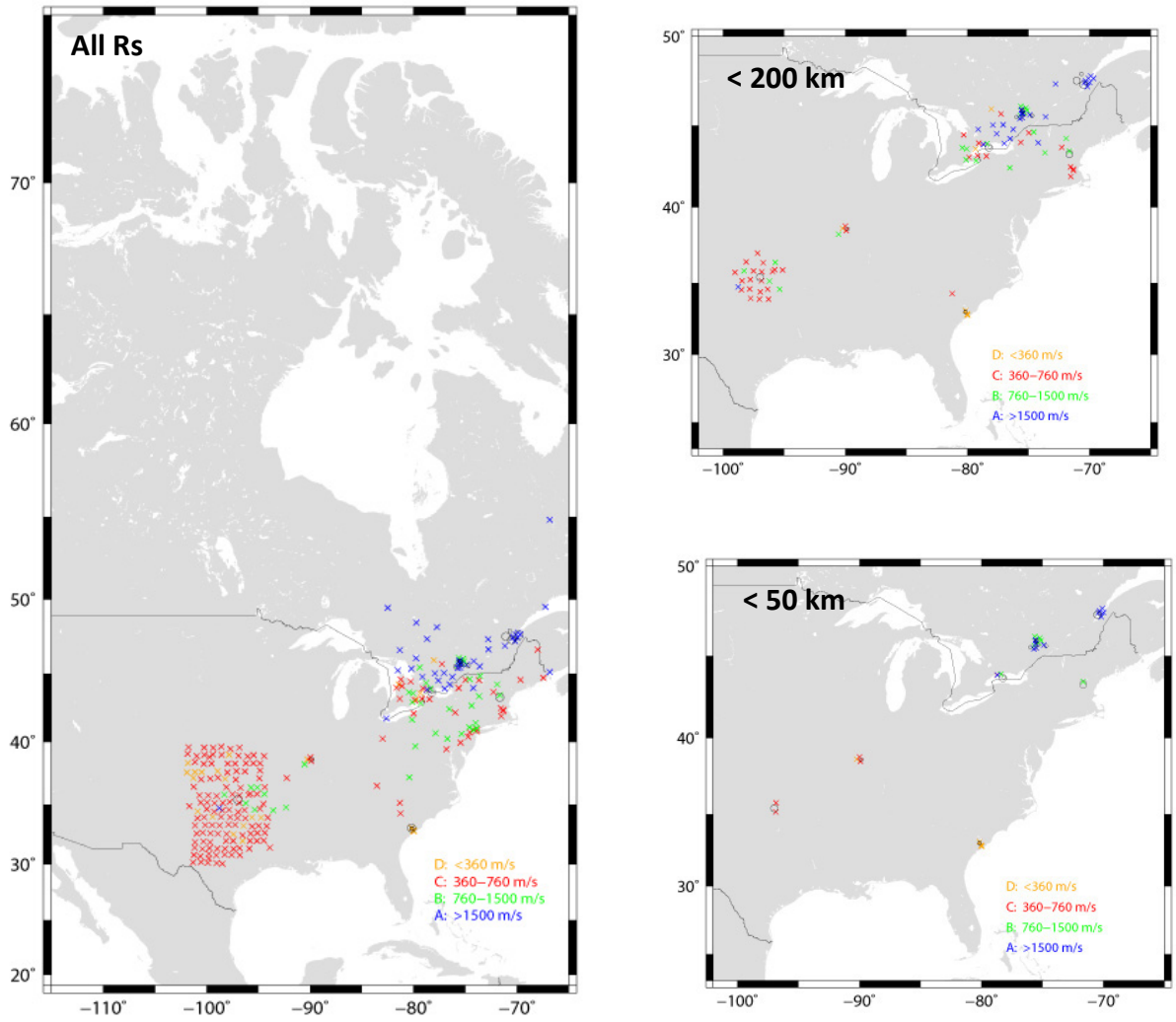

Figure 3.11 **Epicenters and recording stations for recordings with $DF\_{DS} \geq 10$ Hz: for all distances, for distances less than 200 km, and for distances less than 50 km.**

3.2.2 Preliminary Results

The previous section presented a distance screening example from a large dataset, in this case, NGA-East, to retrieve as many usable recordings as possible for the AS and (if applicable) the DS approach. For the example application, the main considerations are:

- distance: a less restrictive value of $R_e \leq 100$ km (rather than 50 km) was chosen, this distance range (50–100 km) may include some contribution form the path attenuation, but it is assumed to be dominated by the site attenuation
- site classification: sites with $V_{s30} \geq 1000$ m/sec are selected, to include some softer rock sites together with the hard-rock sites

- available bandwidth: the bandwidth criterion is reduced from 10 to 8 Hz, that is, $DF\_{AS} \geq 8$ Hz and $DF\_{DS} \geq 8$ Hz.

Based on these criteria, the available data for approaches AS and DS are shown in the last two columns of Table 3.4. There are 138 recordings that can be used in the AS method and 48 for the DS. Forty of these recordings can be used in either method. The magnitude and distance distribution is shown in Figure 3.12. The epicenters and station locations are shown in Figure 3.13.

Table 3.4 **Available data for DS and AS approach, at distances less than 100 km and for soft-rock and hard-rock sites ($V_{s30} \geq 1000$ m/sec). Comparison with the total number of recordings, events and stations in NGA-East.**

	Total	AS	DS
Recordings	9384	**138**	**48**
Events	84	34	13
Stations	1272	45	25

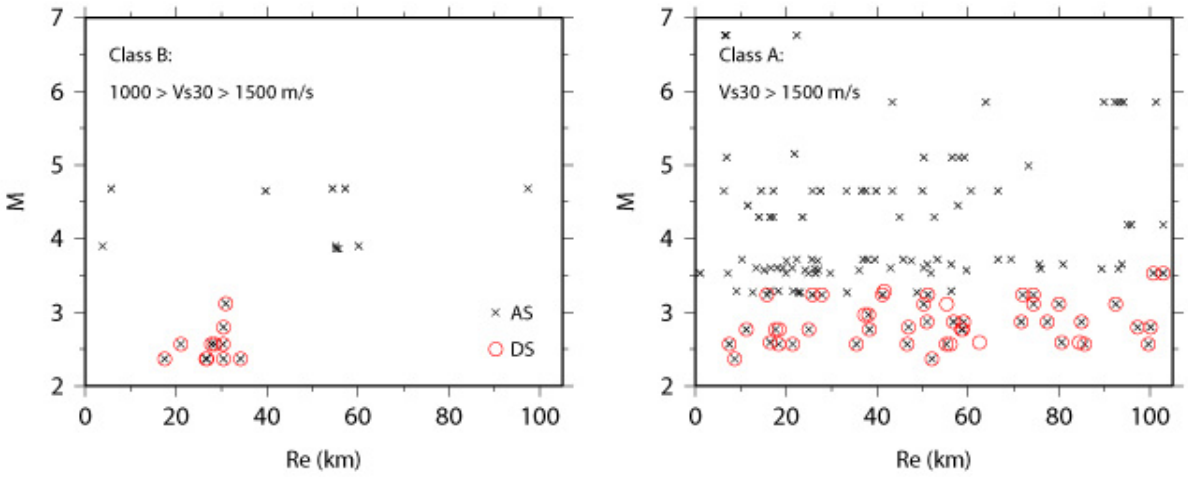

(a) (b)

Figure 3.12 **Magnitude and distance for the recordings that have $DF\_{AS} \geq 8$ Hz (black) and $DF\_{DS} \geq 8$ Hz (red), for distances less than 100 km, and for sites with (a) $V_{s30} \geq 1000$ m/sec and (b) $V_{s30} \geq 1500$ m/sec.**

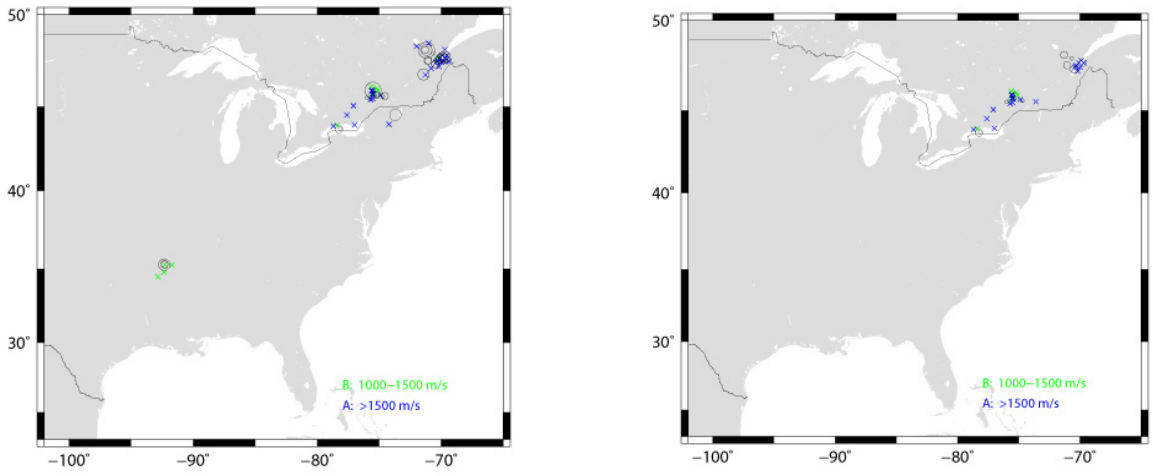

Figure 3.13 Epicenters and station locations for the recordings that have $DF\_{AS} \geq 8$ Hz (left) and $DF\_{DS} \geq 8$ Hz (right), for distances less than 100 km, and for sites with $V_{s30} \geq 1000$ m/sec (green) and $V_{s30} \geq 1500$ m/sec (blue).

A simplified procedure with respect to the detailed methodology of Section 2.2.2 is followed:

- No correction is made on the FAS for amplification from shallow site resonances. In general, the detailed site-specific profiles are unavailable, so 1D transfer functions cannot be computed; however, the FAS is corrected for crustal amplification. More details are given below.
- A correction for the path attenuation, $Q(f)$, is not included because the choice of distance ($\leq$ 100 km) may make this effect negligible for most recordings. For the same reason, the sites are also not regionalized.
- The FAS are not smoothed, nor is a moving window applied to the FAS.
- The vector sum of the FAS defined in Equation (2.3) is used to minimize the effect of component orientation.
- The error on the slope of the FAS [λ in Equation (2.1)] is computed as an indication of the uncertainty of the κ_r estimate.
- Recordings are not binned by PGA because the amplitudes are generally low and nonlinear effects are not a concern for these loading levels at these stiff to very hard sites.
- Recordings are not binned by either V_{s30} or NEHRP class A/B; however, the κ estimates versus V_{s30} are examined.

- κ_r on individual FAS is measured. The risk of including some bias from unknown high-frequency resonances is noted. However, because the FAS per station are stacked on a logarithmic scale to measure an average κ_r; the stacking provides some smoothing through possible resonance peaks.

To correct the FAS for crustal amplification, generic profile and amplification function computed by PEER [2015] and shown in Figure 3.14 are used, with mean V_{s30} of 2032 m/sec. For the results of the band-limited methods AS and DS discussed in this section to be consistent with the results for the broadband methods BB and RESP), we adopted the same amplification function throughout. Note that between 5–15 Hz there is some increase in amplification for this generic site class; this observation will be further discussed when the results for the AS and DS approaches are presented below.

After visual inspection of the recordings chosen as suitable for applying the AS approach, there were several recordings that have acceleration FAS for which no spectral decay (κ) can be observed at high frequencies; these FAS either have a significant up-going trend with increasing frequency or exhibit significant resonance peaks, possibly due to near-surface amplification (e.g., Figure 3.15a). For some recordings, little or no decrease with frequency can be seen because the FAS at high frequencies show no trend, i.e., it appears horizontal; see Figure 3.15b. Finally, several recordings exhibit a clear down-going trend with increasing frequency, as expected for κ; see Figure 3.15c. A flag is assigned to each record according to which FAS trend is observed at high frequencies in the usable bandwidth: -1 for upward trend or strong near-surface amplification effects, 0 for no trend (flat), and 1 for downward trend. These flag definitions are also shown in Table 3.5.

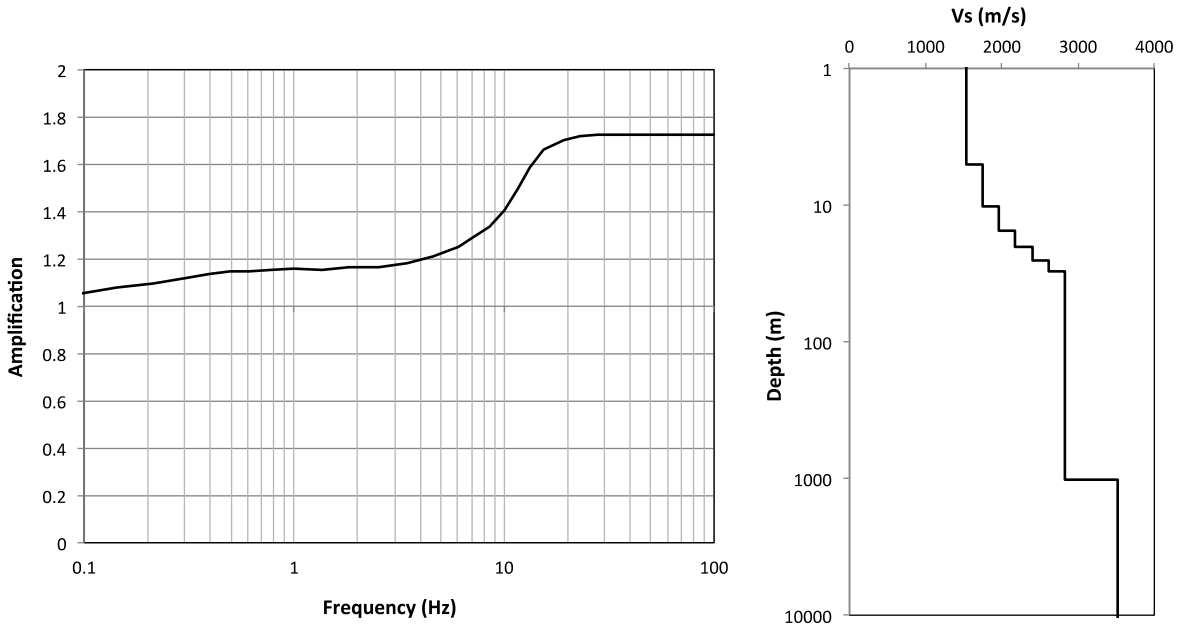

Figure 3.14 Generic crustal profile and corresponding amplification function for class A1 with V_{s30} = 2032 m/sec [PEER 2015].

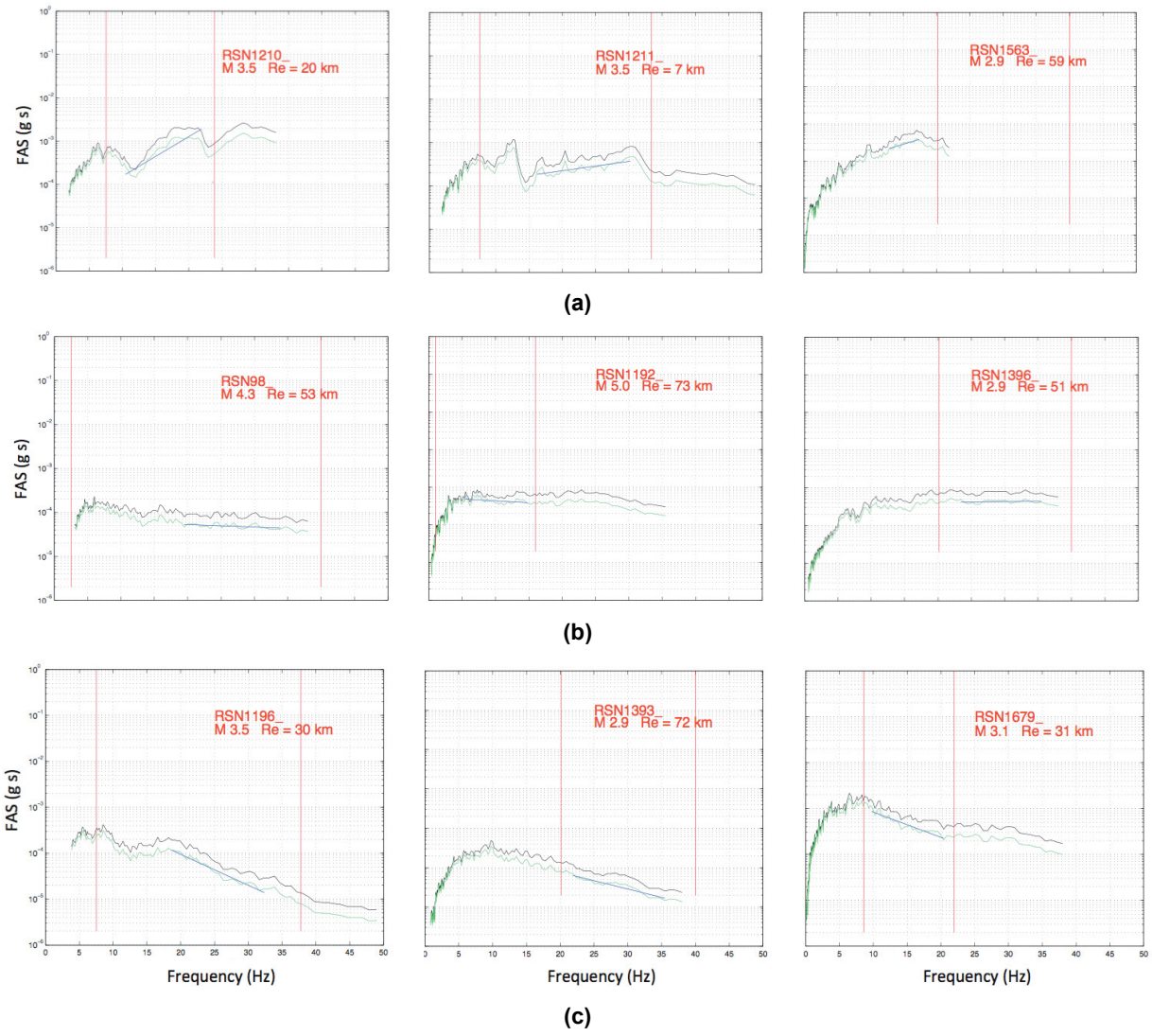

Figure 3.15 **(a) Example FAS for acceleration recordings with significant up-going trend or significant near-surface site amplification (flag -1); (b) recordings without significant up-going trend (flag 0); and (c) recordings with clear down-going trend (flag 1).**

Figure 3.16a shows the measured κ_{r_AS} values for: all recordings (flags 0,-1,1); Figure 3.16b shows recordings without significant up-going trend (flags 0,1), and Figure 3.16c shows recordings with clear down-going trend (flag 1). The mean values for these groups are: 8, 15, and 25 msec, respectively (Table 3.5). The same figure also shows the linear regression with distance. The extrapolated κ_0 value at zero epicentral distance from the fits is 3, 8, and 18 msec, respectively. The three regression lines have similar slopes with distance, from which a regional attenuation of about 1900–2500 (assuming crustal velocity of 3.5 km/sec) can be inferred. However, the correlation coefficients are very low (< 10%), and the confidence intervals at zero distance indicate a large scatter; therefore, the increase with distance is not considered significant. Moreover, the blue curves indicating the confidence intervals for data out to 80–90 km (i.e., excluding only the most distant data) show no distance dependence.

As observed for acceleration FAS, the displacement FAS also show different trends between recordings. Figure 3.17a shows example displacement FAS that have a significant up-going trend or significant near-surface amplification (flag -1); Figure 3.17b shows recordings without significant up-going trend (flat; flag 0); and Figure 3.17c shows recordings with clear down-going trend (flag 1).

Figure 3.18 shows the measured κ_{r_DS} values for: all recordings (top), recordings without significant up-going trend (middle), and recordings with clear down-going trend (bottom). The mean values for these groups are: 27, 35, and 42 msec; combining AS and DS results, the mean values are: 13, 20, and 30 msec. These mean values, along with the number of recordings per flag, are shown in Table 3.5. The extrapolated κ_0 value at zero epicentral distance from the fit is 16, 30, and 36 m/sec respectively, significantly larger than the κ_{r_AS} method; see Table 3.5. As found in the AS case, the correlation coefficients of the regressed lines are again very low (< 10%) and the confidence interval of the mean is very wide; therefore, the increase with distance is not considered significant.

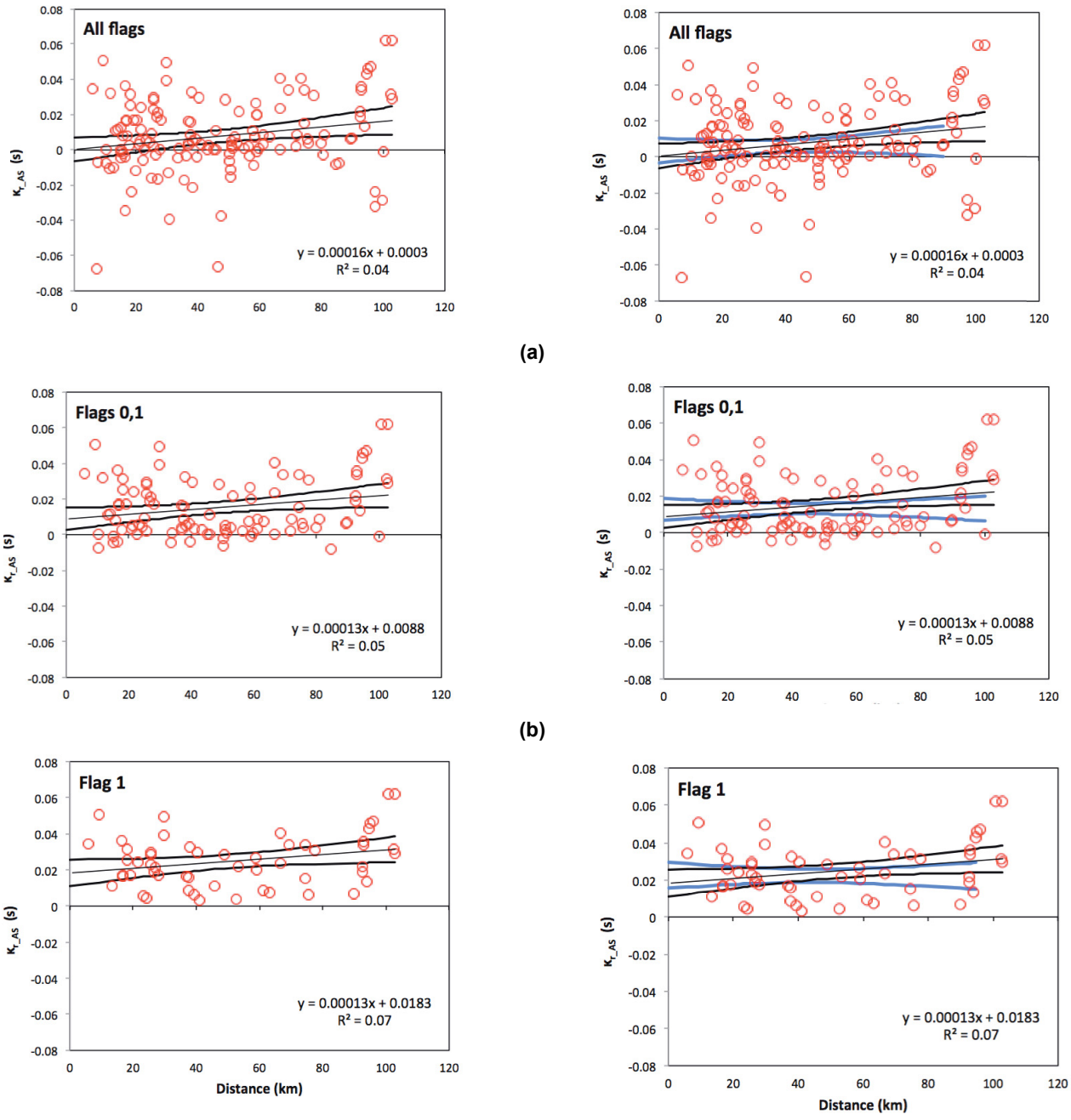

Figure 3.16 (a) Measured κ_{r_AS} values for: all recordings; (b) recordings without significant up-going trend, and (c) recordings with clear down-going trend (bottom). Lines show the mean and its 95% confidence intervals.

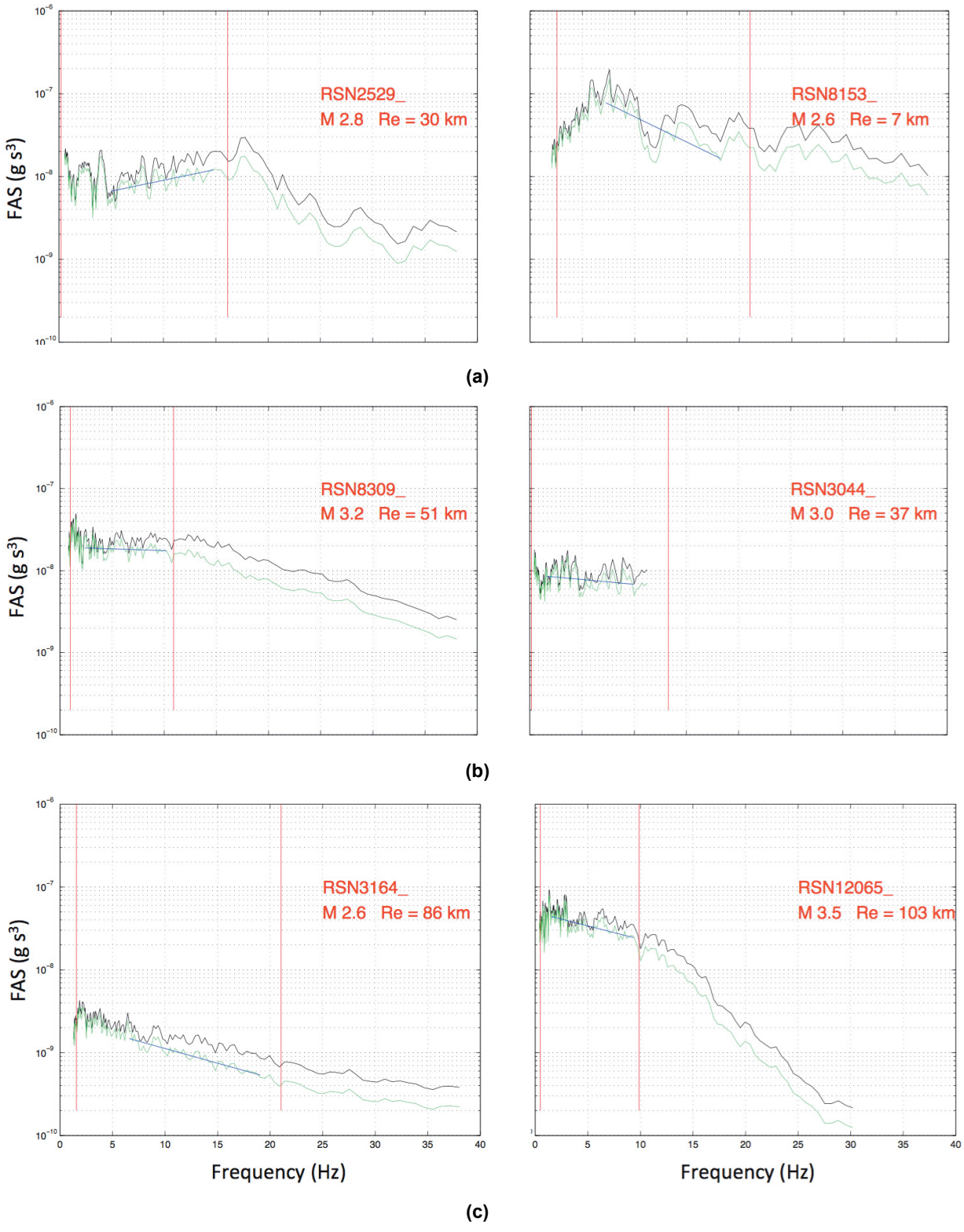

Figure 3.17 **(a) Example FAS for displacement recordings with significant up-going trend or significant interference by amplification (flag -1); (b) recordings without significant up-going trend (flag 0); and (c) recordings with clear down-going trend (flag 1).**

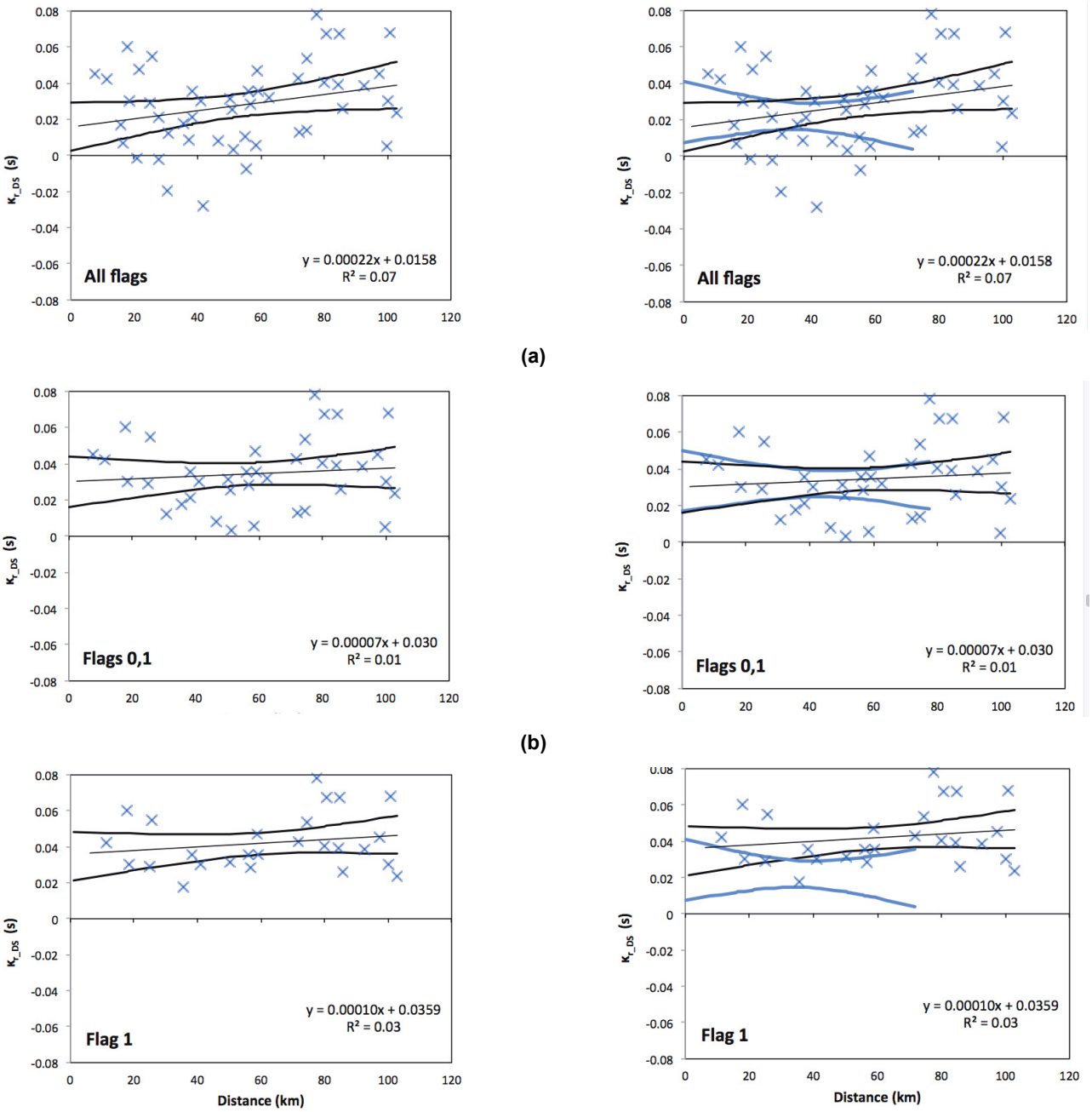

Figure 3.18 **(a) Measured κ_{r_DS} values for: all recordings; (b) recordings without significant up-going trend; and (c) recordings with clear down-going trend (bottom). Lines show the mean and its 95% confidence intervals.**

Table 3.5 **Mean κ_r values over the first 100 km, and extrapolated κ_0 values at zero distance for three subsets: all recordings, recordings without significant up-going trend, and recordings with clear down-going trend.**

Flags	Subset studied	Number of recordings AS/DS	Mean κ_r value over first 100 km (msec)				Extrapolated κ_0 value to $R = 0$ (msec)	
			AS	DS	AS and DS	$\kappa_{r\_DS}/\kappa_{r\_AS}$	AS	DS
Flags -1,0,1	All recordings	138/48	8	27	13	3.4	3	16
Flags 0,1	Exclude up-trending FAS	97/37	15	35	20	2.3	8	30
Flags 1	Only down-trending FAS	55/26	25	42	30	1.7	18	36

In Figure 3.19, the measured κ_{r_AS} and κ_{r_DS} values are plotted versus magnitude, and those with flag 1 are highlighted. In Figure 3.20, the measured κ_{r_AS} and κ_{r_DS} values are combined and plotted against magnitude for all recordings. Figure 3.20a shows results for all recordings, and Figure 3.20b results for recordings with flag 1. For the DS approach there is no significant magnitude dependence, but for the AS approach there is a trend for κ_{r_AS} to decrease at smaller magnitudes (below **M**3). This trend is probably due to the effect of the source corner moving into the frequency measurement band. A clear difference between the two methods is observed, as the DS measurements are generally larger than AS measurements. Table 3.5 shows that, for flag 1, the mean values for the two methods are 25 msec and 42 msec for AS and DS, respectively. This is a factor of 1.7 between the two methods. These factors are consistent with Biasi and Smith [2001] and Kilb et al. [2012] that reported values of 2, while Kishida et al. [2014] found a factor of about 3 using a poorer quality dataset with more limited bandwidth.

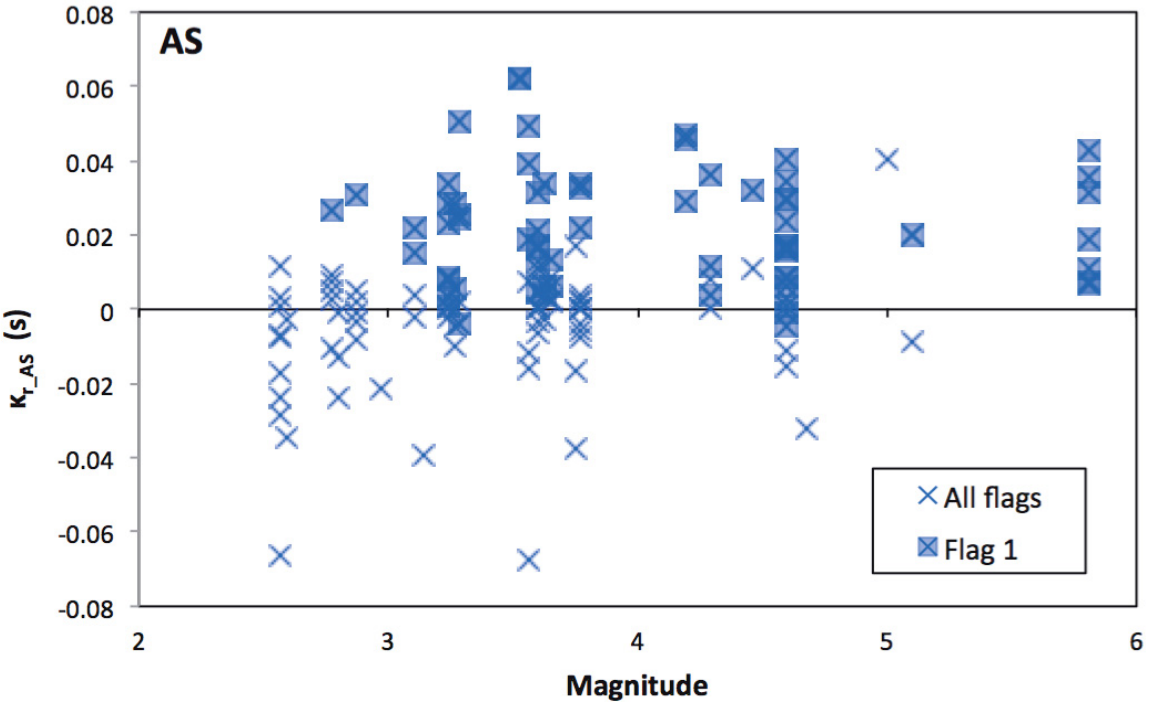

(a)

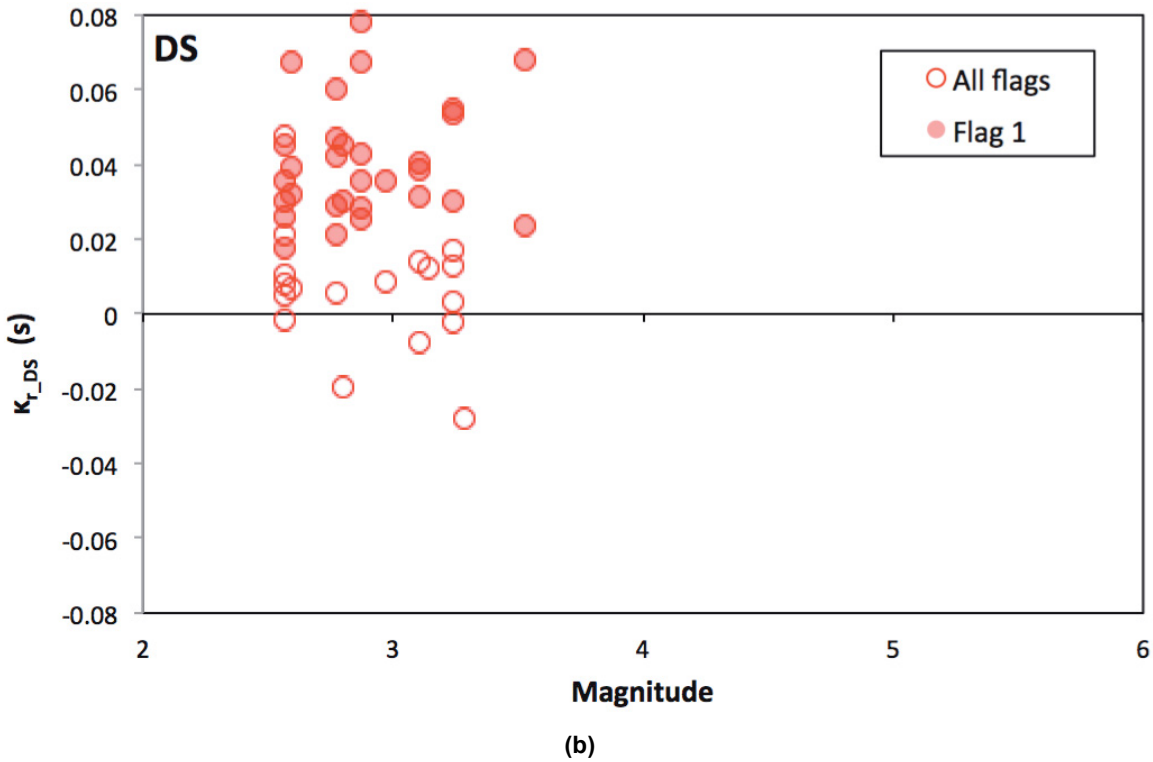

(b)

Figure 3.19 **(a) Measured κ_{r_AS} and (b) κ_{r_DS} values versus magnitude (filled symbols represent data with down-trending FAS, i.e., flag 1).**

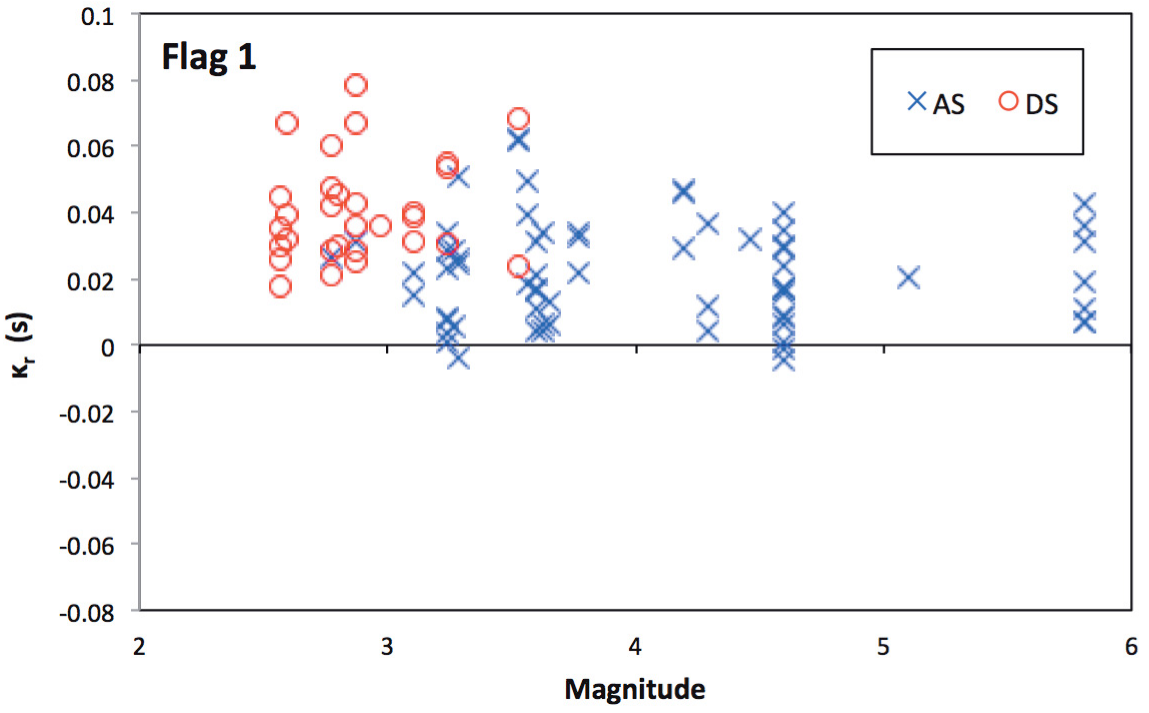

(a)

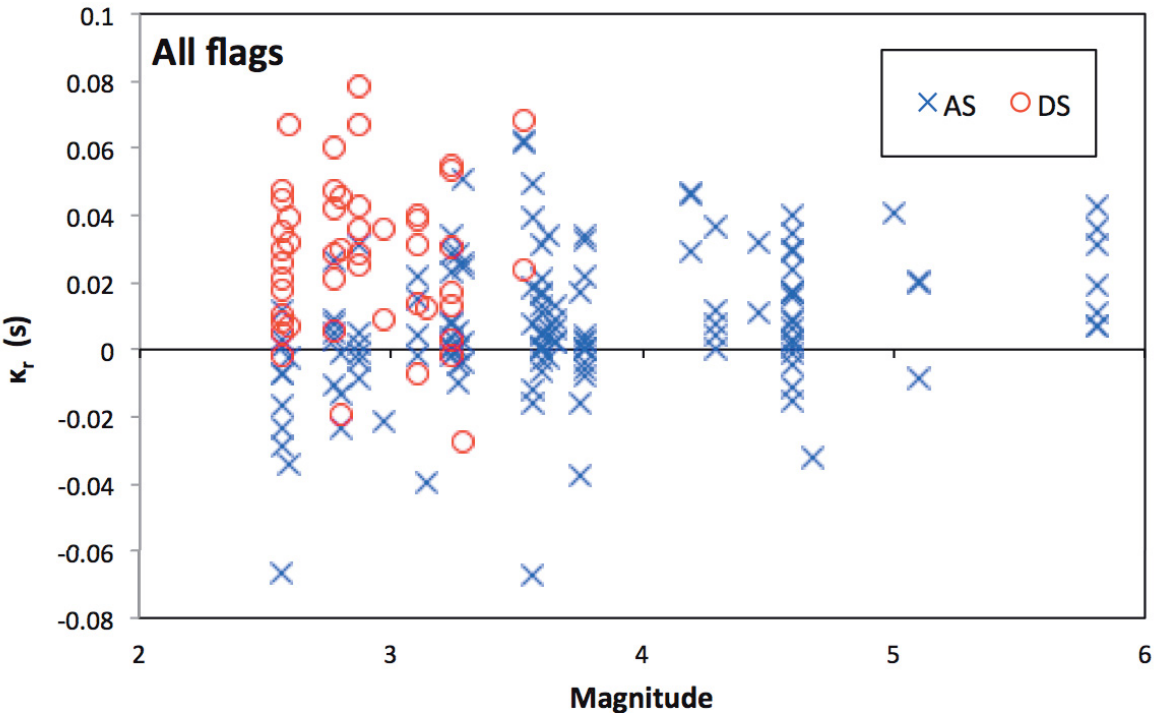

(b)

Figure 3.20 **Measured κ_{r_AS} and κ_{r_DS} values versus magnitude: (a) only down-trending and (b) all recordings.**

Figure 3.21 indicates that the difference between the two methods may not be as significant when one considers the uncertainty about the individual measured values of κ_r. This uncertainty was estimated as the standard deviation that corresponds to the error on the slope λ [Equation (2.1)] when fitting each individual FAS. The uncertainty decreases significantly as magnitude increases, and the uncertainty for the DS measurements is generally higher than for AS.

Overall, no correlation of κ_r with V_{s30} is observed. Figure 3.22 shows that nearly all sites have a designated V_{s30} of 2000 m/sec. Some of these sites are in Canada and have been assigned this value by Beresnev and Atkinson [1997], and this was assumed to be the case for all hard-rock CENA sites by Goulet et al. [2014]. Unfortunately, this is due to the lack of site characterization at CENA hard-rock sites in the NGA-East dataset, which is difficult and expensive to carry out. Therefore, the data cannot determine if part of the large dispersion of κ_{r_AS} and κ_{r_DS} values observed might be explained by differences in site hardness.

As stated earlier, for the results in this section (band-limited methods AS and DS) to be consistent with the results in the following sections (broadband methods BB and RESP), the same amplification function corresponding to NEHRP class A rock (2030 m/sec) derived by PEER [2015, see Figure 3.14] is used to correct the individual FAS for crustal amplification. Because this transfer function includes some amplification between 5–15 Hz, the correction for crustal amplification and its effect on the measured κ values is examined.

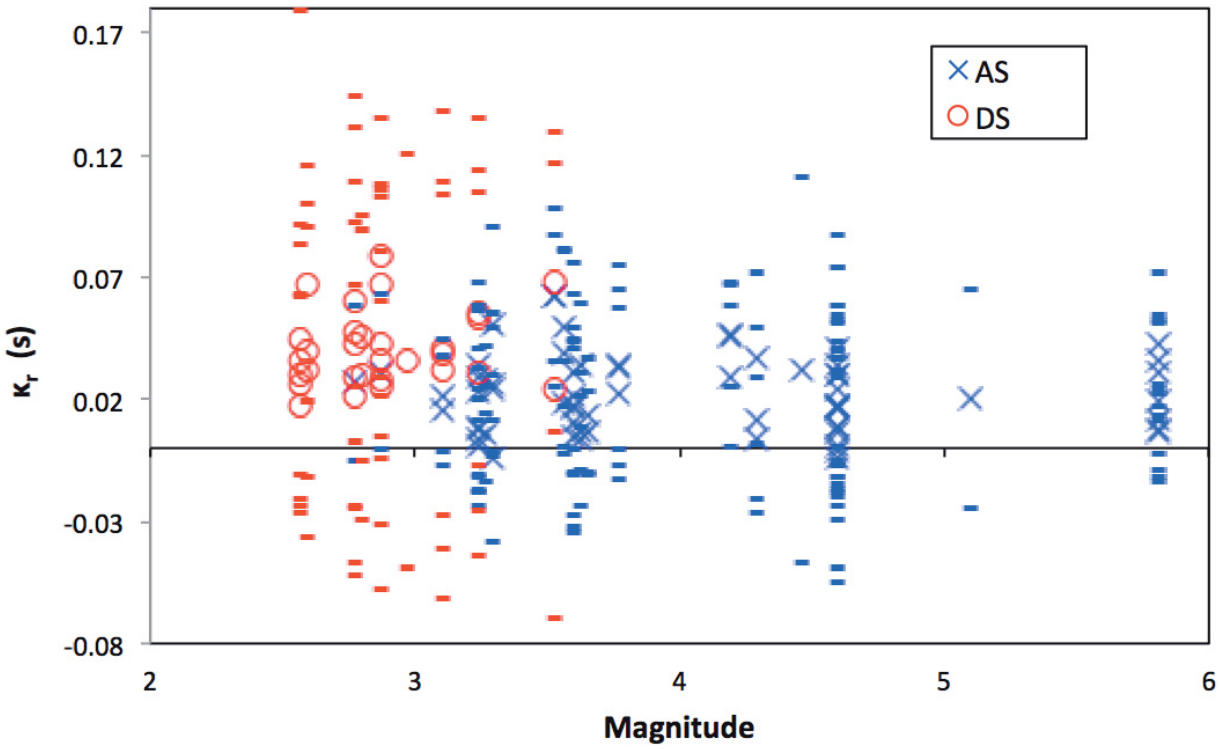

Figure 3.21 **Measured κ_{r_AS} and κ_{r_DS} values versus magnitude for flag 1 recordings. Error bars show the error on the slope in the regression on the FAS.**

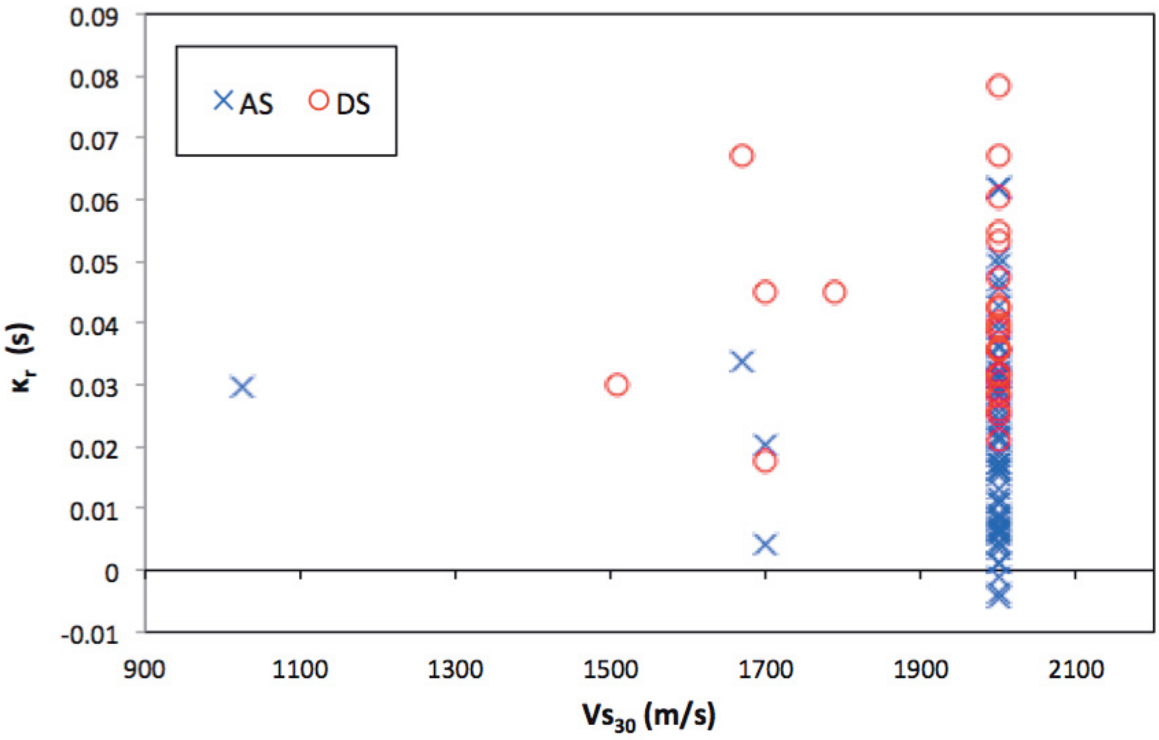

Figure 3.22 Measured κ_{r_AS} and κ_{r_DS} values versus V_{s30}.

In Figure 3.23, the comparison between measured κ_{r_AS} for corrected for crustal amplification and uncorrected (crustal amplification of unity) FAS (for all recordings, and for the subset with down-going trends) is shown. Note that although there is an increase in amplification between 5–15 Hz, this does not affect significantly the measurement of κ_{r_AS}. For most recordings, the difference in κ_{r_AS} for corrected and uncorrected FAS is less than about 5%. One counter-example is the case of southern Arizona project [Kishida et al. 2014], where the usable bandwidth extended only up to 16 Hz, and the crustal amplification at these softer sites was significant in this frequency range, leading to differences in κ_{r_AS} of up to 35%. In contrast, Figure 3.23 shows that κ_{r_DS} is affected by the correction for crustal amplification, which leads to a systematic increase in κ_{r_DS} of about 9 m/sec when corrected for crustal amplification. The reason for the different effect of the generic crustal amplification correction on the AS and DS κ_r values is explained in Figure 3.24: the AS approach mostly uses frequencies unaffected by the correction, i.e., frequencies above 15 Hz, while the bandwidth used by the DS approach lies largely within the 5–15 Hz range.

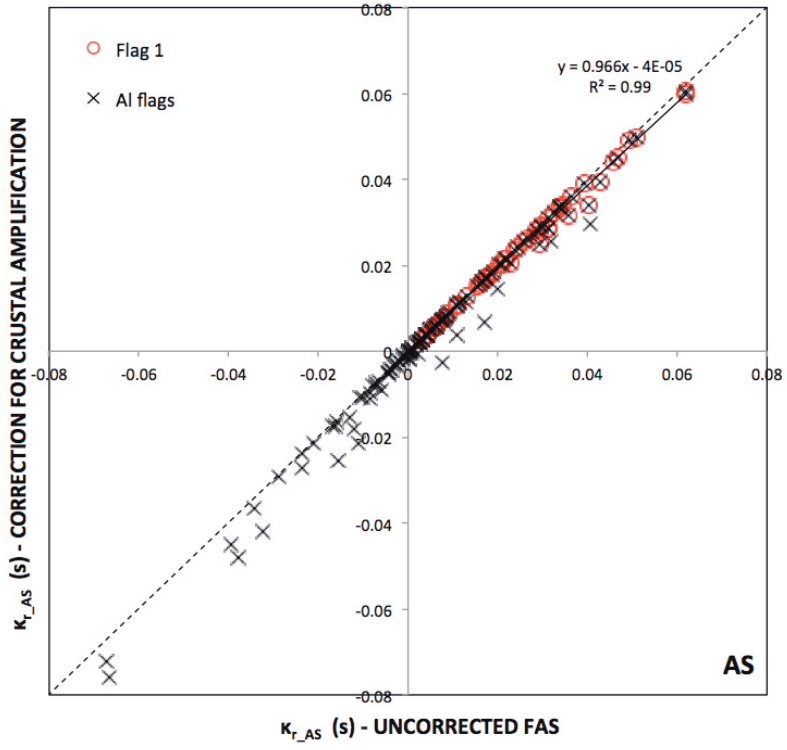

(a)

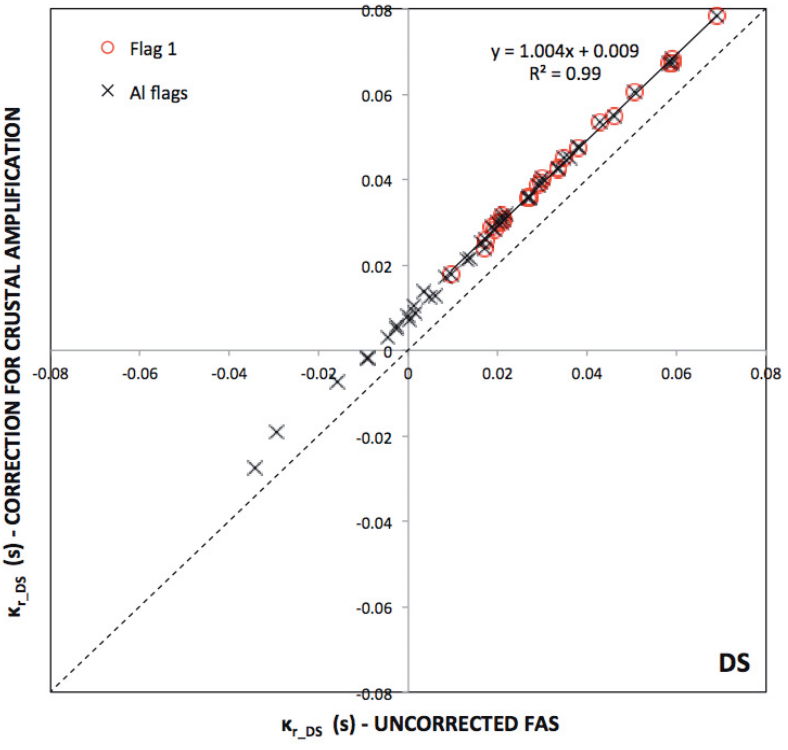

(b)

Figure 3.23 **Comparison of measured (a) κ_{r_AS} and (b) κ_{r_DS} for site-corrected and uncorrected FAS.**

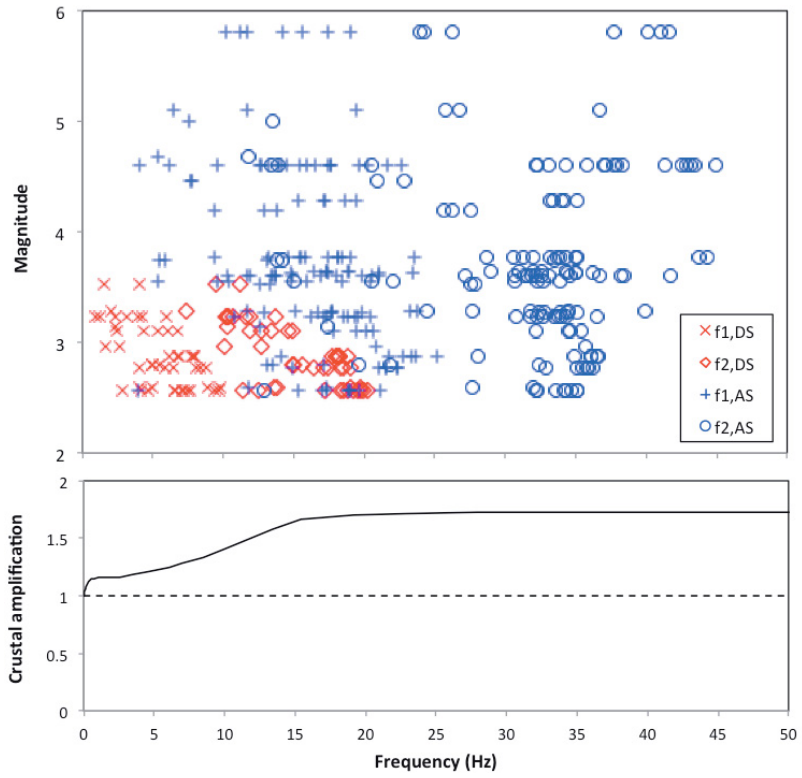

Figure 3.24 **Frequency bands (f_1, blue cross, f_2, red circle) used to measure κ_{r_AS} (thin symbols) and κ_{r_DS} (thick symbols), plotted against magnitude. Also shown, the crustal amplification function, which mainly affects the band for $\kappa_{r\ DS}$.**

Previously, κ_r was measured on vector-averaged FAS, for both acceleration and displacement, at the risk of including some bias from the record-specific 'fine' structure of the FAS, or from site-specific resonance patterns. In order to minimize these effects, the FAS from the recordings are stacked (on a logarithmic scale) in two ways: first, the FAS of all recordings are stacked together (separately for each approach, AS and DS), and second, the FAS of all available recordings per station are stacked provided the station recorded at least three events. The average κ_r on the mean FAS derived from the stacking was then estimated. This process yielded an overall value of κ_{0_AS} and κ_{0_DS} for the entire region under study (CENA), and overall values of κ_{0_AS} and κ_{0_DS} for well-recorded stations. This stacking procedure should help smooth through the differences between individual recordings and between individual stations. Because there is no significant dependence of κ_{r_AS} and κ_{r_DS} values with either parameter in this dataset, the use of stacking means that differences in magnitude and distance can be ignored.

To stack the FAS, a common frequency range is selected, which allows the use of as many recordings as possible over as wide a frequency range as possible. After examining the data, the chosen frequency range (f_1, f_2) for the individual FAS per approach (Figure 3.24), is 15–30 Hz for the AS approach and 5–15 Hz for the DS approach. This selection eliminates fewer than ten recordings overall.

Figure 3.25a and 3.25b show the mean FAS derived from stacking all FAS for the AS and the DS approaches, respectively. All recordings (i.e., all flags) are used. The individual FAS are plotted normalized as to their mean value in the 15–30 Hz interval, to accentuate the slope (κ). The mean κ values measured from the stacked FAS are 6.6 and 29.4 msec for the AS and DS approaches, respectively. These are almost the same values found from averaging the individual κ_r measurements for all flags (Table 3.5). We performed a sensitivity check, modifying the chosen frequency range (f_1–f_2) several times for each approach, e.g., from 15–30 Hz to 13–28 Hz. The results of the frequency range variation are shown in Table 3.6.

Table 3.6 **Mean κ measurements from stacked FAS for the AS and DS approach, for various f_1–f_2 combinations. The chosen bandwidth is shown in bold. Underlined values represent windows outside the allowed bandwidth, which are too close to the source corner frequency.**

Frequency range (Hz)	21–30	19–30	17–30	**15–30**	15–28	15–26	15–24	13–24	13–22	11–20	9–20
κ_{r_AS} (msec)	9	8	7.5	**6.6**	5.8	5.1	4.7	4.3	4.1	4	2.7

Frequency range (Hz)	5–12	5–13	5–14	**5–15**	6–15	7–15	8–15
κ_{r_DS} (msec)	24.9	26	27.4	**29.4**	31.2	33.1	35.1

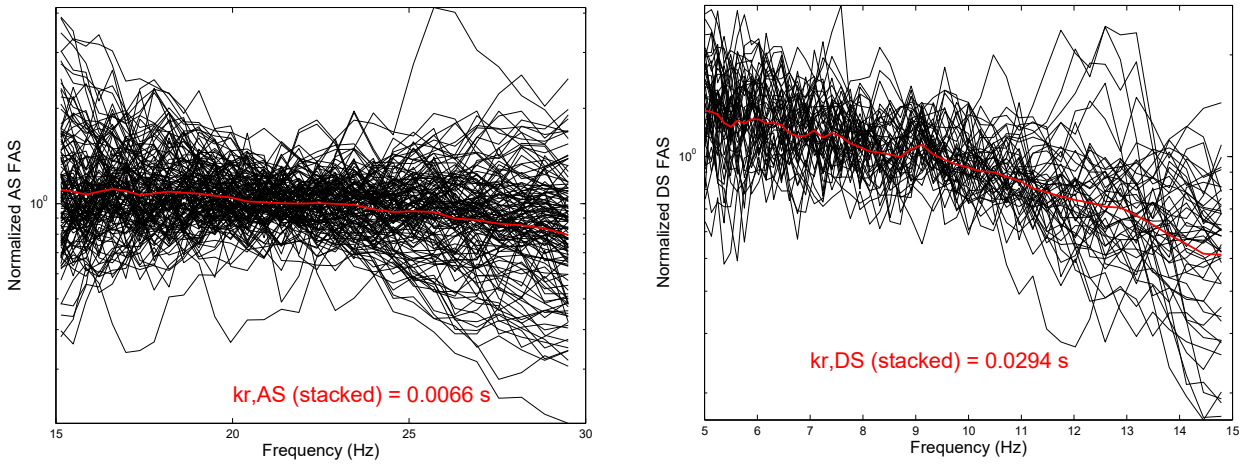

(a) **(b)**

Figure 3.25 **Mean FAS derived from stacking all recordings chosen for (a) the AS and (b) DS approach, and estimation of mean κ for the entire dataset.**

For the AS method, increasing the minimum frequency limit f_1 (from 15 to 17, 19, or 21 Hz, with f_2 = 30 Hz) increases κ_{r_AS} by 36% (from 6.6 to 9 msec). In contrast, decreasing the upper frequency limit f_2 (from 30 to 28, 26, or 24 Hz, with f_1 = 15 Hz) decreases κ_{r_AS}. The mean κ_{r_AS} from these variations in bandwidth is in good agreement with the κ_{r_AS} from the selected bandwidth. However, decreasing the frequency range ever further (e.g., 9–20 Hz in Table 3.6), causes the results to decrease significantly because the approach is no longer applied correctly as the source corner frequency is approached.

Similarly, for the DS method, decreasing the maximum frequency limit f_2 (from 15 to 14, 13, or 12 Hz) decreases the estimated κ_{r_DS}. Again, increasing the minimum frequency limit f_1 (from 5 to 6, 7, or 8 Hz) increases the estimate of κ_{r_DS}. In this case, the measurements become less robust as the DF decreases.

Finally, the FAS for individual sites that have recorded more than three events are stacked. There are nine sites for the AS method and seven for the DS that meet this requirement. The same chosen frequency bands (f_1, f_2) are used as before. Initially, recordings with any flag were used because of the paucity of data at each station. Figure 3.26 shows the individual and mean stacked FAS per station for the AS approach; Figure 3.27 shows the same for the DS. Tables 3.7 and 3.8 show the number of recordings per site for each method, with the flags attributed to the individual FAS and the computed mean site κ. The mean κ_{r_AS} is computed for:

- All sites and recordings regardless of flag (8 msec)
- Only sites that have flags of 0 and 1 –indicated by an asterisk- (19 msec)
- For all sites rejecting flags of -1 (12 msec).

The mean κ_{r_DS} is 35 m/sec (there are no flags of -1). These values are again consistent with those in Table 3.5.

In this section, consistent κ values were computed for each approach (AS or DS) for the ensemble of the selected dataset, measuring κ on either the individual FAS or on FAS stacked in two different ways. However, the scatter within stations can be large (Figures 3.26 and 3.27), and the scatter between sites is larger; see Figure 3.28 and Tables 3.7 and 3.8). The within-station scatter may be related to differences in distance, Q, complexity along the path, or particular source characteristics, such as higher or lower stress drop. The station-to-station differences may be due to site-related factors. For instance, for some sites there is a systematic trend in the FAS, across all events, e.g., station 15 in Figure 3.26, where all the FAS have an up-going trend with increasing frequency (negative κ, or κ effects at above the HUF). This may be due to shallow site resonance, especially broadband amplification effects, which may interfere with the measurement of κ. At a recent study at a site in CENA, with shallow soil and weathered rock over hard rock, the site resonance was observed near 60 Hz [R. B. Darragh, *personal communication*, 2015]. The FAS at this site increased, similar to the observation for several sites in this study, as frequency increased to the peak near the resonance frequency. Fortunately, the HUF at this site was 80 Hz, much larger than most of the HUF values in this dataset. Resolving this issue lies beyond the scope of this report; however, these results indicate that such effects should be investigated further and taken into account in measuring κ. Instrumentation with higher sampling rates (at least 200 samples per second) is also suggested, especially at hard-rock sites. In addition, the coupling of site amplification with site attenuation becomes a key

limitation in measuring and interpreting κ. Although κ is considered to be caused solely by damping in the shallow crust, measurement techniques often cannot separate the effects of damping and amplification, and yield the net effect of both phenomena.

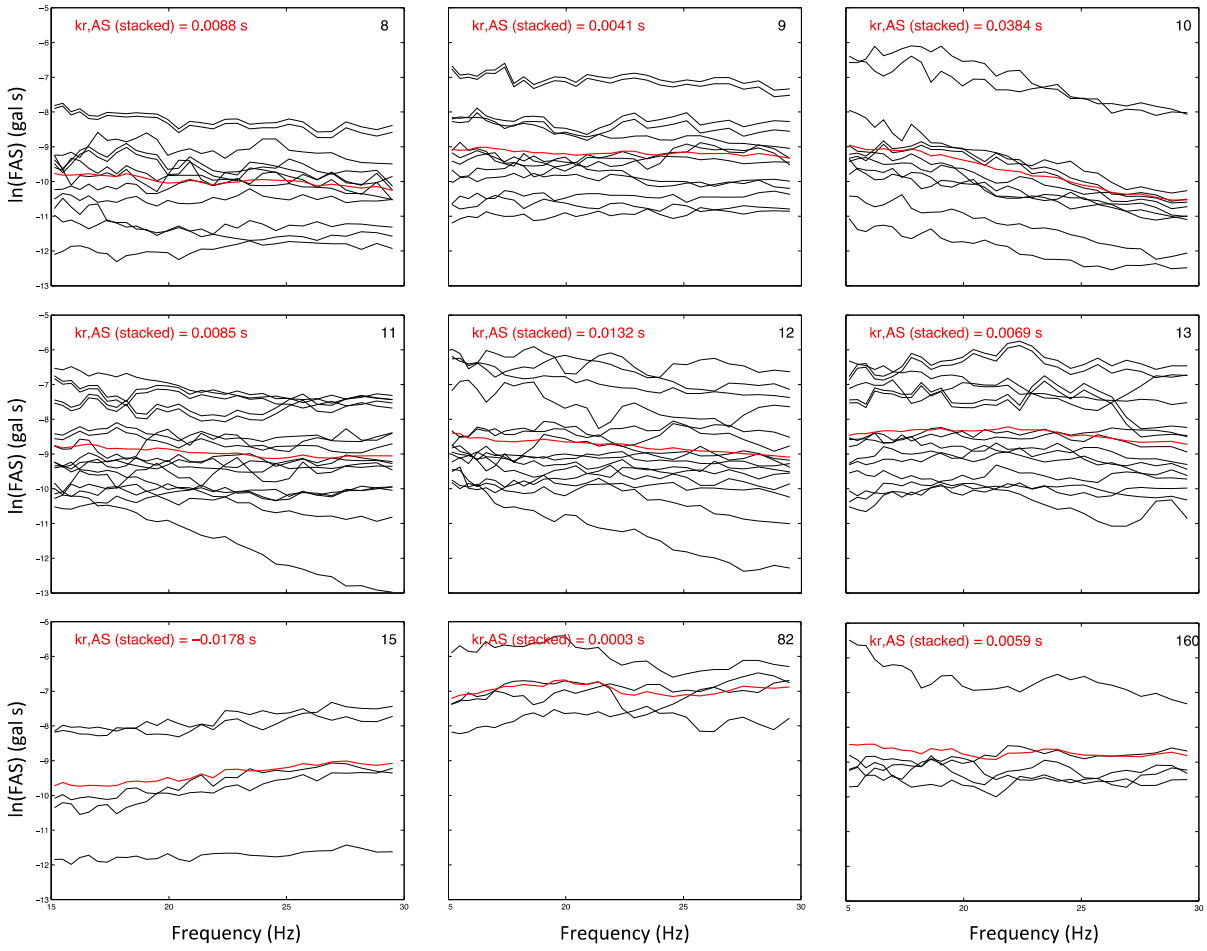

Figure 3.26 **Mean FAS derived from stacking all recordings per station for the AS approach, and estimation of mean κ_{0_AS} per site (red). Individual FAS are shown in black. The station number is written on the top right.**

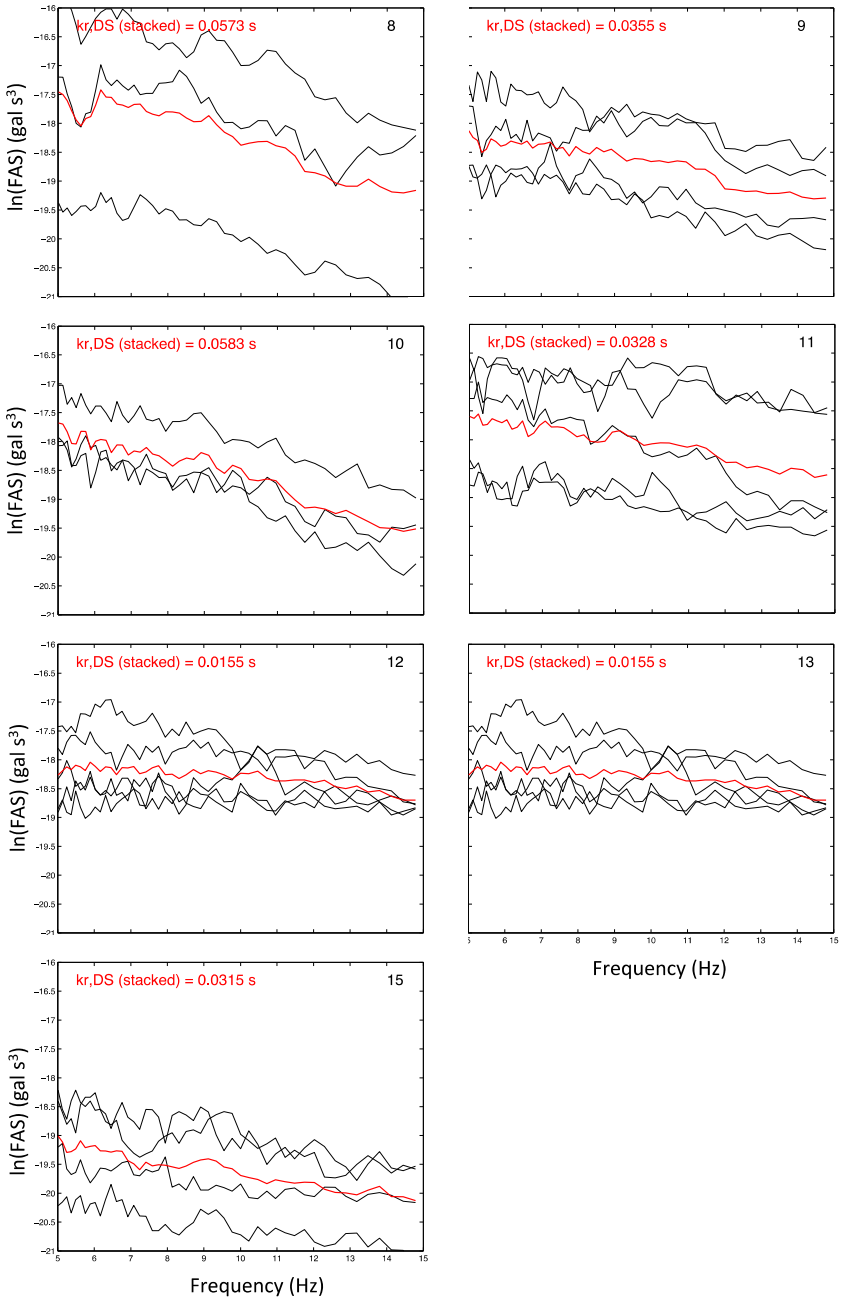

Figure 3.27 **Mean FAS derived from stacking all recordings per station for the DS approach, and estimation of mean κ_{0_DS} per site (red). Individual FAS are shown in black. The station number is written on the top right.**

Table 3.7 Mean κ measurements per station from stacked FAS (AS approach).

Station #	Flag	N_{rec} (all flags)	κ_{r_AS} (sec): 15–30 Hz - (all flags)	N_{rec} (flags 0, 1)	κ_{r_AS} (sec): 15–30 Hz - (flags 0, 1)
8	-1,0,1	12	0.0088	11	0.0093
9	-1,0,1	13	0.0041	12	0.0049
10	1	11	0.0384*	**11**	0.0384
11	-1,0,1	17	0.0085	12	0.0134
12	0,1	15	0.0132*	**15**	0.0132
13	-1,0,1	15	0.0069	12	0.0057
15	-1	5	-0.0178	0	-
82	-1,0,1	4	0.0003	3	0.0023
160	1	5	0.0059*	5	0.0059
Mean (s)			**0.0075 (only *: 0.0190)**		**0.0116**
Standard deviation (s)			**0.0146 (only *: 0.0149)**		**0.0149**
Standard deviation (ln)			**1.33 (0.81)**		**0.9**

Table 3.8 Mean κ measurements per station from stacked FAS (DS approach).

Station #	V_{s30} (m/sec)	N_{rec}	Flag	κ_{r_DS} (s): 5–15 Hz
8	2000	3	1	0.0573
9	2000	4	1	0.0355
10	2000	3	1	0.0583
11	2000	5	0,1	0.0328
12	2000	5	0,1	0.0155
13	2000	5	0,1	0.0155
15	2000	4	0,1	0.0315
82	2000	-	-	-
160	2000	-	-	-
Mean (sec)				**0.0352**
Standard deviation (sec)				**0.0175**
Standard deviation (ln)				**0.54**

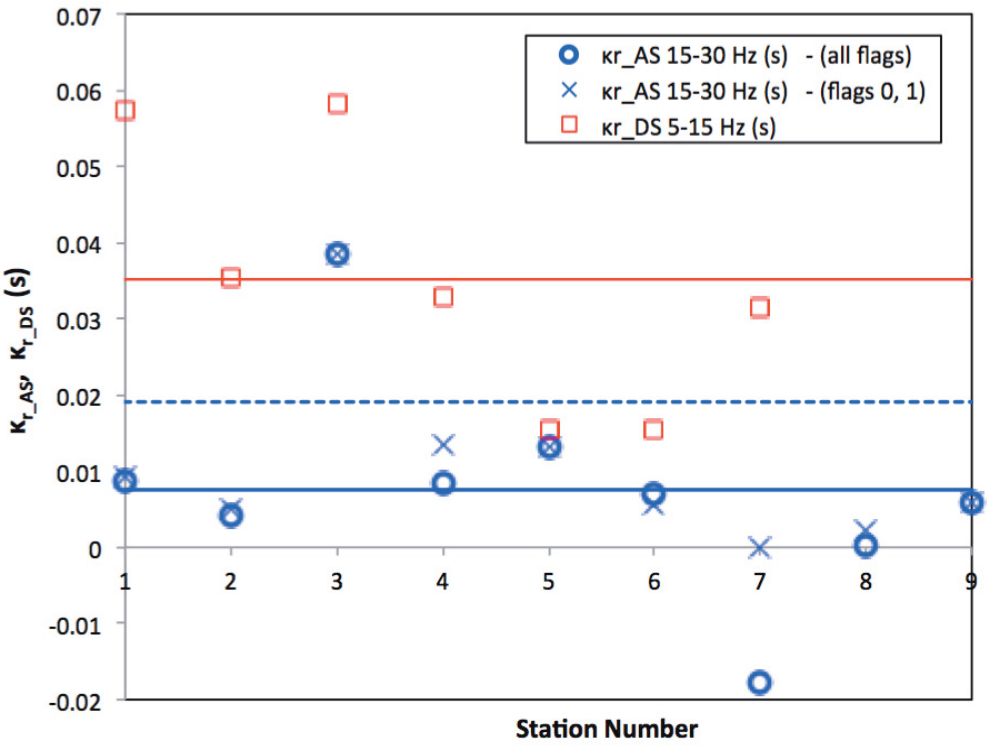

Figure 3.28 **Mean κ_r derived from stacking all recordings per station for the AS (red) and DS (blue) approach, plotted against the number of stations. For the AS results for all flags (circles and solid line) and without -1 flags (crosses and dashed line) are shown. Symbols indicate station values and lines indicate average over stations.**

3.3 BROADBAND APPROACH

In Chapter 3 of PEER (2015), the BB approach was applied to the NGA-East FAS data, which were recorded at 241 stations from 53 events (listed in Table 3.9); 1133 recordings were analyzed. The maximum distance was 250 km for TA data and 1000 km for all other stations. The stations were grouped into the five NEHRP site classes. The ten earthquake names (EQ Name) are followed by the indication 'PIE,' which are Probably Induced Earthquakes in the dataset [PEER 2015]. These shallow events occurred mainly in Oklahoma and Arkansas. Inversions were performed with and without these data. The amplification factors computed in PEER [2015)] for each site class have been shown in Figure 3.14.

A total of 351 recordings came from class A from 43 events recorded at 43 stations. Q_0 and κ estimates for the five NEHRP classifications were solved for in the inversion. η and R_0 were held fixed at 0.5 and 50 km, respectively. The Brune [1970; 1971] source model parameters V_s and ρ were also fixed at 3.8 km/sec and 2.8 gm/cm^3. For NEHRP site class A, the estimated mean κ_{0_BB} is 0.0049±0.0004 sec. The results of the inversion from all the data in Table 3.9 are summarized in Table 3.10. The results from NEHRP site class E were not considered statistically significant due to the small (n = 6) recordings in the dataset. The κ_{0_BB} estimates resulting from the inversion are similar for NEHRP A and B, as well for NEHRP C and D (Table 3.10).

Table 3.9 List of class-A recordings used in BB approach.

#	EQID	M	R_h (km)	No. recs	Class A	Class B	Class C	Class D	Class E	< 50 km	50–100 km	100–250 km	> 250 km	EQ name
1	5	5.81	21.47	19	12	3	4	0	0	0	7	8	4	Saguenay
2	6	3.27	7.5	5	5	0	0	0	0	5	0	0	0	La Malbaie, QC
3	7	4.29	5	6	6	0	0	0	0	5	1	0	0	La Malbaie, QC
4	8	4.46	22	7	7	0	0	0	0	1	1	5	0	Cap-Rouge, QC
5	9	4.44	20	5	5	0	0	0	0	0	0	0	5	Cote-Nord, QC
6	10	4.63	13	3	3	0	0	0	0	0	0	1	2	Kipawa, QC
7	11	3.29	11.4	6	6	0	0	0	0	5	1	0	0	La Malbaie, QC
8	12	3.65	18	8	7	0	1	0	0	1	6	1	0	Laurentide, QC
9	13	3.11	18	6	6	0	0	0	0	0	5	1	0	Laurentide, QC
10	16	5	5	19	5	7	4	3	0	0	2	8	9	Au Sable Forks, NY
11	17	3.78	2	8	8	0	0	0	0	0	0	0	8	Lac Laratelle, QC
12	18	4.55	17	7	0	4	2	1	0	0	0	1	6	Caborn, IN
13	24	3.56	11.1	23	12	5	4	2	0	7	1	0	15	La Malbaie, QC
14	25	3.82	18	35	17	7	8	2	0	0	0	8	26	Bark Lake, QC
15	28	2.87	22	6	6	0	0	0	0	0	6	0	0	La Baie, QC
16	29	3.1	4	33	8	11	10	4	0	0	0	1	32	Prairie Center, IL
17	30	3.1	4	28	8	10	7	3	0	1	3	15	9	Port Hope, ON
18	32	4.6	12.3	43	23	9	10	1	0	11	4	2	26	Rivière du Loup, AS
19	35	3.75	16	46	20	14	7	5	0	5	1	12	28	Thurso, ON
20	36	2.59	18	16	7	4	4	1	0	1	3	7	5	Hawkesbury, ON
21	37	3.77	25	36	21	7	6	2	0	7	4	0	25	Baie St Paul
22	44	2.8	5	26	7	8	8	3	0	3	5	11	7	Cobourg, ON
23	45	2.77	13.5	8	8	0	0	0	0	5	2	1	0	Baie St Paul
24	46	5.27	14	16	0	4	8	4	0	3	3	9	1	Mt Carmel, IL
25	47	4.64	14	14	0	3	8	3	0	2	3	8	1	Mt Carmel, IL
26	48	4.03	15	14	0	3	8	3	0	2	3	8	1	Mt Carmel, IL

#	EQID	M	R_h (km)	No. recs	Class A	Class B	Class C	Class D	Class E	< 50 km	50–100 km	100–250 km	> 250 km	EQ name
27	49	3.75	13	13	0	3	7	1	0	2	3	6	2	Mt Carmel, IL
28	50	2.97	18	24	7	7	6	3	1	3	0	6	15	Buckingham, QC
29	51	3.6	13.3	32	17	7	5	2	1	4	2	1	25	Rivière du Loup, AS
30	55	2.57	26.1	21	5	7	7	1	1	3	1	6	11	Constance Bay, ON
31	56	3.84	8	22	1	1	19	1	0	1	3	18	0	Jones, OK (PIE)
32	57	4.18	4	23	0	2	20	1	0	4	5	12	2	Lincoln,, OK (PIE)
33	59	2.62	20.8	5	0	1	2	2	0	4	1	0	0	Lebanon, IL
34	60	5.1	22	52	21	8	19	3	1	0	8	11	33	Val-des-Bois
35	61	3.51	13	22	8	6	6	2	0	0	0	4	18	St. Fravien, QC
36	63	4.48	11	8	5	2	1	0	0	0	0	3	5	Mont Laurier, QC
37	66	4.36	14	52	1	6	42	4	0	10	6	32	4	Slaughterville, OK (PIE)
38	67	3.86	5	10	0	3	7	0	0	2	1	7	0	Guy, AR (PIE)
39	73	3.96	3	47	1	5	39	2	0	9	5	33	0	Arcadia, OK (PIE)
40	74	3.23	4	44	1	6	35	2	0	9	3	32	0	Bethel Acres, OK (PIE)
41	75	3.85	14	31	4	7	16	4	0	0	0	4	27	Greentown, IN
42	76	3.9	5	12	0	4	7	1	0	3	1	7	1	Guy, AR (PIE)
43	80	4.68	4	25	0	12	9	3	0	3	3	14	5	Greenbrier, AR (PIE)
44	81	3.89	27	38	1	11	19	7	0	1	3	23	11	Sullivan, MO
45	83	2.57	16.7	36	14	12	9	1	0	8	2	7	19	Val-des-Bois, AS
46	84	2.37	19.9	24	9	11	2	1	1	8	1	8	7	Val-des-Bois, AS
47	85	3.63	7	46	19	11	13	3	1	1	4	5	36	Hawkesbury, ON
48	86	3.6	11.4	8	8	0	0	0	0	7	1	0	0	Charlevoix
49	87	3.24	13.3	16	8	3	3	2	0	4	3	0	9	Baie St Pul
50	90	4.73	3	43	1	9	32	1	0	3	5	21	14	Sparks, OK (PIE)
51	91	5.68	8	24	1	5	17	1	0	4	1	15	4	Sparks, OK (PIE)
52	116	4.19	28	6	6	0	0	0	0	0	2	4	0	Saguenay, FS
53	117	3.5	30	6	6	0	0	0	0	0	0	6	0	Saguenay, AS

Table 3.10 Results for attenuation parameters from the broadband inversion.

NEHRP classification	κ_{0_BB} (sec)	$Q(f)$
A	0.0049 ± 0.0004	$630 \bullet f^{0.5}$
B	0.0049 ± 0.0005	
C	0.0134 ± 0.0005	
D	0.0111 ± 0.0009	

Figures 3.29, 3.30 and 3.31 show the fit to the FAS for three example events, shown in decreasing magnitude: the Rivière du Loup event (**M**4.6), recorded at 17 NEHRP site class-A sites; the Laurentide event (**M**3.65) recorded at 7 NEHRP site class-A sites; and Val de Bois (**M**2.57), recorded at 14 NEHRP class-A sites. The spectra are shown with both log-log and log-lin scale to facilitate the observation of spectral characteristics such as corner frequency and κ. For several sites in Canada (e.g., St Simeon, La Malbaie, and others) site-resonance patterns due to shallow impedance contrasts are observed. These resonances were not removed when the FAS were corrected with the generic crustal amplification function for site classification A1 (Figure 3.14). This again indicates the need for better site characterization in CENA. For the intermediate magnitude events shown in Figures 3.29 and 3.30, it is possible to observe the f_c, plateau and κ/Q decay on most of the spectra. However, at the La Malbaie, Canada, site, only κ can be resolved in Figure 3.29 and f_c in Figure 3.30. At the Sept Chutes site, the opposite pattern is observed, only f_c on Figure 3.29 and κ on Figure 3.30. In contrast, for the small magnitude event in Figure 3.31, it is difficult to resolve f_c (which most likely lies at frequencies above the available bandwidth), and κ. As mentioned earlier, this may also be due to shallow site resonance, especially broadband amplification effects, which may interfere with the measurement of κ. As mentioned earlier, a CENA site with shallow soil and weather rock over hard rock had a site resonance near 60 Hz [R. B. Darragh, *personal communication*, 2015]. Therefore, recordings from small magnitude events at these very hard sites require large high-frequency bandwidths (high sample rates) to resolve κ and f_c. The final model shown on these figures provides an adequate fit to the FAS data for these NEHRP A sites for distances ranging from about 10 to 500 km.

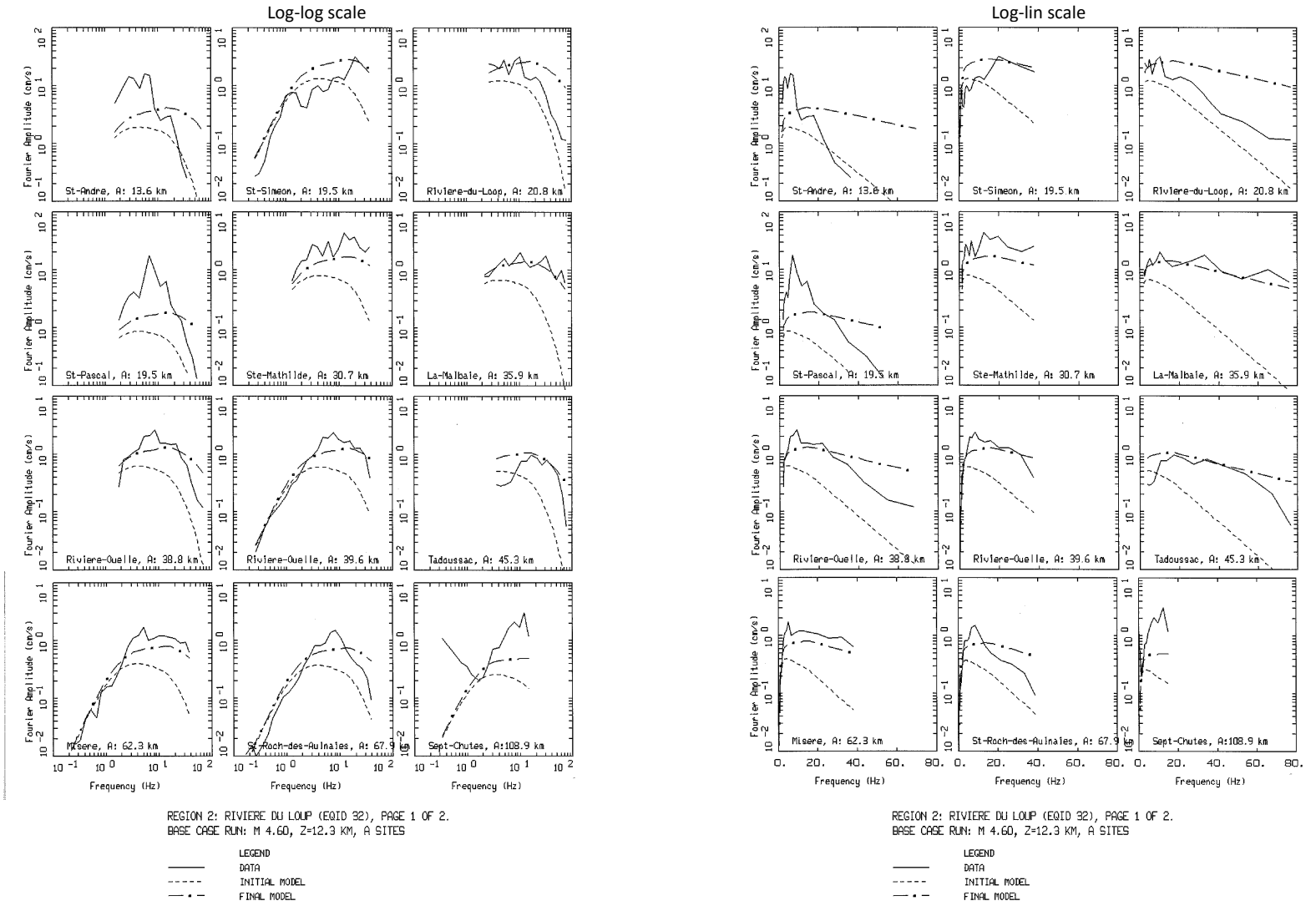

Figure 3.29 The broadband inversion fits of the FAS for Rivière du Loup event (M4.6) on log-log (top) and log-lin scale (bottom).

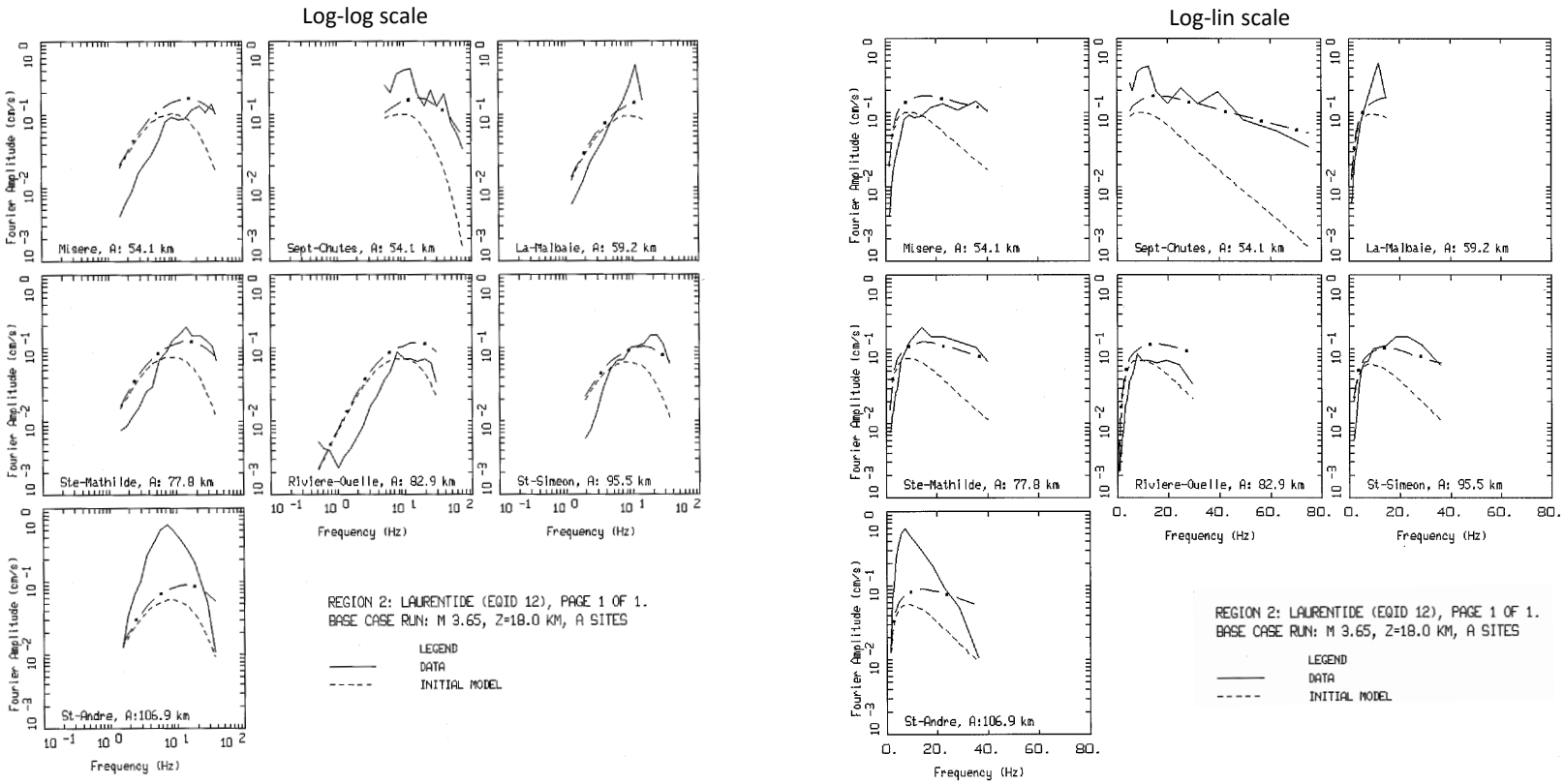

Figure 3.30 The broadband inversion fits of the FAS for Laurentine event (M3.65) on log-log (top) and log-lin scale (bottom).

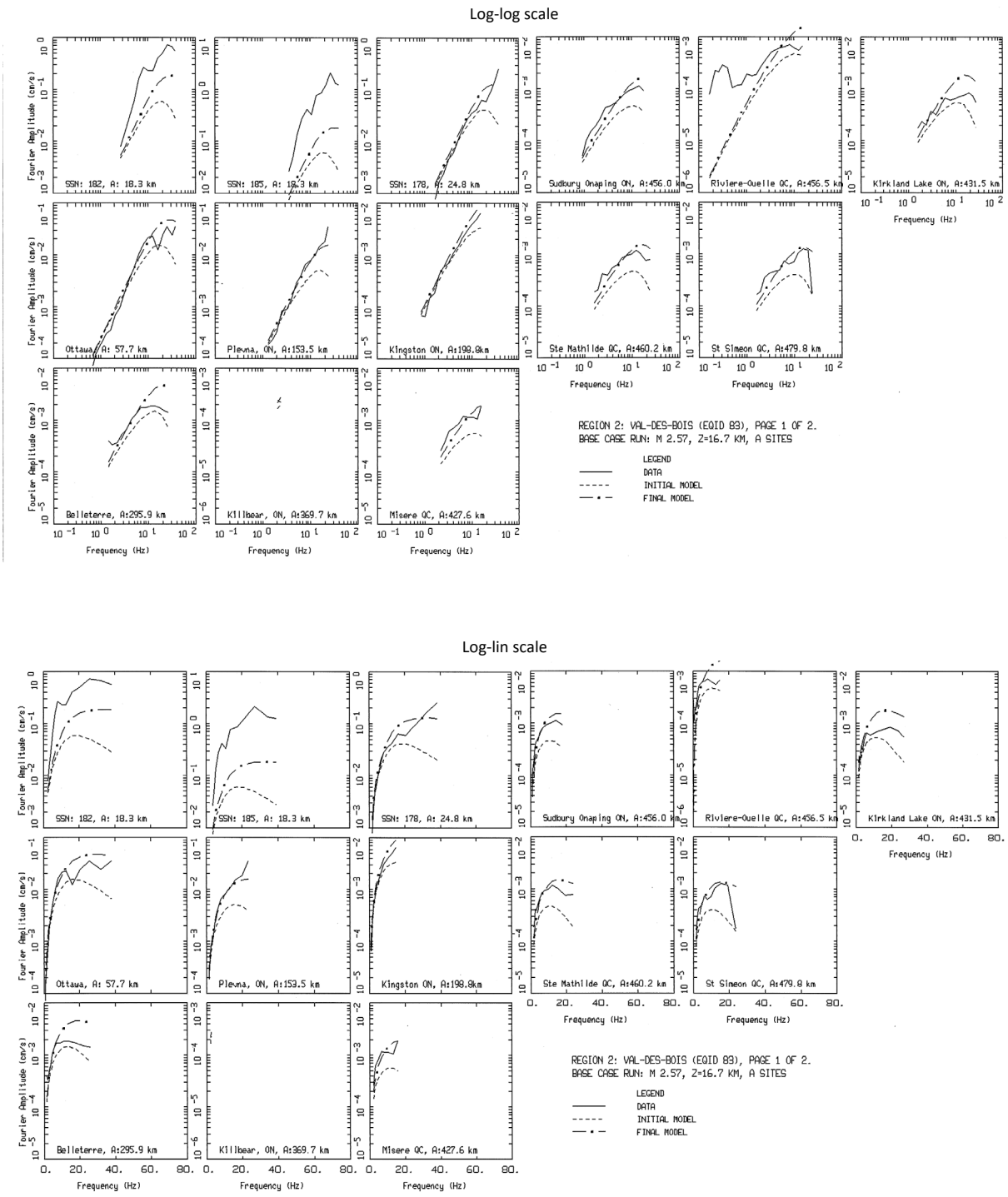

Figure 3.31 The broadband inversion fits of the FAS for Val de Bois event (M2.57) on log-log (top) and log-lin scale (bottom).

3.4 SPECTRAL SHAPE APPROACH

Figure 3.32 shows the spectral shape for two of the three example events examined previously in the BB method: Rivière du Loup (**M**4.6), and Val de Bois (**M**2.57). The Laurentide earthquake (EQID 12 in Table 3.9) was not included in this analysis because there was only one recording at a distance less than 50 km. As discussed in Section 2.5, for this example all NEHRP site class-A recordings within 50 km were averaged together. Figure 3.32 shows the average (ln), maximum and minimum response spectral shape. Eighteen and six horizontal components from NEHRP sites A were used for Rivière du Loup and Val de Bois, respectively.

The model shape shown on the figures is from PSSM (RASCALS: Silva and Lee [1987], as validated in Silva et al. [1997]) with a distance of 30 km (near the average epicentral distance for these stations for each event), $Q(f)$ is from the inversion (Table 3.10), and for consistency the other parameters [e.g., stress parameter, amplification factor (Figure 3.14), R_o, β, and ρ] are the same as in the inversion (Section 3.3). The PSSM model includes a low-pass filter at 40 Hz to approximately account for the anti-alias filter or processing filter used in the NGA-East dataset for these recordings.

As discussed in Section 2.5, κ is most sensitive to the frequency and width of the peak in the spectral shape. For these CENA events the peak is near 20 to 30 Hz. The moment magnitude in PSSM controls the longer period response greater than about 0.3 sec for these two earthquakes (Table 3.9). The κ used in these examples provides an adequate fit. Slightly larger values may provide a slightly better fit. The moment magnitude for the smaller event was increased from 2.57 to 3.0 to improve the fit at periods longer than about 0.3 sec.

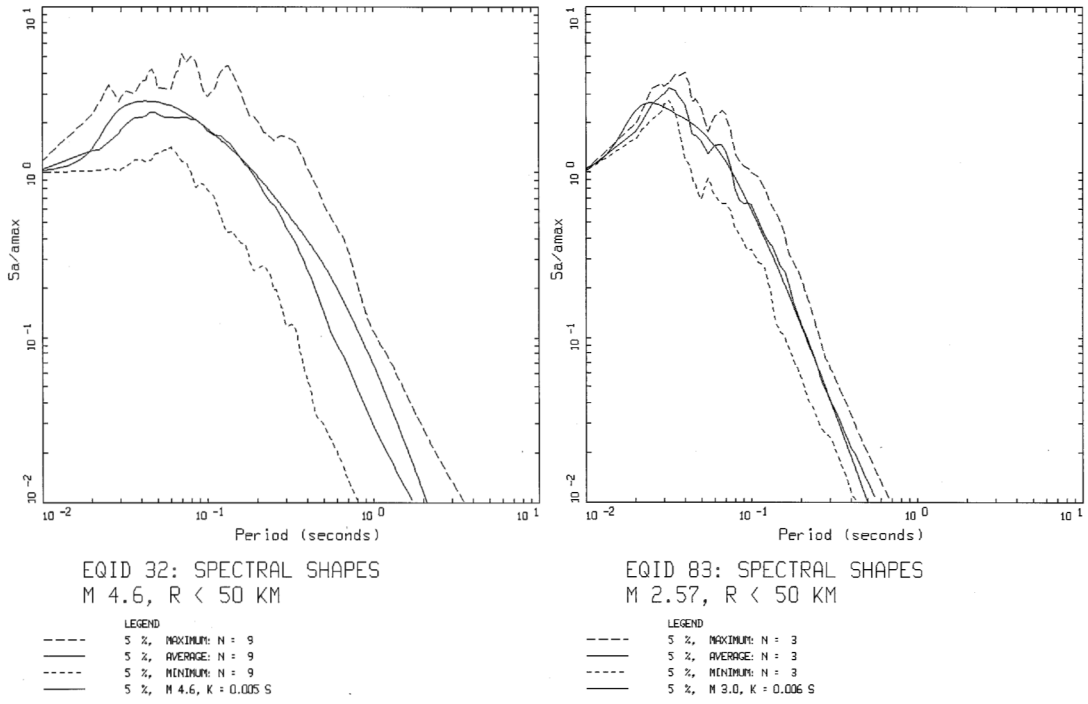

Figure 3.32 The mean normalized PSA (minimum and maximum) for recordings within 50 km for events Rivière du Loup (M4.6, left) and Val de Bois (M2.57, right).

Table 3.11 Example results from the κ_{RESP} approach.

	Rivière du Loup	Val de Bois
κ_{0_RESP} (sec)	0.005	0.006

3.5 COMPARING APPROACHES

Working with different approaches helps quantify epistemic uncertainty, especially for small events, and in the face of large stress-drop uncertainties.

Concerning the band-limited approaches, DS has generally been observed on other studies to provide an upper limit to κ estimates; this is also observed with these data. Comparing κ_{r_AS} (above **M**3 to avoid source effects) and κ_{r_DS} (below **M**3.5), we find a difference between them of a factor of 1.7 for flag 1 recordings (Table 3.5). This factor doubles when all recordings are analyzed. The κ_{r_DS} estimates also have larger uncertainty, and are more sensitive to the crustal amplification correction. The mean κ_{r_AS} values for all flags, for flags 0 and 1, and for flag 1, are: 8, 15 and 25 msec, respectively. The mean κ_{r_DS} values for these groups are: 27, 35 and 42 msec. Combining AS and DS results, the mean values are: 13, 20, and 30 msec. The mean κ values measured from stacking all available FAS together (and all flags) are 6.6 and 29.4 msec for the AS and DS approach, respectively. Finally, when stacking the FAS for individual sites with more than three recordings, the mean values of κ_{r_AS} for all flags, for flags 0 and 1, and for flag 1, are: 8, 12, and 19 msec, respectively. The mean κ_{r_DS} is 35 msec (there are no flags -1). Results from individual and stacked recordings are similar.

The two broadband approaches, BB and RESP, yield similar results in these examples. The mean κ_{0_BB} is 5±0.5 msec across all NEHRP class A sites. The κ_{0_RESP} for the two events examined is about 5 and 6 msec. These values are similar to the mean κ_{r_AS} values computed for all recordings taken together (all flags) of 6.6 msec, whether on individual or on the stacked FAS.

Campbell et al. [2014] performed a literature review on κ_0 values for very hard rock (which was defined at V_s = 3000 m/sec; in this study, V_s = 2030 m/sec was assumed for hard rock based on PEER [2015]). Those authors concluded that the average value of κ_0 in CENA is 6±2 msec. Table 3.12 reproduces their Table 1, and summarizes the review in Campbell et al. [2104]. Of the references therein, three were based on f_{max}, three on the κ_{RESP} method, and three on κ_{AS} (the DS method was not used). The value proposed is the same value given by EPRI [1993], for V_s = 2830 m/sec) and is consistent with other studies listed by the authors. We note that the mean values of Campbell et al. [2014], which represent the typical values considered for CENA very hard rock, are similar to the broadband estimates (κ_{0_RESP}, κ_{0_BB}) of this study, and to the mean κ_{r_AS} when all available recordings are used along with all flags. When only recordings with down-going FAS slope are selected from the dataset, the mean value of κ_{r_AS} increases by a factor of 2–3 (e.g., most recordings from the Val de Bois event are flagged as -1, and their presence in the analysis lowers the mean κ).

Finally, two issues should be emphasized:

- The lack of site characterization (e.g., V_s profile to 30 m or greater) in CENA for hard-rock sites, which does not allow the determination of whether part of the observed dispersion of κ values might be explained by differences in site hardness.
- The possible trade-off/coupling between site attenuation and site amplification (a possible source for the flag -1 FAS is near surface site amplification due to a large impedance contrast), which may contribute towards lower κ values.

Table 3.12 Summary of literature review on hard-rock κ_0 values in CENA (from Campbell et al. [2014]).

Source	Mean κ_0 (sec)	Range κ_0 (sec)	Comments
Atkinson [1984]	0.006	-	Based on f_{max} = 50 Hz
Atkinson [1984]	0.009	-	Based on f_{max} = 50 Hz
Toro and McGuire [1987]	0.008	-	Based on f_{max} = 50 Hz
Darragh et al. [1989]	0.006	-	-
Silva and Darragh [1985]	0.007	0.004–0.016	Including Monticello Reservoir
Silva and Darragh [1985]	0.006	0.004–0.008	Excluding Monticello Reservoir
Atkinson [1996]	0.002	0–0.004	4–30 Hz
Chapman et al. [2003]	0.000	0–0.018	Monticello Reservoir
Campbell [2009]	0.004	0–0.007	12–22 Hz [Atkinson 1996]
Atkinson and Boore [2006]	0.005	0–0.01	Data from Atkinson [2004]

4 Residuals with κ_0

4.1 INTRODUCTION

A common approach for evaluating the significance of an additional predictive parameter is to plot the residuals versus the parameter of interest. This chapter evaluates the residuals of the high-frequency ground motion at hard-rock sites as a function of the κ values estimated in Chapter 3.

4.2 EMPIRICAL DATA FOR RESIDUALS FOR HARD-ROCK SITES

A key difficulty for empirical estimates of the κ scaling has been the sparse datasets for hard-rock sites. Furthermore, when the dataset is restricted to short distances to avoid significant trade-offs between Q effects and κ effects, the number of hard-rock site recordings is even more limited. For example, the V_{s30} sampling of the NGA-West2 dataset [Ancheta et al. 2014] versus rupture distance is shown in Figure 4.1. Although the NGA-West2 dataset consists of over 20,000 recordings, it only includes three recordings from sites with $V_{s30} > 1500$ m/sec at rupture distances less than 50 km (Table 4.1). The recently developed NGA-East dataset has a better sampling of hard-rock sites at short distances, as shown in Figure 4.2. The NGA-East dataset includes 64 hard-rock recordings within 50 km, and 116 recordings within 100 km that are reliable at 20 Hz (Table 4.1).

Table 4.1 Number of recordings included in major North American datasets for hard-rock sites.

Dataset	Region	Maximum rupture distance (km)	Number of recordings with $V_{S30} > 1500$ m/sec	
			Useable at 0.05 sec (20 Hz)	Useable at 0.03 sec (33 Hz)
NGA-West2	Global	50	3	3
NGA-East	CEUS	50	64	61
NGA-East	CEUS	100	116	105

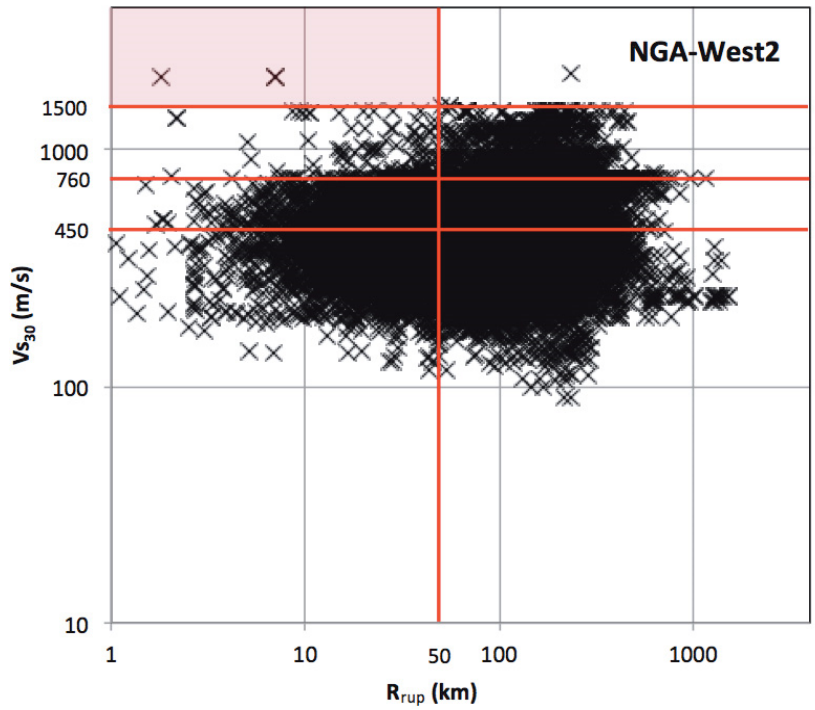

Figure 4.1 Distribution of rupture distance and V_{s30} for the NGA-West2 dataset.

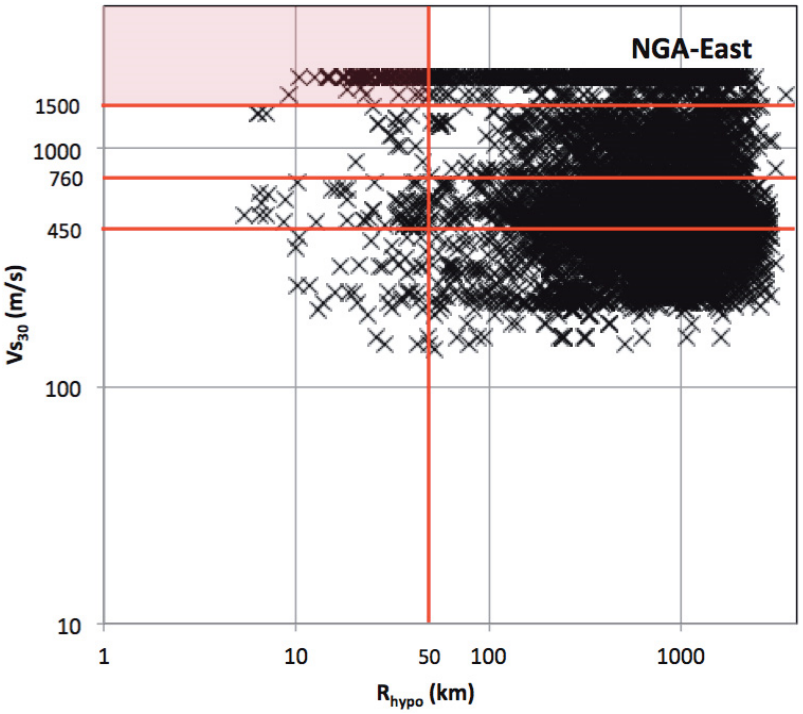

Figure 4.2 Distribution of hypocentral distance and V_{s30} for the NGA-East dataset.

4.3 κ DEPENDENCE OF RESIDUALS

Using the NGA-East subset of hard-rock data at short distances described in the previous section, the residuals were computed with respect to the reference GMPE derived from the NGA-East data [J. Hollenback, *personal communication*, 2015]. The regression was conducted using the random-effects method, which partition the residuals into between-event and within-event residuals. The dependence on κ is a site term that should be part of the within-event residual; however, for this case, we evaluated the κ scaling using both the within-event and the total residual because there may be a trade-off between κ and the event term. For example, if the regional variations in κ extend over large regions, then the regional differences in κ may be mapped into the event terms (e.g., if all of the recordings from an earthquake are from a region with low κ sites, then the average effect of κ would be manifest in the event term).

In the example application of Chapter 3, we estimated the κ values for rock sites in the NGA-East dataset with the AS and DS approaches. These κ values were used for plotting the residuals versus κ. For some recordings, the estimated κ was negative, indicating that there was a positive slope of the FAS with frequency, which suggests that there are some site response effects not removed from the FAS that map onto κ. In the evaluation of the κ scaling in the residuals, we used the three different subsets of the data described in Chapter 3 (Figure 3.16), with respect to the flags defined there (all flags, only flags 0 and 1, and only flag 1).

Figures 4.3, 4.4, and 4.5 show the total residuals for hard-rock sites at high frequencies (10, 20, and 30 Hz), against the estimated κ_0 values for sites at distances of less than 100 km. Figures 4.6, 4.7, and 4.8 show the corresponding between-event residuals. The residuals are shown for three cases, using different subsets of κ based on the FAS flags (down-trending, almost flat, and up-trending) and also using the AS and DS κ values. The two lines indicate the theoretical scaling of total residuals with κ_0, as predicted from the PSSM (blue line, from 0.020 to 0.005 sec) and from the IRVT approach (red line, from 0.020 to 0.010 sec). If the site factor for hard-rock sites scales strongly with κ_0—as indicated by the modeling—then we would expect to see a strong negative correlation of the residuals versus κ_0, as small κ_0 values will lead to higher ground motions and therefore larger residuals. When it comes to the κ_{AS} values (left-hand panels of Figures 4.3–4.8), the residuals between κ_0 of 0.020 to 0.005 sec do not show the strong trend that is predicted by the analytical models. Figures 4.6, 4.7, and 4.8 show the same sets of plots for the within-event residuals for hard-rock sites. The trends of the within-event are similar to those from the total residuals.

Based on the residual plots shown in Figures 4.3–4.8, the high-frequency response spectral values of the NGA-East hard-rock data do not show the expected dependence on κ_0, when that is computed with the AS approach. However, the residuals with respect to κ_{DS} measurements (right-hand panels of Figures 4.3– 4.8) seem to scale more strongly and more consistently with the theoretical scaling.

To interpret this observation, we recall the frequency ranges in which each of the two approaches was applied (Figure 3.24). κ_{AS} was measured on the acceleration FAS mostly in the range of 15–35 Hz, while κ_{DS} was measured on the displacement FAS mostly in the range of 5–15 Hz. Figure 3.24 also plots the crustal amplification transfer function, which was computed for the generic hard-rock profile in CENA, and which was used to correct all FAS before κ measurement. The crustal amplification according to this function takes place below 15 Hz;

therefore, the correction of the FAS mostly affects the results of the DS approach. It is possible that there is amplification above 15 Hz that is not computed by the generic profile due to lack of small-scale information that would affect high frequencies. In this case, it would mean that the κ_{DS} measurements better reflect the damping in the shallow crust, while the κ_{AS} measurements may reflect a net effect of damping and amplification that has not been decoupled. This would imply that, should we be able to correct the FAS above 15 Hz, the residuals might scale more strongly with κ_{AS} values, as they do with κ_{DS} values.

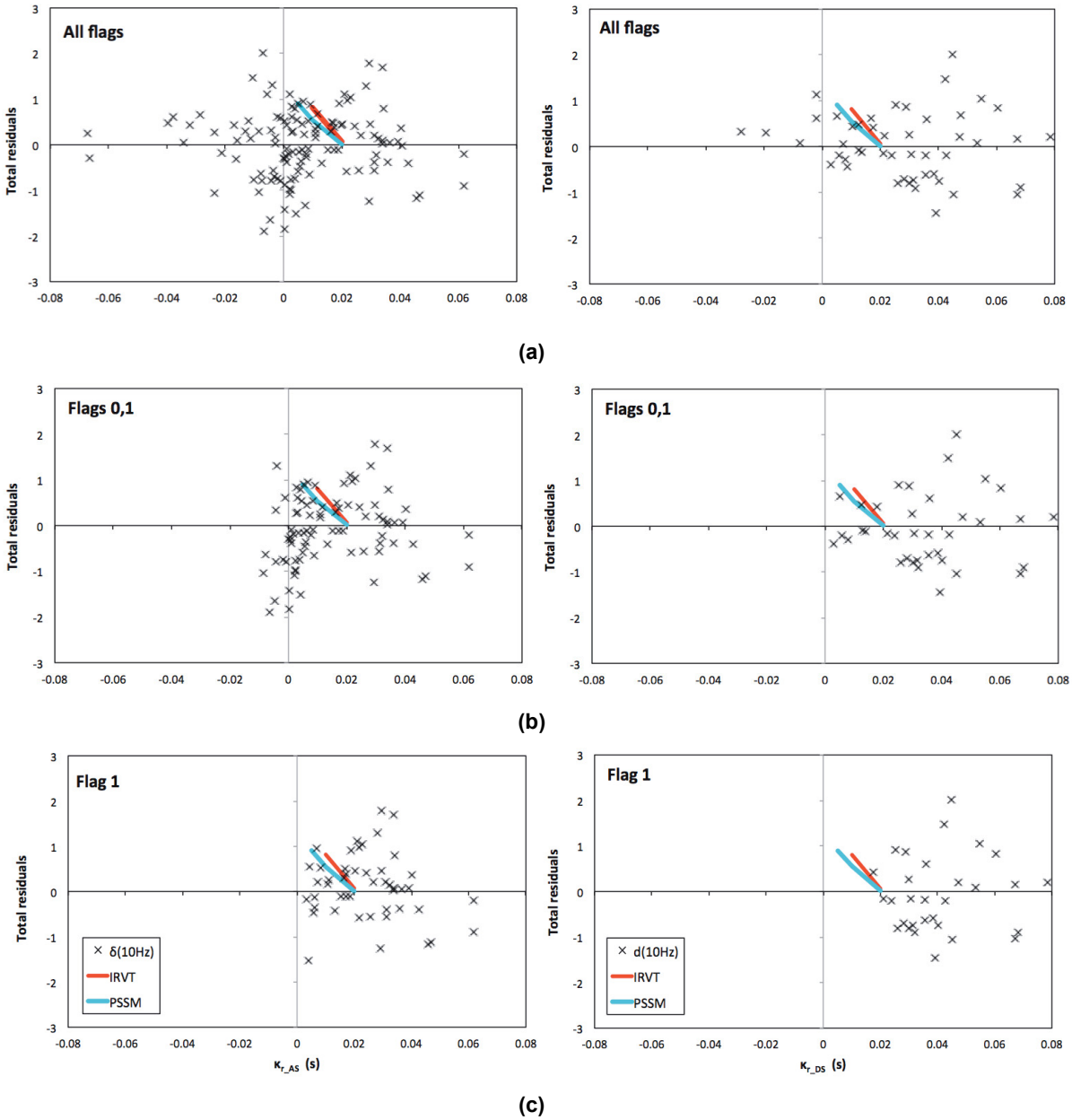

Figure 4.3 **<u>Total</u> residuals at <u>10 Hz</u> for the PEER model [2015] versus measured κ_{r_AS} values (left) and κ_{r_DS} values (right) for: (a) all recordings; (b) recordings without significant up-going trend in their FAS, and (c) recordings with clear down-going trend in their FAS. The blue and red lines show the theoretical scaling predicted from the PSSM and IRVT.**

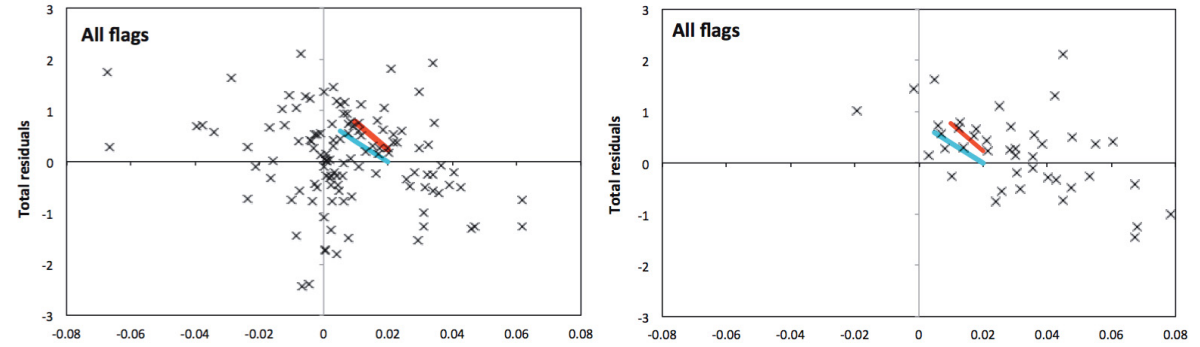

(a)

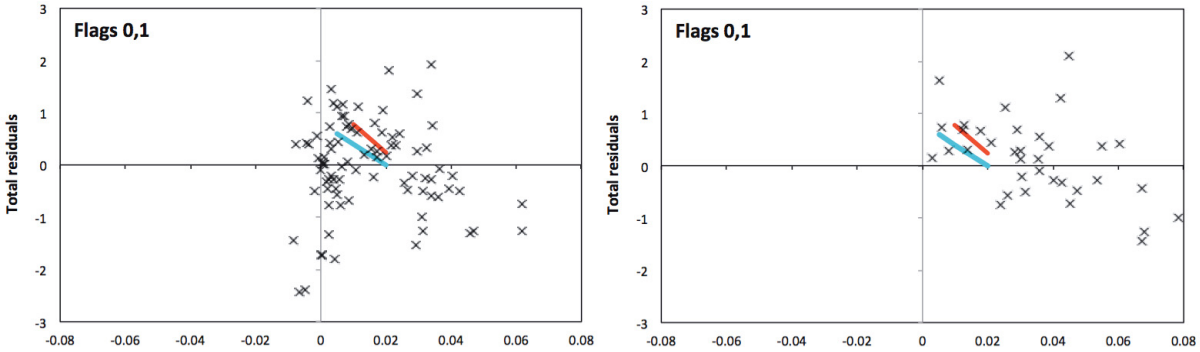

(b)

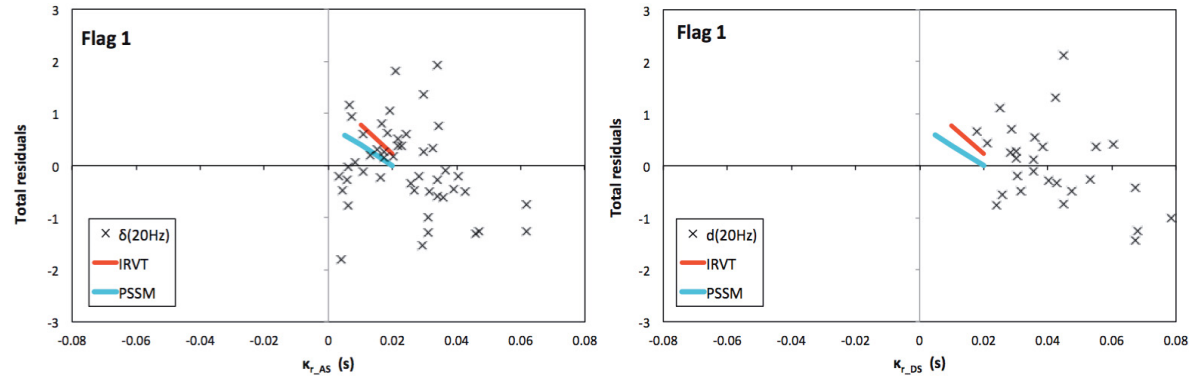

(c)

Figure 4.4 **<u>Total</u> residuals at <u>20 Hz</u> for the PEER model [2015] versus measured κ_{r_AS} values (left) and κ_{r_DS} values (right) for: (a) all recordings; (b) recordings without significant up-going trend in their FAS; and (c) recordings with clear down-going trend in their FAS. The blue and red lines show the theoretical scaling predicted from the PSSM and IRVT.**

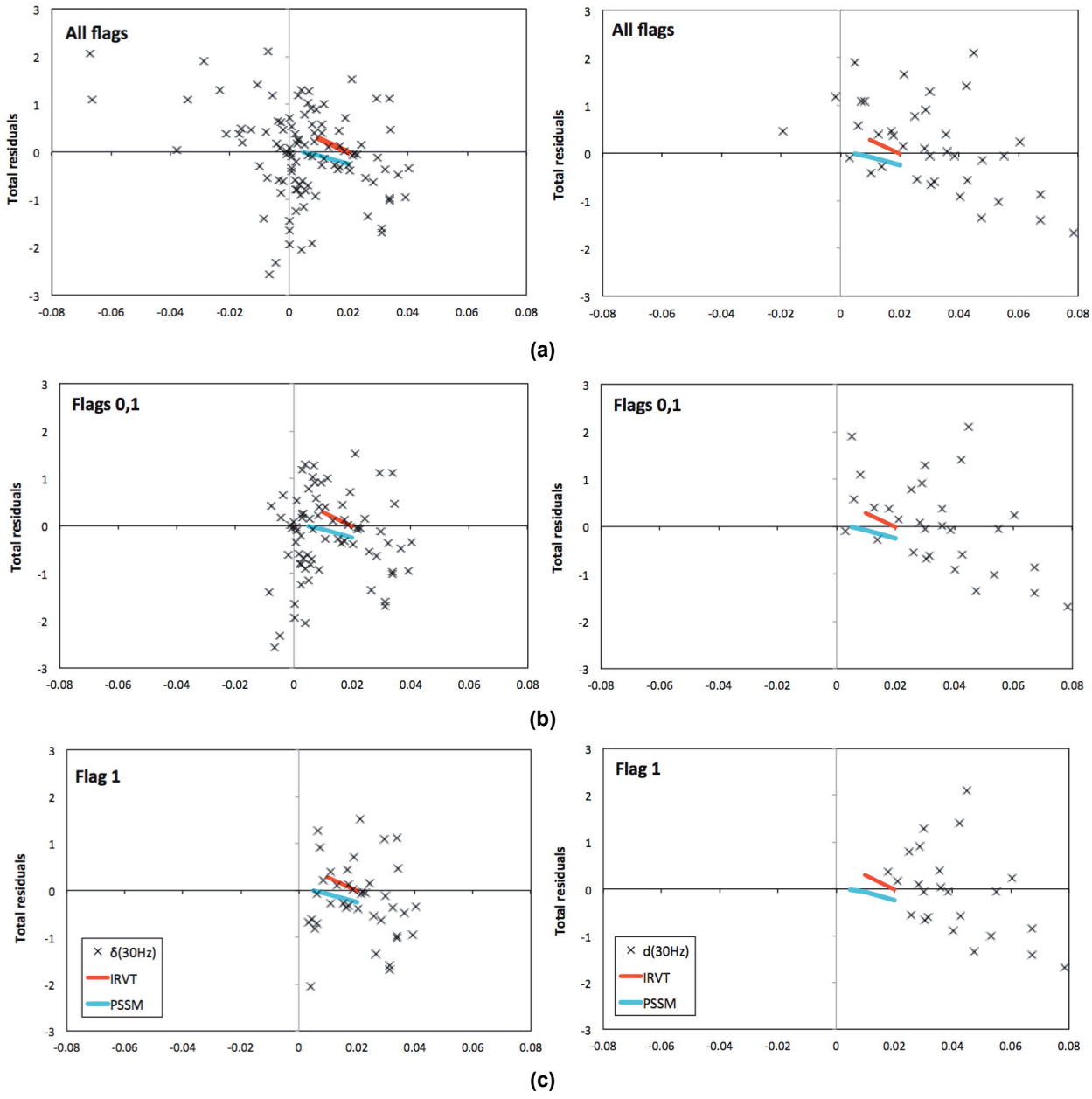

Figure 4.5 **Total residuals at 30 Hz for the PEER model [2015] versus measured κ_{r_AS} values (left) and κ_{r_DS} values (right) for: (a) all recordings; (b) recordings without significant up-going trend in their FAS; and (c) recordings with clear down-going trend in their FAS. The blue and red lines show the theoretical scaling predicted from the PSSM and IRVT.**

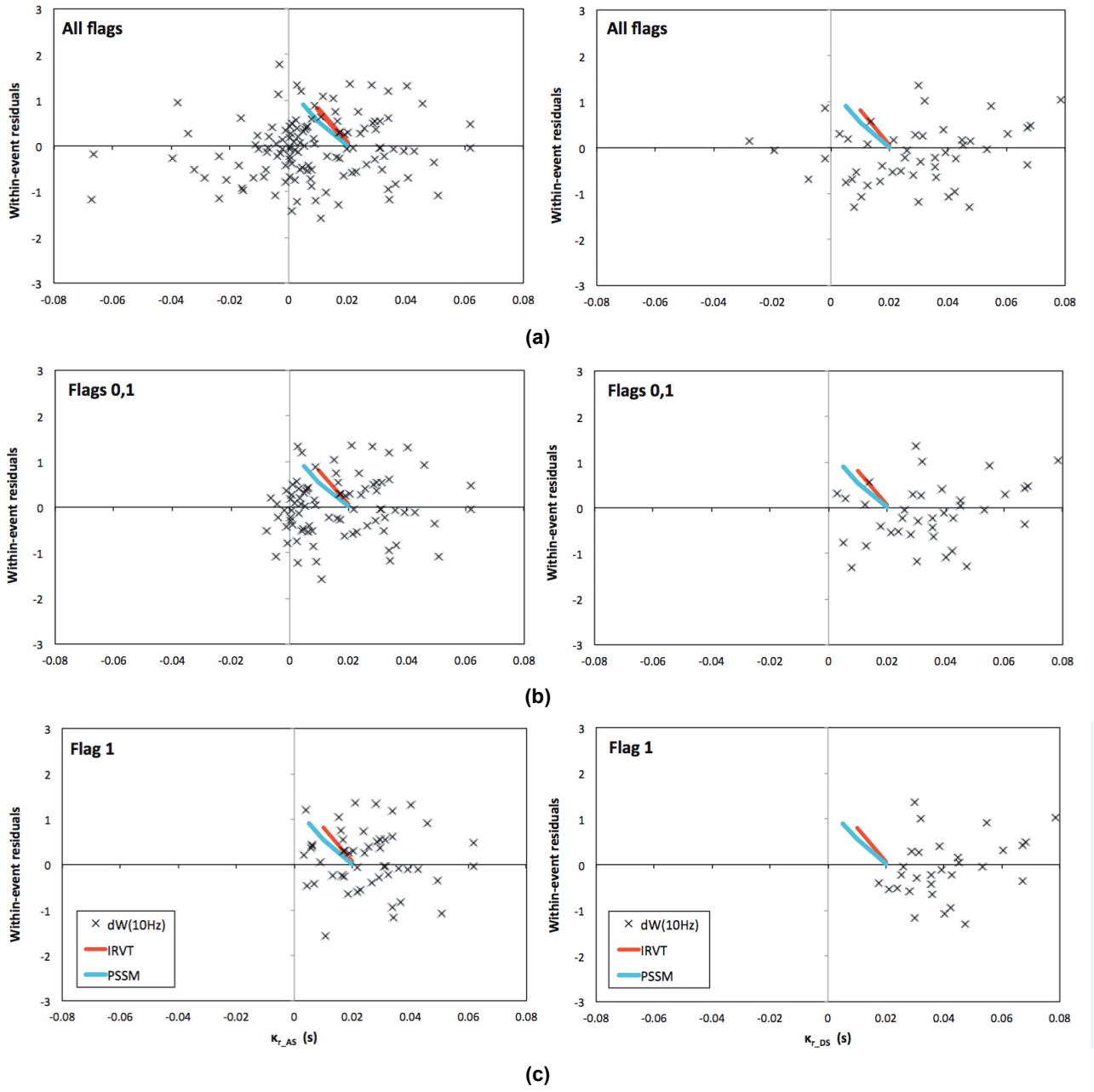

Figure 4.6 **Within-event residuals at 10 Hz for the PEER model [2015] versus measured κ_{r_AS} values (left) and κ_{r_DS} values (right) for: (a) all recordings; (b) recordings without significant up-going trend in their FAS; and (c) recordings with clear down-going trend in their FAS. The blue and red lines show the theoretical scaling predicted from the PSSM and IRVT.**

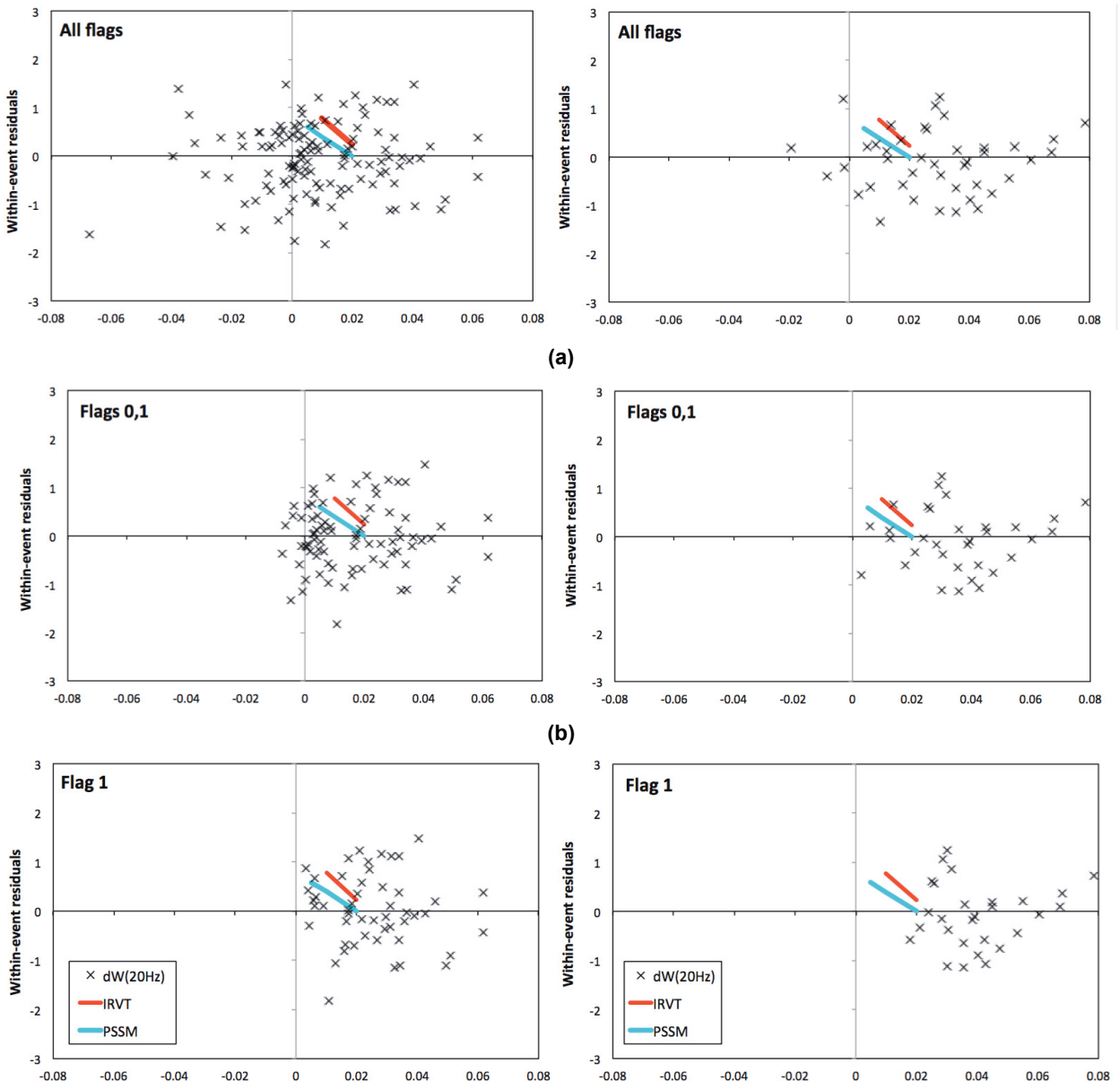

Figure 4.7 **<u>Within-event</u> residuals at <u>20 Hz</u> for the PEER model [2015] versus measured κ_{r_AS} values (left) and κ_{r_DS} values (right) for: (a) all recordings; (b) recordings without significant up-going trend in their FAS; and (c) recordings with clear down-going trend in their FAS. The blue and red lines show the theoretical scaling predicted from the PSSM and IRVT.**

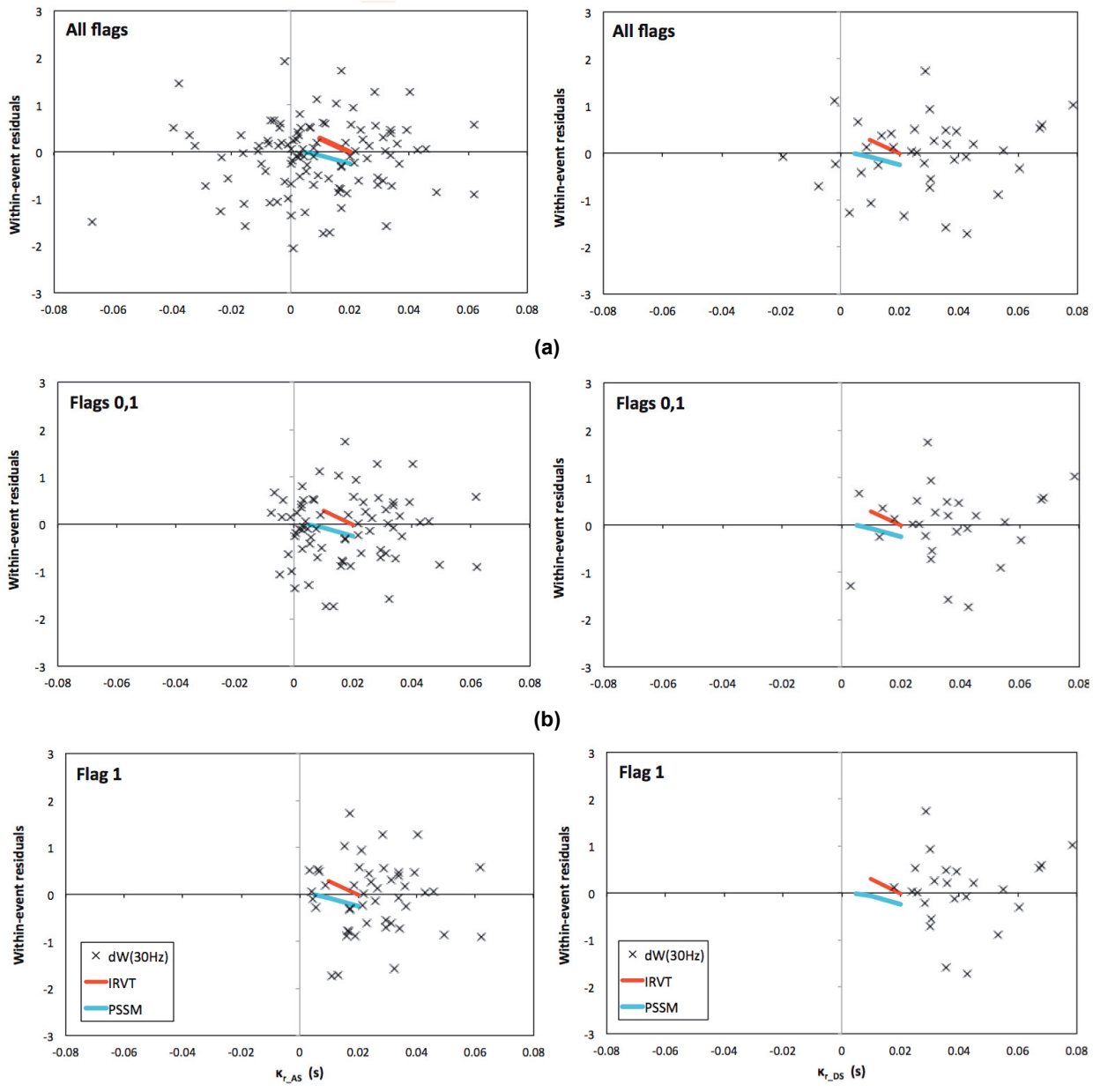

Figure 4.8 **Within-event residuals at 30 Hz for the PEER [2015] model versus measured κ_{r_AS} values (left) and κ_{r_DS} values (right) for: (a) all recordings; (b) recordings without significant up-going trend in their FAS; and (c) recordings with clear down-going trend in their FAS. The blue and red lines show the theoretical scaling predicted from the PSSM and IRVT.**

4.4 EMPIRICALLY-BASED V_S-κ FACTORS FOR HARD-ROCK SITES

Given that the residuals do not show a strong trend with κ, an alternative approach is used to develop the combined effect of V_s and κ for hard-rock sites relative to a reference-site condition. A V_{s30} of 760 m/sec is used as the reference-site condition because it is the upper range of V_{s30} values for which there is still adequate empirical data to reliably constrain the V_{s30} scaling in the GMPEs.

The mean total residual at each spectral frequency is computed giving equal weight to each recording. These mean residuals show the misfit in the ground motion if the site amplification (with respect to 760 m/sec) is assumed to be unity. Therefore, the mean residuals represent the empirical estimate of the combined V_s-κ_0 site factor relative to a 760 m/sec reference-site condition.

The mean residuals for the two subsets of the NGA-East (showing the difference between hard-rock sites and soft-rock sites) are shown in Figure 4.9a, and are not significantly different for recordings out to 50 km and 100 km. The empirical results are compared with results from analytical modeling in Figure 4.9b, and they are derived from simulations with the point-source stochastic model and adjustments with the inverse RVT approach. At low frequencies (<3 Hz), the residuals are in the 0.6–0.9 range, which is consistent with the scaling for the change in the impedance contrast. At high frequencies (>10 Hz), the residuals from the NGA-East data do not show the strong increase in the site factors as seen in the analytical model results.

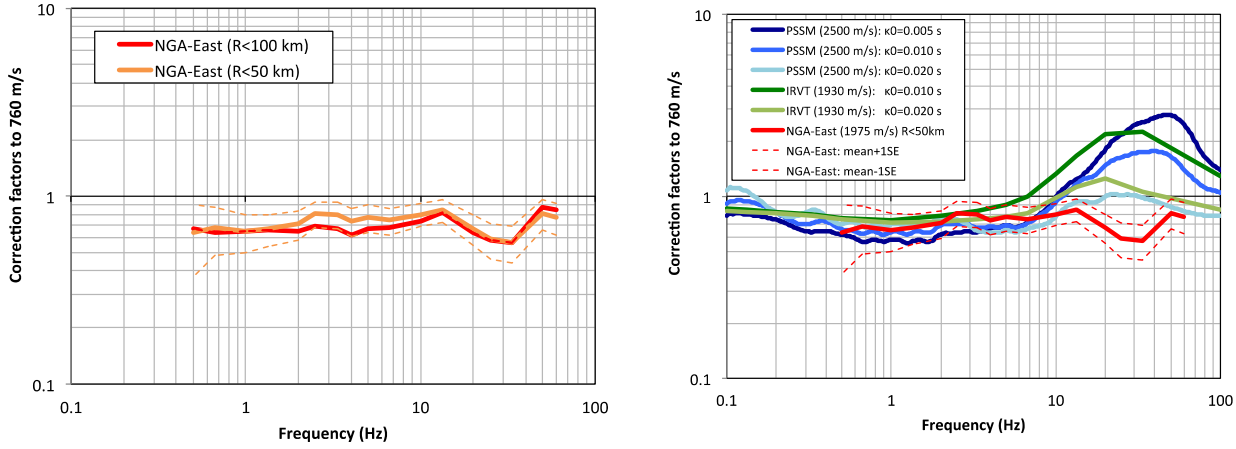

Figure 4.9 **(a) Soft-rock to hard-rock empirical amplification factors on PSA using the NGA-East dataset, for magnitudes M3 and above, for sites in NEHRP class A (V_{s30} ≥ 1500 m/sec), and for distances out to 50 km (orange) and 100 km (red). Dashed lines indicate the standard error; and (b) soft-rock to hard-rock empirical amplification factors for distances out to 50 km compared with theoretical factors computed using the PSSM and the IRVT approaches.**

4.5 OTHER EMPIRICAL STUDIES

The study by Laurendeau et al. [2013] shows the V_{s30} scaling from 550 m/sec to 1100 m/sec from Japanese surface rock stations. Our evaluation of V_s-κ_0 scaling using the NGA-East data was for the scaling from V_{s30} = 760 m/sec to hard-rock sites (V_{s30} > 1500 m/sec). Because the V_{s30} scaling is often assumed to be linear in the log V_{s30} ratio, we assumed that the scaling from 550 to 1100 m/sec given by Laurendeau et al. [2013] is equal to the factor from 760 m/sec to 1520 m/sec (e.g., the factor is for a doubling of the V_{s30} value). With this assumption, we compared the scaling from Laurendeau et al. [2013] with the residuals from the NGA-East dataset, as shown in Figure 4.10. The V_s-κ_0 scaling from Laurendeau et al. [2013] is stronger than seen in the NGA-East residuals, and the factors at high frequencies are consistent with the analytical results for κ_0 = 0.020–0.025 sec.

Laurendeau et al. [2013] also included κ_0 scaling in their GMPE, but the values of κ_0 are estimated from the spectral shape (frequency at which the PSA/PGA = 1.5) and not from the slope of the FAS. This method for calculating a conservative estimate of κ_0 scaling was developed as part of the swissnuclear [2012] κ studies. It is conservative because it assumes that increased high-frequency content is due to only to κ_0. Any resonances at short periods, which reflect V_s scaling and not κ_0 scaling, are interpreted as κ_0 scaling.

The second dataset is from British Columbia, Canada. This dataset consists of hard-rock recordings from small earthquakes in B.C. for a total of 257 recordings with V_{s30} > 1500 m/sec within 100 km in the magnitude range of **M**2.0–**M**4.6. Within 50 km, the number of recordings drops to 142. A GMPE was not developed directly for this dataset. Instead, the CY14 California model was used to compute the residuals with respect to a reference soft-rock site condition (V_{s30} = 760 m/sec). Therefore, the residuals represent the scaling from California soft-rock sites to BC hard-rock sites. The mean residuals are shown in Figure 4.11. The BC hard-rock residuals show an increase in the 15–50 Hz range that is consistent with the analytical κ_0 scaling for a hard-rock κ_0 of about 0.015 sec.

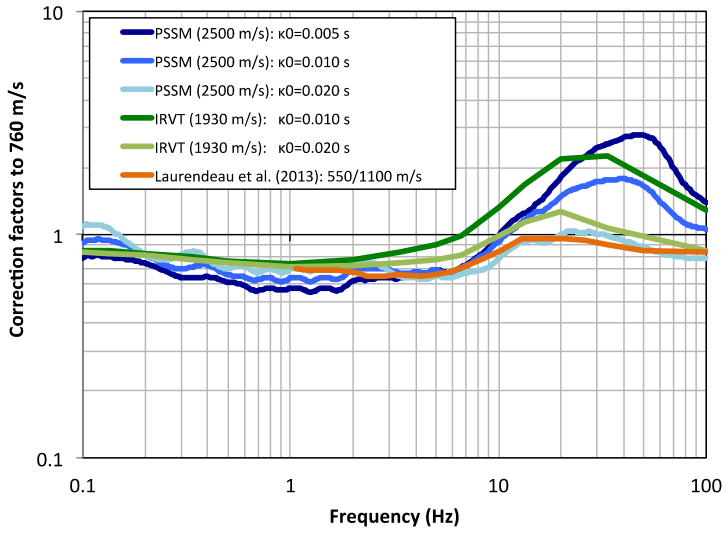

Figure 4.10 **Amplification factors on PSA by Laurendeau et al. [2013] from 550 to 1100 m/sec. Comparison with theoretical factors computed using the PSSM and the IRSV approaches.**

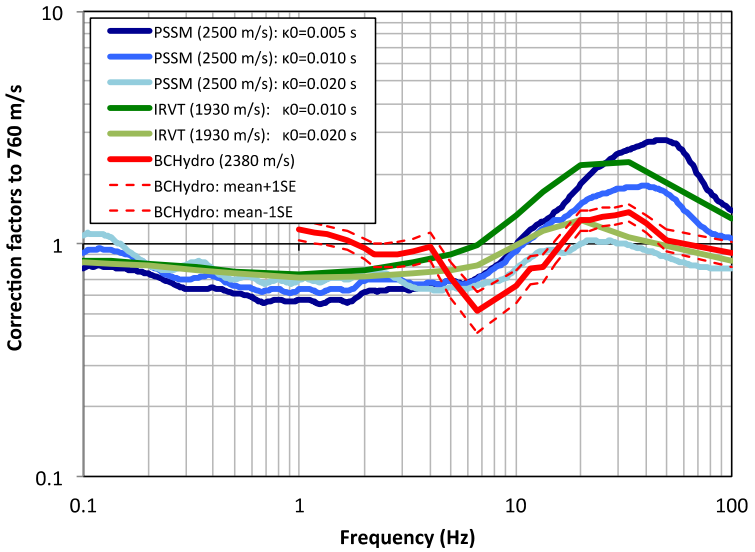

Figure 4.11 **Soft-rock to hard-rock amplification factors on PSA using the BCHydro dataset, for magnitudes M3 and above, for sites in NEHRP class A (V_{s30} ≥ 1500 m/sec), and for distances out to 50 km. Dashed lines indicate the standard error. Comparison with theoretical factors computed using the PSSM and the IRSV approaches.**

4.6 VARIABILITY OF PSA FOR HARD-ROCK SITES

The variability of the PSA residuals can also be used to evaluate the κ_0 scaling for hard-rock sites from analytical modeling. We divided the entire dataset into two groups of sites, namely hard rock (V_{s30} >1500 m/sec) and soil and soft rock (V_{s30} < 1500 m/sec). For each group, we looked at data in two magnitude ranges (**M**3–**M**4 and **M**4–**M**5) and two distance ranges (out to 50 km and out to 100 km). We computed the standard deviation of the total residuals (see previous section) for each of the subsets, but only at frequencies where more than 20 recordings are available. The standard deviation between the hard-rock sites and non-hard-rock sites for the magnitude and distance ranges mentioned above is shown in Figure 4.12. The limited magnitude ranges are intended to minimize changes in the high-frequency spectral shape expected from the magnitude scaling.

The scatter in existing κ_0 values found in literature is disproportionately large compared to the observed variability in ground motion. Simply propagating a typical value of scatter found in κ_0 (e.g., from empirical κ_0-V_{s30} correlations found in Ktenidou et al. [2014]) into ground-motion models, using the κ_0 correction process given for GMPE adjustments in Al Atik et al. [2014], would lead to a standard deviation in spectral acceleration at 20 Hz of 0.9 natural log units just due to κ_0 variability. We compared this to the observed variability in in our residuals. In Figure 4.12, for the case of **M**3–**M**4 and R < 50 km, we observed an increase in the standard deviation (up to 0.2) of the hard-rock sites relative to the other sites above 10 Hz. The commonly used approach of independently combining the κ_0 uncertainty with the GMPE variability corresponds to adding the variances. For the data points in Figure 4.12, this would result in a total standard deviation of 1.2, which is much higher than the standard deviation observed for hard rock (0.8–1.0 above 10 Hz). Therefore, this observation is in line with hard-rock sites being

more variable at high frequencies due to the additional κ_0 variability; however, this additional variability is less than the apparent variability predicted by κ_0-V_{s30} correlations. This is consistent with weaker κ_0 scaling compared to that predicted by the analytical modeling.

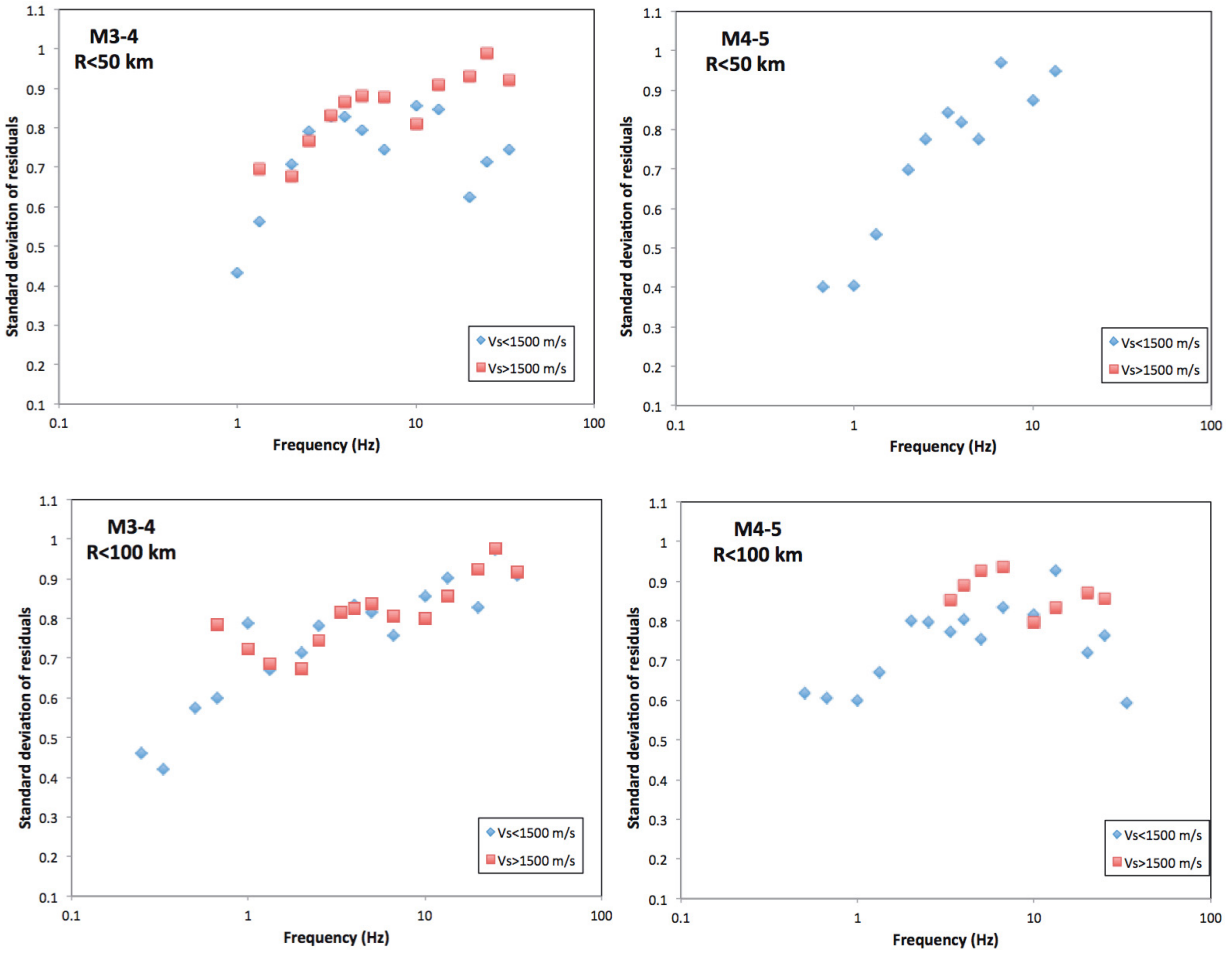

Figure 4.12 **Standard deviation of total residuals for NGA-East data versus frequency, for magnitude ranges M3–M4 and M4–M5, and distance ranges out to 50 and 100 km. The plots compare variability between hard-rock sites (V_{s30} > 1500 m/sec) and soil and soft-rock sites (V_{s30} < 1500 m/sec). Data points shown only for frequencies for which more than 20 recordings are available.**

5 Moving Forward

Although the number of empirical hard-rock observations at short distances is limited to about 100 recordings, the analysis of residuals in Chapter 4 shows that there is a potential inconsistency between the strong κ_0 scaling of high-frequency response spectral values from the analytical modeling and weak κ_0 scaling in the empirical observations.

Overall, the key issue is the consistent treatment of aleatory variability and epistemic uncertainty between GMPEs and site-specific site response, which will control hazard. For κ_0 scaling, how much of the aleatory variability and epistemic uncertainty in κ_0 is captured in the GMPEs and what needs to be included in the site-specific hazard analysis? The objective is to capture the full aleatory variability and epistemic uncertainty, but without double counting. The results in Chapter 4 suggest that there is double-counting of epistemic uncertainty in the median κ_0 scale factors due to correlations in the data—such as correlations between site amplification and the estimated κ—that were not considered in the model development.

To address the inconsistencies between the κ_0 scale factors for the analytical modeling and the empirical observations, we recommend that the tasks listed in Table 5.1 be conducted as part of a two-year κ study.

Table 5.1 Proposed tasks for future research on κ.

	Task	Use of Results
	1 Empirical data for κ_0 scale factors	
1.1	Evaluate basis for κ_0 scale factors in the EPRI (1995) study using the original dataset	Provides a check (understanding) of what the data available in 1995 showed.
1.2	Add additional hard-rock data from global datasets	Improves reliability of κ_0 scale factors
1.3	Add down-hole data (hard-rock at depth)	Using data at depth may greatly increase the number of hard-rock recordings
1.4	Evaluate methods to expand useable frequency range for κ_0	Using a broader frequency band provides more stable estimates of κ_0
	2 Site characterization	
2.1	Conduct site characterization for hard-rock sites for both shallow and deep parts of the profiles (not just the V_{s30})	Provides more accurate V_s profiles that can be used to constrain the site-specific crustal amplification for hard-rock sites
2.2	Evaluate uncertainty of V_s profiles estimated for hard-rock sites	Estimating epistemic uncertainty of the crustal amplification to be sure full range is captured (expected to be larger than soil)
	3. Estimation of site κ_0	
3.1	Evaluate correlation of κ_0 with deep geologic structure	Provides a methodology to regionalize κ_0 based on the geologic maps
3.2	Evaluate methods for estimation of κ_0 using coda waves	May provide a more robust estimate of κ_0 because the coda waves capture average effects over a range of directions
3.3	Use improved site characterization (V_s profile) to estimate amplification and the resulting κ_0	Reduce trade-offs between damping (κ_0) and the site-specific crustal amplification (impedance contrast effects)
3.4	Estimate κ_0 for vertical component (gets into the bigger issue of site amplification for vertical)	Constrain V/H ratios for rock sites
	4. Correlation of κ_0 and V_{s30} effects	
4.1	Evaluate how much κ_0 scaling is captured in the V_{s30} scaling	Avoid double counting or under-estimating epistemic uncertainty in site-specific site amplification
4.2	Estimate aleatory standard deviations for rock and hard-rock sites (correlation effects show up in standard deviations)	Use to check that the combined κ_0 scale factors and κ_0 variability for given V_{s30} is consistent with observed standard deviation on hard-rock sites

REFERENCES

Abrahamson, N. A., and W. J. Silva (2008). Summary of the Abrahamson & Silva NGA Ground-Motion Relations, *Earthq. Spectra*, 24(1): 67–97.

Aki K. (1967). Scaling law of seismic spectrum, *J. Geophys. Res.,* 72: 1217–1231.

Alatik, L., Kottke, A., Abrahamson, N., and Hollenback, J. (2014). Kappa correction of ground motion prediction equations using inverse random vibration theory approach, *Bull. Seismol. Soc. Am*. 104, 336-346.

Ancheta T.D., Darragh R.B., Stewart J.P., Seyhan E., Silva W.J., Chiou B.-S.J., Wooddell K.E., Graves R.W., Kottke A.R., Boore D.M., Kishida T., Donahue J.L. (2014). NGA-West2 database, *Earthq. Spectra*, 30(3): 989–1005.

Anderson J.G. (1991). A preliminary descriptive model for the distance dependence of the spectral decay parameter in Southern California, *Bull. Seismol. Soc. Am*., 81: 2186–2193.

Anderson J.G. (2013). *Personal communication*.

Anderson J.G., Hough S.E. (1984). A model for the shape of the Fourier amplitude spectrum of acceleration at high frequencies, *Bull. Seismol. Soc. Am*., 74(5): 1969–1993.

Anderson J.G., Humphrey J.R. (1991). A least squares method for objective determination of earthquake source parameters, *Seismol. Res. Letts.*, 62, 201–209.

Atkinson G.M., Boore D.M. (2006). Earthquake ground-motion prediction equations for eastern North America, *Bull. Seismol. Soc. Am*., 96: 2181–2205.

Atkinson G.M. (1984). Attenuation of strong ground motion in Canada from a random vibrations approach, *Bull. Seismol. Soc. Am*., 74(6): 2629–2653.

Atkinson G.M. (1996). The high-frequency shape of the source spectrum for earthquake in Eastern and Western Canada, *Bull. Seismol. Soc. Am.,* 86(1A): 106–112.

Atkinson G.C. (2004). Empirical attenuation of ground-motion spectral amplitudes in Southeastern Canada and the Northeastern United States, *Bull. Seismol. Soc. Am*., 94(3): 1079–1095.

Atkinson G.M, Boore D.M. (2014). The attenuation of Fourier amplitudes for rock sites in eastern North America, *Bull. Seismol. Soc. Am*., 104: 513–528.

Atkinson G.M., Silva W.J. (2000). Stochastic modeling of California ground motions, *Bull. Seismol. Soc. Am*., 90: 255–274.

Baltay A., Hanks T.C. (2013). *Personal communication*.

Beresnev I.A., Atkinson G.M. (1997). Shear-wave velocity survey of seismographic sites in eastern Canada: calibration of empirical regression method of estimating site response, *Seismol. Res. Letts*., 68: 981–987.

Biasi G.P. (2012). *Personal communication*.

Biasi G.P. (2013). *Personal communication.*

Biasi G.P., Smith K.D. (2001). Site effects for seismic monitoring stations in the vicinity of Yucca Mountain, Nevada, *MOL 20011204.0045*, A report prepared for the US DOE/University and Community College System of Nevada Cooperative Agreement.

Biro Y., Renault P. (2012). Importance and impact of host-to-target conversions for ground motion prediction equations in PSHA, *Proceedings,* 15th World Conference of Earthquake Engineering, Lisbon, Portugal.

Boatwright J. (2014). Regional spectral analysis of moderate earthquakes in northeastern North America, NGA-East Working Meeting on Regionalization, January 27, 2014, Pacific Earthquake Engineering Research Center, Berkeley, CA.

Boore D.M. (1983). Stochastic simulation of high-frequency ground motions based on seismological models of the radiated spectra, *Bull. Seismol. Soc. Am*., 73(6): 1865-1894.

Boore D.M. (2003). Simulation of ground motion using the stochastic method, *Pure Appl. Geoph*., 160: 635–676.

Boore D.M. (2009). Comparing stochastic point-source and finite-source ground-motion simulations: SMSIM and EXSIM, *Bull. Seismol. Soc. Am*., 99: 3202–3216.

Boore D.M. (2012). Updated determination of stress parameters for nine well-recorded earthquakes in eastern North America, *Seismol. Res. Letts*., 83: 190–199.

Boore D.M. (2013). The uses and limitations of the square-root impedance method for computing site amplification, *Bull. Seismol. Soc. Am*., 103: 2356–2368.

Boore D.M., Atkinson G. M. (1987). Point-source prediction of ground motion and spectral response parameters at hard-rock sites in eastern North America, *Bull. Seismol. Soc. Am*., 77(2): 440–467.

Boore, D.M., Campbell K.W., Atkinson G.M. (2010). Determination of stress parameters for eight well-recorded earthquakes in eastern North America, *Bull. Seismol. Soc. Am*., 100: 1632–1645.

Boore D.M., Joyner W. (1997). Site amplifications for generic rock sites, *Bull. Seismol. Soc. Am*., 87(2): 327–341.

Bora S. (2015). *Personal communication.*

Brune J. N. (1970). Tectonic stress and the spectra of seismic shear waves from earthquakes, *J. Geophys Res*., 75: 4997–5002.

Brune J.N. (1971). Correction: Tectonic stress and the spectra of seismic shear waves from earthquakes, *J. Geophys. Res*., 76: 5002.

Campbell K.W. (2003). Prediction of strong ground motion using the hybrid empirical method and its use in the development of ground-motion (attenuation) relations in eastern North America, *Bull. Seismol. Soc. Am*., 93, 1012–1033.

Campbell K.W. (2004). Erratum: Prediction of strong ground motion using the hybrid empirical method and its use in the development of ground-motion (attenuation) relations in eastern North America, *Bull. Seismol. Soc. Am*., 94: 2418.

Campbell K.W. (2009). Estimates of shear-wave Q and κ0 for unconsolidated and semiconsolidated sediments in eastern North America, *Bull. Seismol. Soc. Am*., 99: 2365–2392.

Campbell K.W., Hashash Y.M.A., Kim B., Kottke A.R., Rathje E.M., Silva W.J., Stewart J.P. (2014). Reference-rock site conditions for Central and Eastern North America: Part II - Attenuation (kappa) definition, *PEER Report No. 2014/12,* Pacific Earthquake Engineering Research Center, Berkeley, CA.

Chapman M.C., Talwani P., Cannon R.C. (2003). Ground-motion attenuation in the Atlantic Coastal Plain near Charleston, South Carolina, *Bull Seismol. Soc. Am*., 93(3): 998–1011.

Cotton F., Scherbaum F., Bommer J.J., Bungum H. (2006). Criteria for selecting and adjusting ground-motion models for specific target regions: Application to Central Europe and rock sites, *J. Seismol*., 10: 137–156.

Darragh R.B. (2015). *Personal communication*.

Darragh R.B., Green, R.K., Turcott F.T. (1989). Special characteristics of small magnitude earthquakes with application to Western and Eastern North American tectonic environments: Surface motions and depth effects, *Miscellaneous Paper G1-89-16*, U.S. Army Corps of Engineers, Waterways Experiment Station, Vicksburg, MI.

Douglas J., Bungum, H., Scherbaum, F. (2006), Ground motion prediction equations for southern Spain and southern Norway obtained using the composite model perspective, *J. Earthq. Eng*., 10: 33–72.

Douglas J., Gehl P., Bonilla L.F., Gélis C. (2010). A κ model for mainland France, *Pure Appl. Geophys*., 167: 1303–1315.

Dreiling J., Isken M.P., Mooney W.D., Chapman M.C., Godbee R.W. (2014). NGA-East regionalization report: Comparison of four crustal regions within Central and Eastern North America using waveform modeling and 5%-damped pseudo-spectral acceleration response, *PEER Report No. 2014/15*, Pacific Earthquake Engineering Research Center, Berkeley, CA.

Edwards B., Faeh D., Giardini D. (2011). Attenuation of seismic shear wave energy in Switzerland, *Geophys. J. Int*., 185: 967–984.

Edwards B., Ktenidou O.-J., Cotton F., Fäh D., Van Houtte C., Abrahamson N.A. (2015). Near-surface attenuation (Kappa0) determination at hard-rock sites in Switzerland, *Geoph. J. Int.,* doi: 10.1093/gji/ggv222.

EPRI (1993). Guidelines for determining design basis ground motions, Electric Power Research Institute, Vol. 1-5, *EPRI TR-102293*, Palo Alto, CA.

EPRI (2013). Seismic evaluation guidance: Screening, prioritization, and implementation details (SPID) for the resolution of Fukushima near-term task for recommendation 2.1 Seismic, Electric Power Research Institute, Palo Alto, CA.

Gentili S., Franceschina G. (2011). High frequency attenuation of shear waves in the southeastern Alps and northern Dinarides, *Geophys. J. Int*., 185: 1393–1416.

Graves R.W., Pitarka A. (2010). Broadband ground-motion simulation using a hybrid approach, *Bull. Seismol. Soc. Am.*, 100: 2095–2123.

Goulet C.A., Kishida T. Ancheta T.D., Cramer C.H., Darragh R.B., Silva W.J., Hashash Y.M.A., Harmon J., Stewart J.P., Wooddell K.E., Youngs R.R. (2014). PEER NGA-East database, *PEER Report No. 2014/17*. Pacific Earthquake Engineering Research Center, Berkeley, CA.

Hanks T. C. (1982). f max, *Bull. Seismol. Soc. Am*., 72: 1867–1879.

Hiemer S., Scherbaum F., Roessler D., Kuehn N. (2011). Determination of τ0 and rock site κ from recordings of the 2008/2009 earthquake swarm in western Bohemia, *Seismol. Res. Letts*., 82: 387–393.

Hollenback J. (2015). *Personal communication*.

Hough S.E., Anderson J.G. (1988). High-frequency spectra observed at Azna, California: Implications for Q structure, *Bull. Seismol. Soc. Am*., 78: 692–707.

Humphrey J.R., Anderson J.G. (1992). Shear wave attenuation and site response in Guerrero, Mexico, *Bull. Seism. Soc. Am*., 81: 1622–1645.

Kilb D., Biasi G., Anderson J.G., Brune J., Peng Z., Vernon F.L. (2012). A comparison of spectral parameter kappa from small and moderate earthquakes using Southern California ANZA seismic network data, *Bull. Seismol. Soc. Am*., 102: 284–300.

Ktenidou O.-J., Abrahamson N.A., Drouet S., Cotton F. (2015). Understanding the physics of kappa (κ): Insights from a downhole array, *Geoph. J. Int*., doi: 10.1093/gji/ggv315.

Ktenidou O.-J., Cotton F., Abrahamson N.A., Anderson J.G. (2014). Taxonomy of κ: a review of definitions and estimation approaches targeted to applications, *Seismol. Res. Letts*., 85 (1): 135–146.

Ktenidou O.-J., Gélis C., Bonilla L.F. (2013). A study on the variability of κ in a borehole: implications of the computation process, *Bull. Seismol. Soc. Am*., 103(2A): 1048–1068.

Kishida T., Kayen R., Ktenidou O.-J., Silva W.J., Darragh R.B., Watson-Lamprey J. (2014). PEER Arizona strong-motion database and GMPEs evaluation, *PEER Report No. 2014/09*, Pacific Earthquake Engineering Research Center, Berkeley, CA.

Laurendeau A., Cotton F., Ktenidou O.-J., Bonilla L.F., Hollender F. (2013). Rock and stiff-soil site amplification: Dependencies on Vs30 and kappa (κ0), *Bull. Seismol. Soc. Am*., 103: 3131–3148.

Lermo J., Chavez-Garcia F.J. (1993). Site effect evaluation using spectral ratios with only one station, *Bull. Seismol. Soc. Am*., 83(5): 1574–1594.

Mai P.M., Imperatori W., Olsen K.B. (2010). Hybrid broadband ground-motion simulations: Combining long-period deterministic synthetics with high-frequency multiple S-to-S backscattering, *Bull. Seismol. Soc. Am*., 100(5A): 2124–2142.

Muto M., Duron Z. (2015). High-frequency seismic hazard estimation and impact on seismic evaluation for dams, *Proceedings*, SSA Annual Meeting, Pasadena, CA.

Nava F.A., García R., Castro R.R., Suárez C., Márquez B., Núñez-Cornú F., Saavedra G., Toscano R. (1999). S wave attenuation in the coastal region of Jalisco-Colima, Mexico, *Phys. Earth Planet. Inter.*, 115: 247–257.

Parolai S., Bindi D. (2004). Influence of soil-layer properties on k evaluation, *Bull. Seismol. Soc. Am*., 94: 349–356.

PEER (2015). NGA-East: median ground-motion models for the Central and Eastern North America Region, *PEER Report No. 2015/04*, Pacific Earthquake Engineering Research Center, University of California, Berkeley, CA.

Press W.H., Flannery B.P., Teukolsky S.A., Vetterling W.T. (1986). *Numerical Recipes*, Cambridge University Press, Cambridge, UK.

Purvance M.D., Anderson J.G. (2003). A comprehensive study of the observed spectral decay in strong-motion accelerations recorded in Guerrero, Mexico, *Bull. Seismol. Soc. Am*., 93: 600–611.

Scherbaum F. (1990). Combined inversion for the three-dimensional Q structure and source parameters using microearthquake spectra, *J. Geophys. Res*., 95: 12423–12438.

Schneider J.F., Silva W.J., Stark C.L. (1993). Ground motion model for the M6.9 1989 Loma Prieta earthquake including effects of source, path and site, *Earthq. Spectra*, 9: 251–287.

Silva W.J. (1991). Global characteristics and site geometry. Chapter 6, *Proceedings: NSF/EPRI Workshop on Dynamic Soil Properties and Site Characterization*, Electric Power Research Institute, NP-7337, Palo Alto, CA.

Silva W.J. (2013). *Personal communication.*

Silva W.J., Abrahamson N.A., Toro G., Costantino C. (1997). Description and validation of the stochastic ground motion model, Report Submitted to Brookhaven National Laboratory, *Contract No. 770573*, Associated Universities, Inc. Upton, NY.

Silva W.J., Darragh R.B. (1995). Engineering characterization of earthquake strong ground motion recorded at rock sites, Electric Power Research Institute, *TR-102261*, Palo Alto, CA.

Silva W.J., Darragh R.B., Gregor N., Martin G., Abrahamson N.A., Kircher C. (1998). Reassessment of site coefficients and near-fault factors for building code provisions, *Technical Report Program Element II: 98-HQGR-1010*, Pacific Engineering and Analysis, El Cerrito, CA.

Silva W.J., Green R.K. (1989). Magnitude and distance scaling of response spectral shapes for rock sites with applications to North American tectonic environment, *Earthq. Spectra*, 5(3): 591-624.

Silva W.J., Lee K. (1987). WES RASCAL code for synthesizing earthquake ground motions. state-of-the-art for Assessing Earthquake Hazards in the United States, *Report 24*, *Misc. Paper S-73-1*, U.S. Army Engineers Waterways Experiment Station, Vicksburg, MS.

swissnuclear (2012). Summary of updated kappa-fpeak relationships, unpublished report, *EXT-SUP-1044*, rev1_AlAtik_11-10-2011-6.

Toro G.R., McGuire R.K. (1987). An investigation into earthquake ground motion characteristics in eastern North America, *Bull. Seismol. Soc. Am*., 77(2): 468–489.

Tsai C.-C.P., Chen K.-C. (2000). A model for the high-cut process of strong motion accelerations in terms of distance, magnitude, and site condition: an example from the SMART 1 array, Lotung, Taiwan, *Bull. Seismol. Soc. Am.*, 90: 1535–1542.

Van Houtte, C., Drouet, S. and Cotton, F. (2011). Analysis of the origins of κ (kappa) to compute hard rock to rock adjustment factors for GMPEs, *Bull. Seism. Soc. Am*. 101, 2926–2941

Van Houtte C., Ktenidou O.-J., Larkin T. (2013). Near-source kappa estimates from the Canterbury earthquake sequence, New Zealand, SSA Annual Meeting, Salt Lake City, 17–19 April (presentation).

Van Houtte C., Ktenidou O.-J., Larkin T., Holden C. (2014). Hard-site κ0 (kappa) calculations for Christchurch, New Zealand, and comparison with local ground motion prediction models, *Bull. Seismol. Soc. Am*., 104(4): 1899–1913.

PEER REPORTS

PEER reports are available as a free PDF download from http://peer.berkeley.edu/publications/peer_reports_complete.html. Printed hard copies of PEER reports can be ordered directly from our printer by following the instructions at http://peer.berkeley.edu/publications/peer_reports.html. For other related questions about the PEER Report Series, contact the Pacific Earthquake Engineering Research Center, 325 Davis Hall Mail Code 1792, Berkeley, CA 94720. Tel.: (510) 642-3437; Fax: (510) 642-1655; Email: clairejohnson@berkeley.edu.

PEER 2016/01 *A Methodology for the Estimation of Kappa (κ) from Large Datasets: Example Application to Rock Sites in the NGA-East Database and Implications on Design Motions.* Olga-Joan Ktenidou, Norman A. Abrahamson, Robert B. Darragh, and Walter J. Silva. April 2016.

PEER 2015/13 *Self-Centering Precast Concrete Dual-Steel-Shell Columns for Accelerated Bridge Construction: Seismic Performance, Analysis, and Design*. Gabriele Guerrini, José I. Restrepo, Athanassios Vervelidis, and Milena Massari. December 2015.

PEER 2015/12 *Shear-Flexure Interaction Modeling for Reinforced Concrete Structural Walls and Columns under Reversed Cyclic Loading*. Kristijan Kolozvari, Kutay Orakcal, and John Wallace. December 2015.

PEER 2015/11 *Selection and Scaling of Ground Motions for Nonlinear Response History Analysis of Buildings in Performance-Based Earthquake Engineering*. N. Simon Kwong and Anil K. Chopra. December 2015.

PEER 2015/10 *Structural Behavior of Column-Bent Cap Beam-Box Girder Systems in Reinforced Concrete Bridges Subjected to Gravity and Seismic Loads. Part II: Hybrid Simulation and Post-Test Analysis*. Mohamed A. Moustafa and Khalid M. Mosalam. November 2015.

PEER 2015/09 *Structural Behavior of Column-Bent Cap Beam-Box Girder Systems in Reinforced Concrete Bridges Subjected to Gravity and Seismic Loads. Part I: Pre-Test Analysis and Quasi-Static Experiments*. Mohamed A. Moustafa and Khalid M. Mosalam. September 2015.

PEER 2015/08 *NGA-East: Adjustments to Median Ground-Motion Models for Center and Eastern North America*. August 2015.

PEER 2015/07 *NGA-East: Ground-Motion Standard-Deviation Models for Central and Eastern North America*. Linda Al Atik. June 2015.

PEER 2015/06 *Adjusting Ground-Motion Intensity Measures to a Reference Site for which V_{S30} = 3000 m/sec*. David M. Boore. May 2015.

PEER 2015/05 *Hybrid Simulation of Seismic Isolation Systems Applied to an APR-1400 Nuclear Power Plant.* Andreas H. Schellenberg, Alireza Sarebanha, Matthew J. Schoettler, Gilberto Mosqueda, Gianmario Benzoni, and Stephen A. Mahin. April 2015.

PEER 2015/04 *NGA-East: Median Ground-Motion Models for the Central and Eastern North America Region*. April 2015.

PEER 2015/03 *Single Series Solution for the Rectangular Fiber-Reinforced Elastomeric Isolator Compression Modulus*. James M. Kelly and Niel C. Van Engelen. March 2015.

PEER 2015/02 *A Full-Scale, Single-Column Bridge Bent Tested by Shake-Table Excitation.* Matthew J. Schoettler, José I. Restrepo, Gabriele Guerrini, David E. Duck, and Francesco Carrea. March 2015.

PEER 2015/01 *Concrete Column Blind Prediction Contest 2010: Outcomes and Observations.* Vesna Terzic, Matthew J. Schoettler, José I. Restrepo, and Stephen A Mahin. March 2015.

PEER 2014/20 *Stochastic Modeling and Simulation of Near-Fault Ground Motions for Performance-Based Earthquake Engineering*. Mayssa Dabaghi and Armen Der Kiureghian. December 2014.

PEER 2014/19 *Seismic Response of a Hybrid Fiber-Reinforced Concrete Bridge Column Detailed for Accelerated Bridge Construction*. Wilson Nguyen, William Trono, Marios Panagiotou, and Claudia P. Ostertag. December 2014.

PEER 2014/18 *Three-Dimensional Beam-Truss Model for Reinforced Concrete Walls and Slabs Subjected to Cyclic Static or Dynamic Loading*. Yuan Lu, Marios Panagiotou, and Ioannis Koutromanos. December 2014.

PEER 2014/17 *PEER NGA-East Database*. Christine A. Goulet, Tadahiro Kishida, Timothy D. Ancheta, Chris H. Cramer, Robert B. Darragh, Walter J. Silva, Youssef M.A. Hashash, Joseph Harmon, Jonathan P. Stewart, Katie E. Wooddell, and Robert R. Youngs. October 2014.

PEER 2014/16 *Guidelines for Performing Hazard-Consistent One-Dimensional Ground Response Analysis for Ground Motion Prediction*. Jonathan P. Stewart, Kioumars Afshari, and Youssef M.A. Hashash. October 2014.

PEER 2014/15 *NGA-East Regionalization Report: Comparison of Four Crustal Regions within Central and Eastern North America using Waveform Modeling and 5%-Damped Pseudo-Spectral Acceleration Response*. Jennifer Dreiling, Marius P. Isken, Walter D. Mooney, Martin C. Chapman, and Richard W. Godbee. October 2014.

PEER 2014/14 *Scaling Relations between Seismic Moment and Rupture Area of Earthquakes in Stable Continental Regions*. Paul Somerville. August 2014.

PEER 2014/13 *PEER Preliminary Notes and Observations on the August 24, 2014, South Napa Earthquake*. Grace S. Kang and Stephen A. Mahin, Editors. September 2014.

PEER 2014/12 *Reference-Rock Site Conditions for Central and Eastern North America: Part II – Attenuation (Kappa) Definition*. Kenneth W. Campbell, Youssef M.A. Hashash, Byungmin Kim, Albert R. Kottke, Ellen M. Rathje, Walter J. Silva, and Jonathan P. Stewart. August 2014.

PEER 2014/11 *Reference-Rock Site Conditions for Central and Eastern North America: Part I - Velocity Definition*. Youssef M.A. Hashash, Albert R. Kottke, Jonathan P. Stewart, Kenneth W. Campbell, Byungmin Kim, Ellen M. Rathje, Walter J. Silva, Sissy Nikolaou, and Cheryl Moss. August 2014.

PEER 2014/10 *Evaluation of Collapse and Non-Collapse of Parallel Bridges Affected by Liquefaction and Lateral Spreading*. Benjamin Turner, Scott J. Brandenberg, and Jonathan P. Stewart. August 2014.

PEER 2014/09 *PEER Arizona Strong-Motion Database and GMPEs Evaluation*. Tadahiro Kishida, Robert E. Kayen, Olga-Joan Ktenidou, Walter J. Silva, Robert B. Darragh, and Jennie Watson-Lamprey. June 2014.

PEER 2014/08 *Unbonded Pretensioned Bridge Columns with Rocking Detail*. Jeffrey A. Schaefer, Bryan Kennedy, Marc O. Eberhard, and John F. Stanton. June 2014.

PEER 2014/07 *Northridge 20 Symposium Summary Report: Impacts, Outcomes, and Next Steps*. May 2014.

PEER 2014/06 *Report of the Tenth Planning Meeting of NEES/E-Defense Collaborative Research on Earthquake Engineering*. December 2013.

PEER 2014/05 *Seismic Velocity Site Characterization of Thirty-One Chilean Seismometer Stations by Spectral Analysis of Surface Wave Dispersion*. Robert Kayen, Brad D. Carkin, Skye Corbet, Camilo Pinilla, Allan Ng, Edward Gorbis, and Christine Truong. April 2014.

PEER 2014/04 Effect of Vertical Acceleration on Shear Strength of Reinforced Concrete Columns. Hyerin Lee and Khalid M. Mosalam. April 2014.

PEER 2014/03 *Retest of Thirty-Year-Old Neoprene Isolation Bearings.* James M. Kelly and Niel C. Van Engelen. March 2014.

PEER 2014/02 *Theoretical Development of Hybrid Simulation Applied to Plate Structures.* Ahmed A. Bakhaty, Khalid M. Mosalam, and Sanjay Govindjee. January 2014.

PEER 2014/01 *Performance-Based Seismic Assessment of Skewed Bridges.* Peyman Kaviani, Farzin Zareian, and Ertugrul Taciroglu. January 2014.

PEER 2013/26 *Urban Earthquake Engineerin*g. Proceedings of the U.S.-Iran Seismic Workshop. December 2013.

PEER 2013/25 *Earthquake Engineering for Resilient Communities: 2013 PEER Internship Program Research Report Collection.* Heidi Tremayne (Editor), Stephen A. Mahin (Editor), Jorge Archbold Monterossa, Matt Brosman, Shelly Dean, Katherine deLaveaga, Curtis Fong, Donovan Holder, Rakeeb Khan, Elizabeth Jachens, David Lam, Daniela Martinez Lopez, Mara Minner, Geffen Oren, Julia Pavicic, Melissa Quinonez, Lorena Rodriguez, Sean Salazar, Kelli Slaven, Vivian Steyert, Jenny Taing, and Salvador Tena. December 2013.

PEER 2013/24 *NGA-West2 Ground Motion Prediction Equations for Vertical Ground Motions*. September 2013.

PEER 2013/23 *Coordinated Planning and Preparedness for Fire Following Major Earthquakes*. Charles Scawthorn. November 2013.

PEER 2013/22 *GEM-PEER Task 3 Project: Selection of a Global Set of Ground Motion Prediction Equations.* Jonathan P. Stewart, John Douglas, Mohammad B. Javanbarg, Carola Di Alessandro, Yousef Bozorgnia, Norman A. Abrahamson, David M. Boore, Kenneth W. Campbell, Elise Delavaud, Mustafa Erdik, and Peter J. Stafford. December 2013.

PEER 2013/21 *Seismic Design and Performance of Bridges with Columns on Rocking Foundations*. Grigorios Antonellis and Marios Panagiotou. September 2013.

PEER 2013/20 *Experimental and Analytical Studies on the Seismic Behavior of Conventional and Hybrid Braced Frames*. Jiun-Wei Lai and Stephen A. Mahin. September 2013.

PEER 2013/19 *Toward Resilient Communities: A Performance-Based Engineering Framework for Design and Evaluation of the Built Environment.* Michael William Mieler, Bozidar Stojadinovic, Robert J. Budnitz, Stephen A. Mahin, and Mary C. Comerio. September 2013.

PEER 2013/18 *Identification of Site Parameters that Improve Predictions of Site Amplification*. Ellen M. Rathje and Sara Navidi. July 2013.

PEER 2013/17 *Response Spectrum Analysis of Concrete Gravity Dams Including Dam-Water-Foundation Interaction*. Arnkjell Løkke and Anil K. Chopra. July 2013.

PEER 2013/16 *Effect of Hoop Reinforcement Spacing on the Cyclic Response of Large Reinforced Concrete Special Moment Frame Beams.* Marios Panagiotou, Tea Visnjic, Grigorios Antonellis, Panagiotis Galanis, and Jack P. Moehle. June 2013.

PEER 2013/15 *A Probabilistic Framework to Include the Effects of Near-Fault Directivity in Seismic Hazard Assessment*. Shrey Kumar Shahi, Jack W. Baker. October 2013.

PEER 2013/14 *Hanging-Wall Scaling using Finite-Fault Simulations.* Jennifer L. Donahue and Norman A. Abrahamson. September 2013.

PEER 2013/13 *Semi-Empirical Nonlinear Site Amplification and its Application in NEHRP Site Factors*. Jonathan P. Stewart and Emel Seyhan. November 2013.

PEER 2013/12 *Nonlinear Horizontal Site Response for the NGA-West2 Project.* Ronnie Kamai, Norman A. Abramson, Walter J. Silva. May 2013.

PEER 2013/11 *Epistemic Uncertainty for NGA-West2 Models.* Linda Al Atik and Robert R. Youngs. May 2013.

PEER 2013/10 *NGA-West 2 Models for Ground-Motion Directionality*. Shrey K. Shahi and Jack W. Baker. May 2013.

PEER 2013/09 *Final Report of the NGA-West2 Directivity Working Group.* Paul Spudich, Jeffrey R. Bayless, Jack W. Baker, Brian S.J. Chiou, Badie Rowshandel, Shrey Shahi, and Paul Somerville. May 2013.

PEER 2013/08 *NGA-West2 Model for Estimating Average Horizontal Values of Pseudo-Absolute Spectral Accelerations Generated by Crustal Earthquakes*. I. M. Idriss. May 2013.

PEER 2013/07 *Update of the Chiou and Youngs NGA Ground Motion Model for Average Horizontal Component of Peak Ground Motion and Response Spectra*. Brian Chiou and Robert Youngs. May 2013.

PEER 2013/06 *NGA-West2 Campbell-Bozorgnia Ground Motion Model for the Horizontal Components of PGA, PGV, and 5%-Damped Elastic Pseudo-Acceleration Response Spectra for Periods Ranging from 0.01 to 10 sec.* Kenneth W. Campbell and Yousef Bozorgnia. May 2013.

PEER 2013/05 *NGA-West 2 Equations for Predicting Response Spectral Accelerations for Shallow Crustal Earthquakes*. David M. Boore, Jonathan P. Stewart, Emel Seyhan, and Gail M. Atkinson. May 2013.

PEER 2013/04 *Update of the AS08 Ground-Motion Prediction Equations Based on the NGA-West2 Data Set*. Norman Abrahamson, Walter Silva, and Ronnie Kamai. May 2013.

PEER 2013/03 *PEER NGA-West2 Database.* Timothy D. Ancheta, Robert B. Darragh, Jonathan P. Stewart, Emel Seyhan, Walter J. Silva, Brian S.J. Chiou, Katie E. Wooddell, Robert W. Graves, Albert R. Kottke, David M. Boore, Tadahiro Kishida, and Jennifer L. Donahue. May 2013.

PEER 2013/02 *Hybrid Simulation of the Seismic Response of Squat Reinforced Concrete Shear Walls*. Catherine A. Whyte and Bozidar Stojadinovic. May 2013.

PEER 2013/01 *Housing Recovery in Chile: A Qualitative Mid-program Review*. Mary C. Comerio. February 2013.

PEER 2012/08 *Guidelines for Estimation of Shear Wave Velocity.* Bernard R. Wair, Jason T. DeJong, and Thomas Shantz. December 2012.

PEER 2012/07 *Earthquake Engineering for Resilient Communities: 2012 PEER Internship Program Research Report Collection.* Heidi Tremayne (Editor), Stephen A. Mahin (Editor), Collin Anderson, Dustin Cook, Michael Erceg, Carlos Esparza, Jose Jimenez, Dorian Krausz, Andrew Lo, Stephanie Lopez, Nicole McCurdy, Paul Shipman, Alexander Strum, Eduardo Vega. December 2012.

PEER 2012/06 *Fragilities for Precarious Rocks at Yucca Mountain.* Matthew D. Purvance, Rasool Anooshehpoor, and James N. Brune. December 2012.

PEER 2012/05 *Development of Simplified Analysis Procedure for Piles in Laterally Spreading Layered Soils.* Christopher R. McGann, Pedro Arduino, and Peter Mackenzie–Helnwein. December 2012.

PEER 2012/04 *Unbonded Pre-Tensioned Columns for Bridges in Seismic Regions.* Phillip M. Davis, Todd M. Janes, Marc O. Eberhard, and John F. Stanton. December 2012.

PEER 2012/03 *Experimental and Analytical Studies on Reinforced Concrete Buildings with Seismically Vulnerable Beam-Column Joints*. Sangjoon Park and Khalid M. Mosalam. October 2012.

PEER 2012/02 *Seismic Performance of Reinforced Concrete Bridges Allowed to Uplift during Multi-Directional Excitation*. Andres Oscar Espinoza and Stephen A. Mahin. July 2012.

PEER 2012/01 *Spectral Damping Scaling Factors for Shallow Crustal Earthquakes in Active Tectonic Regions.* Sanaz Rezaeian, Yousef Bozorgnia, I. M. Idriss, Kenneth Campbell, Norman Abrahamson, and Walter Silva. July 2012.

PEER 2011/10 *Earthquake Engineering for Resilient Communities: 2011 PEER Internship Program Research Report Collection*. Heidi Faison and Stephen A. Mahin, Editors. December 2011.

PEER 2011/09 *Calibration of Semi-Stochastic Procedure for Simulating High-Frequency Ground Motions*. Jonathan P. Stewart, Emel Seyhan, and Robert W. Graves. December 2011.

PEER 2011/08 *Water Supply in regard to Fire Following Earthquake*. Charles Scawthorn. November 2011.

PEER 2011/07 *Seismic Risk Management in Urban Areas*. Proceedings of a U.S.-Iran-Turkey Seismic Workshop. September 2011.

PEER 2011/06 *The Use of Base Isolation Systems to Achieve Complex Seismic Performance Objectives*. Troy A. Morgan and Stephen A. Mahin. July 2011.

PEER 2011/05 *Case Studies of the Seismic Performance of Tall Buildings Designed by Alternative Means.* Task 12 Report for the Tall Buildings Initiative. Jack Moehle, Yousef Bozorgnia, Nirmal Jayaram, Pierson Jones, Mohsen Rahnama, Nilesh Shome, Zeynep Tuna, John Wallace, Tony Yang, and Farzin Zareian. July 2011.

PEER 2011/04 *Recommended Design Practice for Pile Foundations in Laterally Spreading Ground.* Scott A. Ashford, Ross W. Boulanger, and Scott J. Brandenberg. June 2011.

PEER 2011/03 *New Ground Motion Selection Procedures and Selected Motions for the PEER Transportation Research Program*. Jack W. Baker, Ting Lin, Shrey K. Shahi, and Nirmal Jayaram. March 2011.

PEER 2011/02 *A Bayesian Network Methodology for Infrastructure Seismic Risk Assessment and Decision Support*. Michelle T. Bensi, Armen Der Kiureghian, and Daniel Straub. March 2011.

PEER 2011/01 *Demand Fragility Surfaces for Bridges in Liquefied and Laterally Spreading Ground.* Scott J. Brandenberg, Jian Zhang, Pirooz Kashighandi, Yili Huo, and Minxing Zhao. March 2011.

PEER 2010/05 *Guidelines for Performance-Based Seismic Design of Tall Buildings.* Developed by the Tall Buildings Initiative. November 2010.

PEER 2010/04 *Application Guide for the Design of Flexible and Rigid Bus Connections between Substation Equipment Subjected to Earthquakes.* Jean-Bernard Dastous and Armen Der Kiureghian. September 2010.

PEER 2010/03 *Shear Wave Velocity as a Statistical Function of Standard Penetration Test Resistance and Vertical Effective Stress at Caltrans Bridge Sites.* Scott J. Brandenberg, Naresh Bellana, and Thomas Shantz. June 2010.

PEER 2010/02 *Stochastic Modeling and Simulation of Ground Motions for Performance-Based Earthquake Engineering.* Sanaz Rezaeian and Armen Der Kiureghian. June 2010.

PEER 2010/01 *Structural Response and Cost Characterization of Bridge Construction Using Seismic Performance Enhancement Strategies.* Ady Aviram, Božidar Stojadinović, Gustavo J. Parra-Montesinos, and Kevin R. Mackie. March 2010.

PEER 2009/03 *The Integration of Experimental and Simulation Data in the Study of Reinforced Concrete Bridge Systems Including Soil-Foundation-Structure Interaction.* Matthew Dryden and Gregory L. Fenves. November 2009.

PEER 2009/02 *Improving Earthquake Mitigation through Innovations and Applications in Seismic Science, Engineering, Communication, and Response*. Proceedings of a U.S.-Iran Seismic Workshop. October 2009.

PEER 2009/01 *Evaluation of Ground Motion Selection and Modification Methods: Predicting Median Interstory Drift Response of Buildings*. Curt B. Haselton, Editor. June 2009.

PEER 2008/10 *Technical Manual for Strata.* Albert R. Kottke and Ellen M. Rathje. February 2009.

PEER 2008/09 *NGA Model for Average Horizontal Component of Peak Ground Motion and Response Spectra.* Brian S.-J. Chiou and Robert R. Youngs. November 2008.

PEER 2008/08 *Toward Earthquake-Resistant Design of Concentrically Braced Steel Structures*. Patxi Uriz and Stephen A. Mahin. November 2008.

PEER 2008/07 *Using OpenSees for Performance-Based Evaluation of Bridges on Liquefiable Soils*. Stephen L. Kramer, Pedro Arduino, and HyungSuk Shin. November 2008.

PEER 2008/06 *Shaking Table Tests and Numerical Investigation of Self-Centering Reinforced Concrete Bridge Columns*. Hyung IL Jeong, Junichi Sakai, and Stephen A. Mahin. September 2008.

PEER 2008/05 *Performance-Based Earthquake Engineering Design Evaluation Procedure for Bridge Foundations Undergoing Liquefaction-Induced Lateral Ground Displacement*. Christian A. Ledezma and Jonathan D. Bray. August 2008.

PEER 2008/04 *Benchmarking of Nonlinear Geotechnical Ground Response Analysis Procedures.* Jonathan P. Stewart, Annie On-Lei Kwok, Yousseff M. A. Hashash, Neven Matasovic, Robert Pyke, Zhiliang Wang, and Zhaohui Yang. August 2008.

PEER 2008/03 *Guidelines for Nonlinear Analysis of Bridge Structures in California.* Ady Aviram, Kevin R. Mackie, and Božidar Stojadinović. August 2008.

PEER 2008/02 *Treatment of Uncertainties in Seismic-Risk Analysis of Transportation Systems*. Evangelos Stergiou and Anne S. Kiremidjian. July 2008.

PEER 2008/01 *Seismic Performance Objectives for Tall Buildings.* William T. Holmes, Charles Kircher, William Petak, and Nabih Youssef. August 2008.

PEER 2007/12 *An Assessment to Benchmark the Seismic Performance of a Code-Conforming Reinforced Concrete Moment-Frame Building.* Curt Haselton, Christine A. Goulet, Judith Mitrani-Reiser, James L. Beck, Gregory G. Deierlein, Keith A. Porter, Jonathan P. Stewart, and Ertugrul Taciroglu. August 2008.

PEER 2007/11 *Bar Buckling in Reinforced Concrete Bridge Columns.* Wayne A. Brown, Dawn E. Lehman, and John F. Stanton. February 2008.

PEER 2007/10 *Computational Modeling of Progressive Collapse in Reinforced Concrete Frame Structures*. Mohamed M. Talaat and Khalid M. Mosalam. May 2008.

PEER 2007/09 *Integrated Probabilistic Performance-Based Evaluation of Benchmark Reinforced Concrete Bridges*. Kevin R. Mackie, John-Michael Wong, and Božidar Stojadinović. January 2008.

PEER 2007/08 *Assessing Seismic Collapse Safety of Modern Reinforced Concrete Moment-Frame Buildings*. Curt B. Haselton and Gregory G. Deierlein. February 2008.

PEER 2007/07 *Performance Modeling Strategies for Modern Reinforced Concrete Bridge Columns*. Michael P. Berry and Marc O. Eberhard. April 2008.

PEER 2007/06 *Development of Improved Procedures for Seismic Design of Buried and Partially Buried Structures*. Linda Al Atik and Nicholas Sitar. June 2007.

PEER 2007/05 *Uncertainty and Correlation in Seismic Risk Assessment of Transportation Systems*. Renee G. Lee and Anne S. Kiremidjian. July 2007.

PEER 2007/04 *Numerical Models for Analysis and Performance-Based Design of Shallow Foundations Subjected to Seismic Loading.* Sivapalan Gajan, Tara C. Hutchinson, Bruce L. Kutter, Prishati Raychowdhury, José A. Ugalde, and Jonathan P. Stewart. May 2008.

PEER 2007/03 *Beam-Column Element Model Calibrated for Predicting Flexural Response Leading to Global Collapse of RC Frame Buildings*. Curt B. Haselton, Abbie B. Liel, Sarah Taylor Lange, and Gregory G. Deierlein. May 2008.

PEER 2007/02 *Campbell-Bozorgnia NGA Ground Motion Relations for the Geometric Mean Horizontal Component of Peak and Spectral Ground Motion Parameters*. Kenneth W. Campbell and Yousef Bozorgnia. May 2007.

PEER 2007/01 *Boore-Atkinson NGA Ground Motion Relations for the Geometric Mean Horizontal Component of Peak and Spectral Ground Motion Parameters*. David M. Boore and Gail M. Atkinson. May 2007.

PEER 2006/12 Societal Implications of Performance-Based Earthquake Engineering. Peter J. May. May 2007.

PEER 2006/11 *Probabilistic Seismic Demand Analysis Using Advanced Ground Motion Intensity Measures, Attenuation Relationships, and Near-Fault Effects*. Polsak Tothong and C. Allin Cornell. March 2007.

PEER 2006/10 *Application of the PEER PBEE Methodology to the I-880 Viaduct*. Sashi Kunnath. February 2007.

PEER 2006/09 *Quantifying Economic Losses from Travel Forgone Following a Large Metropolitan Earthquake*. James Moore, Sungbin Cho, Yue Yue Fan, and Stuart Werner. November 2006.

PEER 2006/08 *Vector-Valued Ground Motion Intensity Measures for Probabilistic Seismic Demand Analysis*. Jack W. Baker and C. Allin Cornell. October 2006.

PEER 2006/07 *Analytical Modeling of Reinforced Concrete Walls for Predicting Flexural and Coupled–Shear-Flexural Responses*. Kutay Orakcal, Leonardo M. Massone, and John W. Wallace. October 2006.

PEER 2006/06 *Nonlinear Analysis of a Soil-Drilled Pier System under Static and Dynamic Axial Loading*. Gang Wang and Nicholas Sitar. November 2006.

PEER 2006/05 *Advanced Seismic Assessment Guidelines.* Paolo Bazzurro, C. Allin Cornell, Charles Menun, Maziar Motahari, and Nicolas Luco. September 2006.

PEER 2006/04 *Probabilistic Seismic Evaluation of Reinforced Concrete Structural Components and Systems*. Tae Hyung Lee and Khalid M. Mosalam. August 2006.

PEER 2006/03 *Performance of Lifelines Subjected to Lateral Spreading.* Scott A. Ashford and Teerawut Juirnarongrit. July 2006.

PEER 2006/02 *Pacific Earthquake Engineering Research Center Highway Demonstration Project.* Anne Kiremidjian, James Moore, Yue Yue Fan, Nesrin Basoz, Ozgur Yazali, and Meredith Williams. April 2006.

PEER 2006/01 *Bracing Berkeley. A Guide to Seismic Safety on the UC Berkeley Campus.* Mary C. Comerio, Stephen Tobriner, and Ariane Fehrenkamp. January 2006.

PEER 2005/16 *Seismic Response and Reliability of Electrical Substation Equipment and Systems.* Junho Song, Armen Der Kiureghian, and Jerome L. Sackman. April 2006.

PEER 2005/15 *CPT-Based Probabilistic Assessment of Seismic Soil Liquefaction Initiation.* R. E. S. Moss, R. B. Seed, R. E. Kayen, J. P. Stewart, and A. Der Kiureghian. April 2006.

PEER 2005/14 *Workshop on Modeling of Nonlinear Cyclic Load-Deformation Behavior of Shallow Foundations.* Bruce L. Kutter, Geoffrey Martin, Tara Hutchinson, Chad Harden, Sivapalan Gajan, and Justin Phalen. March 2006.

PEER 2005/13 *Stochastic Characterization and Decision Bases under Time-Dependent Aftershock Risk in Performance-Based Earthquake Engineering*. Gee Liek Yeo and C. Allin Cornell. July 2005.

PEER 2005/12 *PEER Testbed Study on a Laboratory Building: Exercising Seismic Performance Assessment.* Mary C. Comerio, Editor. November 2005.

PEER 2005/11 *Van Nuys Hotel Building Testbed Report: Exercising Seismic Performance Assessment.* Helmut Krawinkler, Editor. October 2005.

PEER 2005/10 *First NEES/E-Defense Workshop on Collapse Simulation of Reinforced Concrete Building Structures.* September 2005.

PEER 2005/09 *Test Applications of Advanced Seismic Assessment Guidelines.* Joe Maffei, Karl Telleen, Danya Mohr, William Holmes, and Yuki Nakayama. August 2006.

PEER 2005/08 *Damage Accumulation in Lightly Confined Reinforced Concrete Bridge Columns.* R. Tyler Ranf, Jared M. Nelson, Zach Price, Marc O. Eberhard, and John F. Stanton. April 2006.

PEER 2005/07 *Experimental and Analytical Studies on the Seismic Response of Freestanding and Anchored Laboratory Equipment.* Dimitrios Konstantinidis and Nicos Makris. January 2005.

PEER 2005/06 *Global Collapse of Frame Structures under Seismic Excitations*. Luis F. Ibarra and Helmut Krawinkler. September 2005.

PEER 2005//05 *Performance Characterization of Bench- and Shelf-Mounted Equipment.* Samit Ray Chaudhuri and Tara C. Hutchinson. May 2006.

PEER 2005/04 *Numerical Modeling of the Nonlinear Cyclic Response of Shallow Foundations.* Chad Harden, Tara Hutchinson, Geoffrey R. Martin, and Bruce L. Kutter. August 2005.

PEER 2005/03 *A Taxonomy of Building Components for Performance-Based Earthquake Engineering.* Keith A. Porter. September 2005.

PEER 2005/02 *Fragility Basis for California Highway Overpass Bridge Seismic Decision Making*. Kevin R. Mackie and Božidar Stojadinović. June 2005.

PEER 2005/01 *Empirical Characterization of Site Conditions on Strong Ground Motion.* Jonathan P. Stewart, Yoojoong Choi, and Robert W. Graves. June 2005.

PEER 2004/09 *Electrical Substation Equipment Interaction: Experimental Rigid Conductor Studies.* Christopher Stearns and André Filiatrault. February 2005.

PEER 2004/08 *Seismic Qualification and Fragility Testing of Line Break 550-kV Disconnect Switches.* Shakhzod M. Takhirov, Gregory L. Fenves, and Eric Fujisaki. January 2005.

PEER 2004/07 *Ground Motions for Earthquake Simulator Qualification of Electrical Substation Equipment.* Shakhzod M. Takhirov, Gregory L. Fenves, Eric Fujisaki, and Don Clyde. January 2005.

PEER 2004/06 *Performance-Based Regulation and Regulatory Regimes.* Peter J. May and Chris Koski. September 2004.

PEER 2004/05 *Performance-Based Seismic Design Concepts and Implementation: Proceedings of an International Workshop.* Peter Fajfar and Helmut Krawinkler, Editors. September 2004.

PEER 2004/04 *Seismic Performance of an Instrumented Tilt-up Wall Building.* James C. Anderson and Vitelmo V. Bertero. July 2004.

PEER 2004/03 *Evaluation and Application of Concrete Tilt-up Assessment Methodologies.* Timothy Graf and James O. Malley. October 2004.

PEER 2004/02 *Analytical Investigations of New Methods for Reducing Residual Displacements of Reinforced Concrete Bridge Columns.* Junichi Sakai and Stephen A. Mahin. August 2004.

PEER 2004/01 *Seismic Performance of Masonry Buildings and Design Implications.* Kerri Anne Taeko Tokoro, James C. Anderson, and Vitelmo V. Bertero. February 2004.

PEER 2003/18 *Performance Models for Flexural Damage in Reinforced Concrete Columns.* Michael Berry and Marc Eberhard. August 2003.

PEER 2003/17 *Predicting Earthquake Damage in Older Reinforced Concrete Beam-Column Joints.* Catherine Pagni and Laura Lowes. October 2004.

PEER 2003/16 *Seismic Demands for Performance-Based Design of Bridges.* Kevin Mackie and Božidar Stojadinović. August 2003.

PEER 2003/15 *Seismic Demands for Nondeteriorating Frame Structures and Their Dependence on Ground Motions.* Ricardo Antonio Medina and Helmut Krawinkler. May 2004.

PEER 2003/14 *Finite Element Reliability and Sensitivity Methods for Performance-Based Earthquake Engineering*. Terje Haukaas and Armen Der Kiureghian. April 2004.

PEER 2003/13 *Effects of Connection Hysteretic Degradation on the Seismic Behavior of Steel Moment-Resisting Frames.* Janise E. Rodgers and Stephen A. Mahin. March 2004.

PEER 2003/12 *Implementation Manual for the Seismic Protection of Laboratory Contents: Format and Case Studies*. William T. Holmes and Mary C. Comerio. October 2003.

PEER 2003/11 *Fifth U.S.-Japan Workshop on Performance-Based Earthquake Engineering Methodology for Reinforced Concrete Building Structures*. February 2004.

PEER 2003/10 *A Beam-Column Joint Model for Simulating the Earthquake Response of Reinforced Concrete Frames.* Laura N. Lowes, Nilanjan Mitra, and Arash Altoontash. February 2004.

PEER 2003/09 *Sequencing Repairs after an Earthquake: An Economic Approach.* Marco Casari and Simon J. Wilkie. April 2004.

PEER 2003/08 *A Technical Framework for Probability-Based Demand and Capacity Factor Design (DCFD) Seismic Formats*. Fatemeh Jalayer and C. Allin Cornell. November 2003.

PEER 2003/07 *Uncertainty Specification and Propagation for Loss Estimation Using FOSM Methods.* Jack W. Baker and C. Allin Cornell. September 2003.

PEER 2003/06 *Performance of Circular Reinforced Concrete Bridge Columns under Bidirectional Earthquake Loading*. Mahmoud M. Hachem, Stephen A. Mahin, and Jack P. Moehle. February 2003.

PEER 2003/05 *Response Assessment for Building-Specific Loss Estimation.* Eduardo Miranda and Shahram Taghavi. September 2003.

PEER 2003/04 *Experimental Assessment of Columns with Short Lap Splices Subjected to Cyclic Loads*. Murat Melek, John W. Wallace, and Joel Conte. April 2003.

PEER 2003/03 *Probabilistic Response Assessment for Building-Specific Loss Estimation*. Eduardo Miranda and Hesameddin Aslani. September 2003.

PEER 2003/02 *Software Framework for Collaborative Development of Nonlinear Dynamic Analysis Program*. Jun Peng and Kincho H. Law. September 2003.

PEER 2003/01 *Shake Table Tests and Analytical Studies on the Gravity Load Collapse of Reinforced Concrete Frames.* Kenneth John Elwood and Jack P. Moehle. November 2003.

PEER 2002/24 *Performance of Beam to Column Bridge Joints Subjected to a Large Velocity Pulse.* Natalie Gibson, André Filiatrault, and Scott A. Ashford. April 2002.

PEER 2002/23 *Effects of Large Velocity Pulses on Reinforced Concrete Bridge Columns.* Greg L. Orozco and Scott A. Ashford. April 2002.

PEER 2002/22 *Characterization of Large Velocity Pulses for Laboratory Testing.* Kenneth E. Cox and Scott A. Ashford. April 2002.

PEER 2002/21 *Fourth U.S.-Japan Workshop on Performance-Based Earthquake Engineering Methodology for Reinforced Concrete Building Structures*. December 2002.

PEER 2002/20 *Barriers to Adoption and Implementation of PBEE Innovations.* Peter J. May. August 2002.

PEER 2002/19 *Economic-Engineered Integrated Models for Earthquakes: Socioeconomic Impacts.* Peter Gordon, James E. Moore II, and Harry W. Richardson. July 2002.

PEER 2002/18 *Assessment of Reinforced Concrete Building Exterior Joints with Substandard Details.* Chris P. Pantelides, Jon Hansen, Justin Nadauld, and Lawrence D. Reaveley. May 2002.

PEER 2002/17 *Structural Characterization and Seismic Response Analysis of a Highway Overcrossing Equipped with Elastomeric Bearings and Fluid Dampers: A Case Study*. Nicos Makris and Jian Zhang. November 2002.

PEER 2002/16 *Estimation of Uncertainty in Geotechnical Properties for Performance-Based Earthquake Engineering*. Allen L. Jones, Steven L. Kramer, and Pedro Arduino. December 2002.

PEER 2002/15 *Seismic Behavior of Bridge Columns Subjected to Various Loading Patterns*. Asadollah Esmaeily-Gh. and Yan Xiao. December 2002.

PEER 2002/14 *Inelastic Seismic Response of Extended Pile Shaft Supported Bridge Structures.* T.C. Hutchinson, R.W. Boulanger, Y.H. Chai, and I.M. Idriss. December 2002.

PEER 2002/13 *Probabilistic Models and Fragility Estimates for Bridge Components and Systems.* Paolo Gardoni, Armen Der Kiureghian, and Khalid M. Mosalam. June 2002.

PEER 2002/12 *Effects of Fault Dip and Slip Rake on Near-Source Ground Motions: Why Chi-Chi Was a Relatively Mild M7.6 Earthquake*. Brad T. Aagaard, John F. Hall, and Thomas H. Heaton. December 2002.

PEER 2002/11 *Analytical and Experimental Study of Fiber-Reinforced Strip Isolators*. James M. Kelly and Shakhzod M. Takhirov. September 2002.

PEER 2002/10 *Centrifuge Modeling of Settlement and Lateral Spreading with Comparisons to Numerical Analyses***.** Sivapalan Gajan and Bruce L. Kutter. January 2003.

PEER 2002/09 *Documentation and Analysis of Field Case Histories of Seismic Compression during the 1994 Northridge, California, Earthquake*. Jonathan P. Stewart, Patrick M. Smith, Daniel H. Whang, and Jonathan D. Bray. October 2002.

PEER 2002/08 *Component Testing, Stability Analysis and Characterization of Buckling-Restrained Unbonded Braces™*. Cameron Black, Nicos Makris, and Ian Aiken. September 2002.

PEER 2002/07 *Seismic Performance of Pile-Wharf Connections.* Charles W. Roeder, Robert Graff, Jennifer Soderstrom, and Jun Han Yoo. December 2001.

PEER 2002/06 *The Use of Benefit-Cost Analysis for Evaluation of Performance-Based Earthquake Engineering Decisions*. Richard O. Zerbe and Anthony Falit-Baiamonte. September 2001.

PEER 2002/05 *Guidelines, Specifications, and Seismic Performance Characterization of Nonstructural Building Components and Equipment*. André Filiatrault, Constantin Christopoulos, and Christopher Stearns. September 2001.

PEER 2002/04 *Consortium of Organizations for Strong-Motion Observation Systems and the Pacific Earthquake Engineering Research Center Lifelines Program: Invited Workshop on Archiving and Web Dissemination of Geotechnical Data, 4–5 October 2001*. September 2002.

PEER 2002/03 *Investigation of Sensitivity of Building Loss Estimates to Major Uncertain Variables for the Van Nuys Testbed*. Keith A. Porter, James L. Beck, and Rustem V. Shaikhutdinov. August 2002.

PEER 2002/02 *The Third U.S.-Japan Workshop on Performance-Based Earthquake Engineering Methodology for Reinforced Concrete Building Structures*. July 2002.

PEER 2002/01 *Nonstructural Loss Estimation: The UC Berkeley Case Study.* Mary C. Comerio and John C. Stallmeyer. December 2001.

PEER 2001/16 *Statistics of SDF-System Estimate of Roof Displacement for Pushover Analysis of Buildings.* Anil K. Chopra, Rakesh K. Goel, and Chatpan Chintanapakdee. December 2001.

PEER 2001/15 *Damage to Bridges during the 2001 Nisqually Earthquake.* R. Tyler Ranf, Marc O. Eberhard, and Michael P. Berry. November 2001.

PEER 2001/14 *Rocking Response of Equipment Anchored to a Base Foundation.* Nicos Makris and Cameron J. Black. September 2001.

PEER 2001/13 *Modeling Soil Liquefaction Hazards for Performance-Based Earthquake Engineering*. Steven L. Kramer and Ahmed-W. Elgamal. February 2001.

PEER 2001/12 *Development of Geotechnical Capabilities in OpenSees*. Boris Jeremić. September 2001.

PEER 2001/11 *Analytical and Experimental Study of Fiber-Reinforced Elastomeric Isolators*. James M. Kelly and Shakhzod M. Takhirov. September 2001.

PEER 2001/10 *Amplification Factors for Spectral Acceleration in Active Regions.* Jonathan P. Stewart, Andrew H. Liu, Yoojoong Choi, and Mehmet B. Baturay. December 2001.

PEER 2001/09 *Ground Motion Evaluation Procedures for Performance-Based Design.* Jonathan P. Stewart, Shyh-Jeng Chiou, Jonathan D. Bray, Robert W. Graves, Paul G. Somerville, and Norman A. Abrahamson. September 2001.

PEER 2001/08 *Experimental and Computational Evaluation of Reinforced Concrete Bridge Beam-Column Connections for Seismic Performance*. Clay J. Naito, Jack P. Moehle, and Khalid M. Mosalam. November 2001.

PEER 2001/07 *The Rocking Spectrum and the Shortcomings of Design Guidelines.* Nicos Makris and Dimitrios Konstantinidis. August 2001.

PEER 2001/06 *Development of an Electrical Substation Equipment Performance Database for Evaluation of Equipment Fragilities*. Thalia Agnanos. April 1999.

PEER 2001/05 *Stiffness Analysis of Fiber-Reinforced Elastomeric Isolators.* Hsiang-Chuan Tsai and James M. Kelly. May 2001.

PEER 2001/04 *Organizational and Societal Considerations for Performance-Based Earthquake Engineering*. Peter J. May. April 2001.

PEER 2001/03 *A Modal Pushover Analysis Procedure to Estimate Seismic Demands for Buildings: Theory and Preliminary Evaluation*. Anil K. Chopra and Rakesh K. Goel. January 2001.

PEER 2001/02 *Seismic Response Analysis of Highway Overcrossings Including Soil-Structure Interaction*. Jian Zhang and Nicos Makris. March 2001.

PEER 2001/01 *Experimental Study of Large Seismic Steel Beam-to-Column Connections.* Egor P. Popov and Shakhzod M. Takhirov. November 2000.

PEER 2000/10 *The Second U.S.-Japan Workshop on Performance-Based Earthquake Engineering Methodology for Reinforced Concrete Building Structures*. March 2000.

PEER 2000/09 *Structural Engineering Reconnaissance of the August 17, 1999 Earthquake: Kocaeli (Izmit), Turkey*. Halil Sezen, Kenneth J. Elwood, Andrew S. Whittaker, Khalid Mosalam, John J. Wallace, and John F. Stanton. December 2000.

PEER 2000/08 *Behavior of Reinforced Concrete Bridge Columns Having Varying Aspect Ratios and Varying Lengths of Confinement*. Anthony J. Calderone, Dawn E. Lehman, and Jack P. Moehle. January 2001.

PEER 2000/07 *Cover-Plate and Flange-Plate Reinforced Steel Moment-Resisting Connections.* Taejin Kim, Andrew S. Whittaker, Amir S. Gilani, Vitelmo V. Bertero, and Shakhzod M. Takhirov. September 2000.

PEER 2000/06 *Seismic Evaluation and Analysis of 230-kV Disconnect Switches.* Amir S. J. Gilani, Andrew S. Whittaker, Gregory L. Fenves, Chun-Hao Chen, Henry Ho, and Eric Fujisaki. July 2000.

PEER 2000/05 *Performance-Based Evaluation of Exterior Reinforced Concrete Building Joints for Seismic Excitation*. Chandra Clyde, Chris P. Pantelides, and Lawrence D. Reaveley. July 2000.

PEER 2000/04 *An Evaluation of Seismic Energy Demand: An Attenuation Approach*. Chung-Che Chou and Chia-Ming Uang. July 1999.

PEER 2000/03 *Framing Earthquake Retrofitting Decisions: The Case of Hillside Homes in Los Angeles.* Detlof von Winterfeldt, Nels Roselund, and Alicia Kitsuse. March 2000.

PEER 2000/02 *U.S.-Japan Workshop on the Effects of Near-Field Earthquake Shaking*. Andrew Whittaker, Editor. July 2000.

PEER 2000/01 *Further Studies on Seismic Interaction in Interconnected Electrical Substation Equipment.* Armen Der Kiureghian, Kee-Jeung Hong, and Jerome L. Sackman. November 1999.

PEER 1999/14 *Seismic Evaluation and Retrofit of 230-kV Porcelain Transformer Bushings*. Amir S. Gilani, Andrew S. Whittaker, Gregory L. Fenves, and Eric Fujisaki. December 1999.

PEER 1999/13 *Building Vulnerability Studies: Modeling and Evaluation of Tilt-up and Steel Reinforced Concrete Buildings*. John W. Wallace, Jonathan P. Stewart, and Andrew S. Whittaker, Editors. December 1999.

PEER 1999/12 *Rehabilitation of Nonductile RC Frame Building Using Encasement Plates and Energy-Dissipating Devices*. Mehrdad Sasani, Vitelmo V. Bertero, James C. Anderson. December 1999.

PEER 1999/11 *Performance Evaluation Database for Concrete Bridge Components and Systems under Simulated Seismic Loads*. Yael D. Hose and Frieder Seible. November 1999.

PEER 1999/10 *U.S.-Japan Workshop on Performance-Based Earthquake Engineering Methodology for Reinforced Concrete Building Structures*. December 1999.

PEER 1999/09 *Performance Improvement of Long Period Building Structures Subjected to Severe Pulse-Type Ground Motions*. James C. Anderson, Vitelmo V. Bertero, and Raul Bertero. October 1999.

PEER 1999/08 *Envelopes for Seismic Response Vectors.* Charles Menun and Armen Der Kiureghian. July 1999.

PEER 1999/07 *Documentation of Strengths and Weaknesses of Current Computer Analysis Methods for Seismic Performance of Reinforced Concrete Members*. William F. Cofer. November 1999.

PEER 1999/06 *Rocking Response and Overturning of Anchored Equipment under Seismic Excitations*. Nicos Makris and Jian Zhang. November 1999.

PEER 1999/05 *Seismic Evaluation of 550 kV Porcelain Transformer Bushings.* Amir S. Gilani, Andrew S. Whittaker, Gregory L. Fenves, and Eric Fujisaki. October 1999.

PEER 1999/04 *Adoption and Enforcement of Earthquake Risk-Reduction Measures.* Peter J. May, Raymond J. Burby, T. Jens Feeley, and Robert Wood. August 1999.

PEER 1999/03 *Task 3 Characterization of Site Response General Site Categories*. Adrian Rodriguez-Marek, Jonathan D. Bray and Norman Abrahamson. February 1999.

PEER 1999/02 *Capacity-Demand-Diagram Methods for Estimating Seismic Deformation of Inelastic Structures: SDF Systems*. Anil K. Chopra and Rakesh Goel. April 1999.

PEER 1999/01 *Interaction in Interconnected Electrical Substation Equipment Subjected to Earthquake Ground Motions*. Armen Der Kiureghian, Jerome L. Sackman, and Kee-Jeung Hong. February 1999.

PEER 1998/08 *Behavior and Failure Analysis of a Multiple-Frame Highway Bridge in the 1994 Northridge Earthquake*. Gregory L. Fenves and Michael Ellery. December 1998.

PEER 1998/07 *Empirical Evaluation of Inertial Soil-Structure Interaction Effects.* Jonathan P. Stewart, Raymond B. Seed, and Gregory L. Fenves. November 1998.

PEER 1998/06 *Effect of Damping Mechanisms on the Response of Seismic Isolated Structures*. Nicos Makris and Shih-Po Chang. November 1998.

PEER 1998/05 *Rocking Response and Overturning of Equipment under Horizontal Pulse-Type Motions*. Nicos Makris and Yiannis Roussos. October 1998.

PEER 1998/04 *Pacific Earthquake Engineering Research Invitational Workshop Proceedings, May 14–15, 1998: Defining the Links between Planning, Policy Analysis, Economics and Earthquake Engineering*. Mary Comerio and Peter Gordon. September 1998.

PEER 1998/03 *Repair/Upgrade Procedures for Welded Beam to Column Connections*. James C. Anderson and Xiaojing Duan. May 1998.

PEER 1998/02 *Seismic Evaluation of 196 kV Porcelain Transformer Bushings.* Amir S. Gilani, Juan W. Chavez, Gregory L. Fenves, and Andrew S. Whittaker. May 1998.

PEER 1998/01 *Seismic Performance of Well-Confined Concrete Bridge Columns.* Dawn E. Lehman and Jack P. Moehle. December 2000.

ONLINE PEER REPORTS

The following PEER reports are available by Internet only at http://peer.berkeley.edu/publications/peer_reports_complete.html.

PEER 2012/103 *Performance-Based Seismic Demand Assessment of Concentrically Braced Steel Frame Buildings.* Chui-Hsin Chen and Stephen A. Mahin. December 2012.

PEER 2012/102 *Procedure to Restart an Interrupted Hybrid Simulation: Addendum to PEER Report 2010/103.* Vesna Terzic and Bozidar Stojadinovic. October 2012.

PEER 2012/101 *Mechanics of Fiber Reinforced Bearings.* James M. Kelly and Andrea Calabrese. February 2012.

PEER 2011/107 *Nonlinear Site Response and Seismic Compression at Vertical Array Strongly Shaken by 2007 Niigata-ken Chuetsu-oki Earthquake.* Eric Yee, Jonathan P. Stewart, and Kohji Tokimatsu. December 2011.

PEER 2011/106 *Self Compacting Hybrid Fiber Reinforced Concrete Composites for Bridge Columns.* Pardeep Kumar, Gabriel Jen, William Trono, Marios Panagiotou, and Claudia Ostertag. September 2011.

PEER 2011/105 *Stochastic Dynamic Analysis of Bridges Subjected to Spacially Varying Ground Motions.* Katerina Konakli and Armen Der Kiureghian. August 2011.

PEER 2011/104 *Design and Instrumentation of the 2010 E-Defense Four-Story Reinforced Concrete and Post-Tensioned Concrete Buildings.* Takuya Nagae, Kenichi Tahara, Taizo Matsumori, Hitoshi Shiohara, Toshimi Kabeyasawa, Susumu Kono, Minehiro Nishiyama (Japanese Research Team) and John Wallace, Wassim Ghannoum, Jack Moehle, Richard Sause, Wesley Keller, Zeynep Tuna (U.S. Research Team). June 2011.

PEER 2011/103 *In-Situ Monitoring of the Force Output of Fluid Dampers: Experimental Investigation.* Dimitrios Konstantinidis, James M. Kelly, and Nicos Makris. April 2011.

PEER 2011/102 *Ground-Motion Prediction Equations 1964–2010.* John Douglas. April 2011.

PEER 2011/101 *Report of the Eighth Planning Meeting of NEES/E-Defense Collaborative Research on Earthquake Engineering.* Convened by the Hyogo Earthquake Engineering Research Center (NIED), NEES Consortium, Inc. February 2011.

PEER 2010/111 *Modeling and Acceptance Criteria for Seismic Design and Analysis of Tall Buildings.* Task 7 Report for the Tall Buildings Initiative - Published jointly by the Applied Technology Council. October 2010.

PEER 2010/110 *Seismic Performance Assessment and Probabilistic Repair Cost Analysis of Precast Concrete Cladding Systems for Multistory Buildlings.* Jeffrey P. Hunt and Božidar Stojadinovic. November 2010.

PEER 2010/109 *Report of the Seventh Joint Planning Meeting of NEES/E-Defense Collaboration on Earthquake Engineering. Held at the E-Defense, Miki, and Shin-Kobe, Japan, September 18–19, 2009.* August 2010.

PEER 2010/108 *Probabilistic Tsunami Hazard in California.* Hong Kie Thio, Paul Somerville, and Jascha Polet, preparers. October 2010.

PEER 2010/107 *Performance and Reliability of Exposed Column Base Plate Connections for Steel Moment-Resisting Frames.* Ady Aviram, Božidar Stojadinovic, and Armen Der Kiureghian. August 2010.

PEER 2010/106 *Verification of Probabilistic Seismic Hazard Analysis Computer Programs.* Patricia Thomas, Ivan Wong, and Norman Abrahamson. May 2010.

PEER 2010/105 *Structural Engineering Reconnaissance of the April 6, 2009, Abruzzo, Italy, Earthquake, and Lessons Learned.* M. Selim Günay and Khalid M. Mosalam. April 2010.

PEER 2010/104 *Simulating the Inelastic Seismic Behavior of Steel Braced Frames, Including the Effects of Low-Cycle Fatigue.* Yuli Huang and Stephen A. Mahin. April 2010.

PEER 2010/103 *Post-Earthquake Traffic Capacity of Modern Bridges in California.* Vesna Terzic and Božidar Stojadinović. March 2010.

PEER 2010/102 *Analysis of Cumulative Absolute Velocity (CAV) and JMA Instrumental Seismic Intensity (I_{JMA}) Using the PEER–NGA Strong Motion Database.* Kenneth W. Campbell and Yousef Bozorgnia. February 2010.

PEER 2010/101 *Rocking Response of Bridges on Shallow Foundations.* Jose A. Ugalde, Bruce L. Kutter, and Boris Jeremic. April 2010.

PEER 2009/109 *Simulation and Performance-Based Earthquake Engineering Assessment of Self-Centering Post-Tensioned Concrete Bridge Systems.* Won K. Lee and Sarah L. Billington. December 2009.

PEER 2009/108 *PEER Lifelines Geotechnical Virtual Data Center.* J. Carl Stepp, Daniel J. Ponti, Loren L. Turner, Jennifer N. Swift, Sean Devlin, Yang Zhu, Jean Benoit, and John Bobbitt. September 2009.

PEER 2009/107 *Experimental and Computational Evaluation of Current and Innovative In-Span Hinge Details in Reinforced Concrete Box-Girder Bridges: Part 2: Post-Test Analysis and Design Recommendations.* Matias A. Hube and Khalid M. Mosalam. December 2009.

PEER 2009/106 *Shear Strength Models of Exterior Beam-Column Joints without Transverse Reinforcement.* Sangjoon Park and Khalid M. Mosalam. November 2009.

PEER 2009/105 *Reduced Uncertainty of Ground Motion Prediction Equations through Bayesian Variance Analysis.* Robb Eric S. Moss. November 2009.

PEER 2009/104 *Advanced Implementation of Hybrid Simulation.* Andreas H. Schellenberg, Stephen A. Mahin, Gregory L. Fenves. November 2009.

PEER 2009/103 *Performance Evaluation of Innovative Steel Braced Frames.* T. Y. Yang, Jack P. Moehle, and Božidar Stojadinovic. August 2009.

PEER 2009/102 *Reinvestigation of Liquefaction and Nonliquefaction Case Histories from the 1976 Tangshan Earthquake.* Robb Eric Moss, Robert E. Kayen, Liyuan Tong, Songyu Liu, Guojun Cai, and Jiaer Wu. August 2009.

PEER 2009/101 *Report of the First Joint Planning Meeting for the Second Phase of NEES/E-Defense Collaborative Research on Earthquake Engineering.* Stephen A. Mahin et al. July 2009.

PEER 2008/104 *Experimental and Analytical Study of the Seismic Performance of Retaining Structures.* Linda Al Atik and Nicholas Sitar. January 2009.

PEER 2008/103 *Experimental and Computational Evaluation of Current and Innovative In-Span Hinge Details in Reinforced Concrete Box-Girder Bridges. Part 1: Experimental Findings and Pre-Test Analysis.* Matias A. Hube and Khalid M. Mosalam. January 2009.

PEER 2008/102 *Modeling of Unreinforced Masonry Infill Walls Considering In-Plane and Out-of-Plane Interaction.* Stephen Kadysiewski and Khalid M. Mosalam. January 2009.

PEER 2008/101 *Seismic Performance Objectives for Tall Buildings.* William T. Holmes, Charles Kircher, William Petak, and Nabih Youssef. August 2008.

PEER 2007/101 *Generalized Hybrid Simulation Framework for Structural Systems Subjected to Seismic Loading*. Tarek Elkhoraibi and Khalid M. Mosalam. July 2007.

PEER 2007/100 *Seismic Evaluation of Reinforced Concrete Buildings Including Effects of Masonry Infill Walls*. Alidad Hashemi and Khalid M. Mosalam. July 2007.

The Pacific Earthquake Engineering Research Center (PEER) is a multi-institutional research and education center with headquarters at the University of California, Berkeley. Investigators from over 20 universities, several consulting companies, and researchers at various state and federal government agencies contribute to research programs focused on performance-based earthquake engineering.

These research programs aim to identify and reduce the risks from major earthquakes to life safety and to the economy by including research in a wide variety of disciplines including structural and geotechnical engineering, geology/seismology, lifelines, transportation, architecture, economics, risk management, and public policy.

PEER is supported by federal, state, local, and regional agencies, together with industry partners.

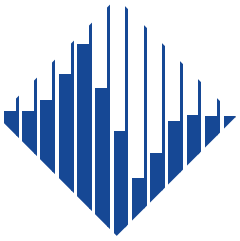

PEER Core Institutions:
University of California, Berkeley (Lead Institution)
California Institute of Technology
Oregon State University
Stanford University
University of California, Davis
University of California, Irvine
University of California, Los Angeles
University of California, San Diego
University of Southern California
University of Washington

PEER reports can be ordered at http://peer.berkeley.edu/publications/peer_reports.html or by contacting

Pacific Earthquake Engineering Research Center
University of California, Berkeley
325 Davis Hall, Mail Code 1792
Berkeley, CA 94720-1792
Tel: 510-642-3437
Fax: 510-642-1655
Email: clairejohnson@berkeley.edu

ISSN 1547-0587X